ISTANBUL TECHNICAL UNIVERSITY ★ GRADUATE SCHOOL

THE ANALYTICAL SOLUTIONS AND DEEP LEARNING ASSESSMENT OF LONG WAVES OVER LINEAR AND NONLINEAR BREADTH AND DEPTH PROFILES: 30 OCTOBER 2020 İZMİR TSUNAMI CASE

Ph.D. THESIS

Ali Rıza ALAN

Department of Coastal Sciences and Engineering

Coastal Sciences and Engineering Programme

MAY 2024

ISTANBUL TECHNICAL UNIVERSITY ★ GRADUATE SCHOOL

THE ANALYTICAL SOLUTIONS AND DEEP LEARNING ASSESSMENT OF LONG WAVES OVER LINEAR AND NONLINEAR BREADTH AND DEPTH PROFILES: 30 OCTOBER 2020 İZMİR TSUNAMI CASE

Ph.D. THESIS

Ali Rıza ALAN
(517202002)

Department of Coastal Sciences and Engineering

Coastal Sciences and Engineering Programme

Thesis Advisor: Assoc. Prof. Dr. Cihan BAYINDIR

MAY 2024

İSTANBUL TEKNİK ÜNİVERSİTESİ ★ LİSANSÜSTÜ EĞİTİM ENSTİTÜSÜ

DOĞRUSAL OLAN VE OLMAYAN GENİŞLİK VE DERİNLİK PROFİLLERİ ÜZERİNDE UZUN DALGALARIN ÇÖZÜMLERİ VE DERİN ÖĞRENME İLE DEĞERLENDİRİLMESİ: 30 EKİM 2020 İZMİR TSUNAMİSİ ÖRNEĞİ

DOKTORA TEZİ

Ali Rıza ALAN
(517202002)

Kıyı Bilimleri ve Mühendisliği Anabilim Dalı

Kıyı Bilimleri ve Mühendisliği Programı

Tez Danışmanı: Doç. Dr. Cihan BAYINDIR

MAYIS 2024

Ali Rıza ALAN, a Ph.D. student of ITU Graduate School student ID 517202002 successfully defended the thesis entitled "THE ANALYTICAL SOLUTIONS AND DEEP LEARNING ASSESSMENT OF LONG WAVES OVER LINEAR AND NONLINEAR BREADTH AND DEPTH PROFILES: 30 OCTOBER 2020 İZMİR TSUNAMI CASE", which he prepared after fulfilling the requirements specified in the associated legislations, before the jury whose signatures are below.

Thesis Advisor :	**Assoc. Prof. Dr. Cihan BAYINDIR** İstanbul Technical University & Boğaziçi University	....
Jury Members :	**Prof. Dr. Mehmet ÖZGER** İstanbul Technical University	....
	Prof. Dr. Abdüsselam ALTUNKAYNAK İstanbul Technical University	....
	Prof. Dr. Berna AYAT AYDOĞAN Yıldız Technical University	....
	Assoc. Prof. Dr. Burak AYDOĞAN Gebze Technical University	....

Date of Submission : **29 March 2024**
Date of Defense : **27 May 2024**

To my grandfather Ali Rıza...

FOREWORD

If I were to dedicate this thesis to only one person, undoubtedly, that person would be my thesis advisor, Assoc. Prof. Dr. Cihan BAYINDIR. I am eternally grateful to Assoc. Prof. Dr. Cihan BAYINDIR, who took my hand and shaped me into a real man while I was drifting in the wind like a withered leaf hopelessly. His profound knowledge has been a guiding light to me throughout my entire academic life. He fearlessly battled alongside me against everyone and everything. If I have become myself, it is because of him. He has been both my thesis advisor and an elder brother to me. Even if I were to serve him for the rest of my life, I could never repay my debt to him. I would be so fortunate if I could become a scientist like him one day. I thank God for granting me a mentor like Assoc. Prof. Dr. Cihan BAYINDIR, and for everything else, I am thankful to Assoc. Prof. Dr. Cihan BAYINDIR. May God bless him. Only the departed see his defeat. This thesis is an oblation to our brotherhood.

I extend my heartfelt thanks to my esteemed professors Prof. Dr. Mehmet ÖZGER and Prof. Dr. Berna AYAT AYDOĞAN for their support and guidance during my presentations as a part of my Doctoral Thesis Steering Committee. I am very grateful to Assoc. Prof. Dr. Cihan BAYINDIR's dear friends Prof. Dr. Fatih ÖZAYDIN and Prof. Dr. Azmi Ali ALTINTAŞ for their assistance. I thank Prof. Dr. Abdüsselam ALTUNKAYNAK, Assoc. Prof. Dr. Burak AYDOĞAN, Assoc. Prof. Dr. Tarkan ERDİK, Assoc. Prof. Dr. Yiğit Can ALTAN, Prof. Dr. Emre OTAY, and Prof. Dr. Ahmet ERGİN for their invaluable comments. A special thanks to Prof. Dr. Robert G. DEAN, Prof. Dr. Robert A. DALRYMPLE, Prof. Dr. Nobuhisa KOBAYASHI, Prof. Dr. Yoshimi GODA, Prof. Dr. Chiang C. MEI, and my academic grandfathers Prof. Dr. James T. KIRBY and Prof. Dr. J. David FROST, whose books and works I benefited from and inspired throughout my doctoral education.

Finally, I express my gratitude to my mother, Firdevs ALAN, who has always been by my side with her prayers, my father, Bekir ALAN, who is my first teacher, my dear sister, Dr. Semina ALAN, and my grandparents, for their boundless support. I thank our great leader, Commander-In-Chief Marshall Ghazi Mustafa Kemal ATATÜRK, who created my philosophy of life with his apothegm "Science is the only true guide in life!" and gifted me a country where I could pursue my doctorate.

I would like to acknowledge and thank that this thesis study is funded by the Turkish Academy of Sciences (TÜBA)-Outstanding Young Scientist Award (GEBİP)-2022, The Science Academy-Young Scientist Award (BAGEP)-2024, and the Research Fund of the İstanbul Technical University with project code: MDK-2021-42849.

May 2024

Ali Rıza ALAN
(Civil Engineer, M.Sc.)

TABLE OF CONTENTS

Page

ABBREVIATIONS

1D	: One Dimensional
2D	: Two Dimensional
AI	: Artifical Intelligence
BC	: Boundary Condition
BVP	: Boundary Value Problem
DART	: Deep-Ocean Assessment and Reporting of Tsunami
DL	: Deep Learning
FFT	: Fast Fourier Transform
GMT	: Greenwich Mean Time
IFFT	: Inverse Fast Fourier Transform
IMSL	: International Mathematics and Statistics Library
KOERI	: Boğaziçi University Kandilli Observatory and Earthquake Research Institute
LSTM	: Long-Short Term Memory
MATLAB	: MATrix LABoratory
NOAA	: National Oceanic and Atmospheric Administration
RMSE	: Root Mean Square Error
RNN	: Recurrent Neural Networks
SWAT	: Soil and Water Assessment Tool
UNESCO	: United Nations Educational, Scientific and Cultural Organization
UTC	: Universal Time Coordinated

SYMBOLS

A	: Incident Wave Amplitude
b(x)	: Breadth Function
$\boldsymbol{\beta}$	: Slope Angle
$\mathbf{C_i}$	: Imaginary Part of C_w
$\mathbf{C_r}$	: Real Part of C_w
$\mathbf{C_w}$	: Complex Parameter Associated with the Degree of Wave Reflection
$\mathbf{d_{eq}}$	: Equivalent Grain Diameter
$\mathbf{d_t}$	: Water Depth at the Structure's Toe
$\boldsymbol{\delta}$	: Reflected Wave Phase Lag
$\mathbf{E_i}$	: Incident Wave Energy
$\mathbf{E_r}$	: Reflected Wave Energy
$\boldsymbol{\eta}(\mathbf{x},\mathbf{t})$	: Water Surface Fluctuation Function
$\mathbf{f_i}$	: Forget Gate
$\mathbf{f_n}$	: Frequency of the nth Component
g	: Gravitational Acceleration
$\mathbf{g_i}$	: Input Gate
H	: Wave Height
$\mathbf{H_0}$	: Incident Deep Water Wave Height
$\mathbf{H_b}$	: Wave Breaker Height
$\mathbf{H_i}$	: Incident Wave Height
$\mathbf{H_r}$	: Reflected Wave Height
$\mathbf{H_s}$	: Significant Wave Height
h	: Water Depth
$\mathbf{h_b}$	: Depth at Which the Wave Breaking Begins
$\mathbf{h_i}$	: The Output
$\mathbf{h_{toe}}$	: Local Water Depth at the Structure's Toe
h(x)	: Depth Function
i	: Unit Imaginary Number ($\sqrt{-1}$)
$\mathbf{J_\nu(z)}$	: Bessel Function of the First Kind Order ν
k	: Wave Number
$\mathbf{L_0}$	: Wave Length in Deep Water
$\mathbf{L_s}$	: Linear Theory Shallow Water Wavelength
$\boldsymbol{\omega}$	: Angular Frequency (for Wave Reflection)
P	: Notional Permeability
$\mathbf{q_i}$	: Output Gate
R	: Wave Reflection Coefficient
r	: Reflection Number
$\mathbf{s_i}$	: State Unit

$\boldsymbol{\sigma}$: Angular Frequency
T : Long-Wave Period
$\mathbf{T_p}$: Peak Period
t : Time
u : Horizontal Velocity
x : Spatial Coordinate
$\mathbf{x_m}$: Cross-Shore Length of the Structure from the Toe to Still Water Level
$\boldsymbol{\xi}$: Surf Similarity Parameter (Iribarren Number)
$\mathbf{Y_{\boldsymbol{\nu}}(z)}$: Bessel Function of the Second Kind Order ν

LIST OF TABLES

LIST OF FIGURES

Page

THE ANALYTICAL SOLUTIONS AND DEEP LEARNING ASSESSMENT OF LONG WAVES OVER LINEAR AND NONLINEAR BREADTH AND DEPTH PROFILES: 30 OCTOBER 2020 İZMİR TSUNAMI CASE

SUMMARY

Long waves in harbor engineering present some difficulties, such as preventing harbor resonance. Understanding and forecasting their dynamics is essential due to similar issues. The nonlinear geometries with power-law forms are not well explored, despite the fact that their dynamics have been thoroughly examined in the literature for a wide range of geometries. A recent paper by the advisor of this thesis describes the analytical solutions of the long-wave equation over nonlinear depth and breadth profiles with power-law forms as $h(x) = c_1x^a$ and $b(x) = c_2x^c$, where the parameters c_1, c_2, a, and c are some constants. Motivated by this, we expand on our previous work in this thesis and derive the precise analytical solutions of the long-wave equation across both linear and nonlinear in the power-law form depth and breadth geometries in which a solid vertical or inclined wall exists.

This thesis consists of 5 chapters. In Chapter 1 within the frame of Introduction, we discuss the known solutions of long waves over different variations in breadth and depth. The solutions for the Bessel Function are expressed. Free Oscillation Period examples are presented. We refer to Laguerre Polynomials and Gauss Hypergeometric Series. Lastly, we introduce the Power-Law form solution to the Long Wave equation.

In Chapter 2 within the frame of Publication Number 1, in the presence of the solid vertical wall, we demonstrate that for these specific power-law forms of depth and breadth profiles, the long-wave equation admits solutions in terms of Bessel-Z functions and the Cauchy-Euler series. Analytical solutions' singular points are removed from the domain when the origin of the harbor/bay geometry contains a solid vertical wall. Consequently, the solutions produced exhibit both the first and second kind of the Bessel functions. Our findings pertain to the overall category of geometries that we examine that have solid vertical or inclined walls. Furthermore, six other instances for the above geometries with the presence of a solid vertical wall are analyzed. Water surface fluctuation functions are obtained in terms of Bessel-Z functions for each of the six different cases. These obtained functions are displayed graphically along with the relevant geometry drawing. Afterward, these graphics are interpreted regarding areas such as in-harbor resonance and wave energy converter.

In Chapter 3 within the frame of Publication Number 2, the work on the exact analytical solutions of the long-wave equation with vertical wall case, which we had previously completed in Chapter 2 within the frame of Publication Number 1, is repeated, but for the case with inclined walls. First, we provide a general overview of partial reflection and its constituent parts—the slope angle, phase lag, reflection coefficient, and Iribarren number—which we have to consider because of the inclined wall, in

addition to the preceding chapter on this subject. On the other hand, we discover that the solutions to the long wave equations are given by Bessel-Z functions; nevertheless, when accounting for a parabolic depth variation, these solutions assume the form of the Cauchy-Euler series. Once more, we present our findings and provide the analytical solution for long waves in different configurations. As in the previous section, water surface fluctuation functions are obtained in terms of Bessel-Z functions for each of the six different cases. These obtained functions are displayed graphically along with the relevant geometry drawing. Afterward, these graphs are compared with the graphs of the vertical wall situation in the previous chapter, and interpretations are made regarding areas such as in-harbor resonance and wave energy converter.

After completing the analytical solutions of long waves containing vertical and inclined wall situations, in Chapter 4 within the frame of Publication Number 3, we move on to the study of the 30 October 2020 İzmir Tsunami, which is the special case of our thesis. In the nearshore environment, tsunamis can be exceedingly deadly even if they happen less frequently than certain other natural disasters. Around 23 km south of Turkey's İzmir province, off the Greek island of Samos, an earthquake with a magnitude of 6.9 Mw struck on October 30, 2020, at 12:51 p.m. UTC (2:51 p.m. GMT+03:00). The tsunami event generated by this earthquake is known as the 30 October 2020 İzmir-Samos (Aegean) tsunami, and in this thesis, we examine the hydrodynamics of this tsunami using some of artificial intelligence (AI) approaches applied to observational data. Comprehensive information is given about the history, structure, content, and working principle of the LSTM deep learning algorithm. We explain that data flow is made possible by the forget, input, and output gates as well as a memory cell outside the input that determines whether the information will be transferred, retained, or forgotten.

More precisely, we make use of the tsunami time series that we obtained at various sites in Bodrum, Syros, Kos, and Kos Marina from the UNESCO data portal. Next, the application and limitations of the Long Short Term Memory (LSTM) DL approach for the Fourier spectrum and time series prediction of tsunamis are examined. More specifically, we investigate the predictability of the dynamics of offshore water surface elevation, their spectral frequency and amplitude properties, potential success factors for predictions, and the improvement of the precise early prediction time scales. To do this, the data utilized in this study is de-tided using a spectral technique to eliminate the astronomical tidal influence. An FFT-IFFT technique is employed for this. It is shown that LSTM with updates is more successful in predicting the lower frequency components for the tsunami time series. Potential study options are also explored, along with the applications and use of our results.

In Chapter 5, within the frame of Conclusion, we report our findings. Our findings can be used in the study of long wave resonance and runup in bays and harbors, as well as wave energy focusers and resonators. It is also possible to investigate the effects on long-wave hydrodynamics of wall building, dredging, and geometry changes generated by landslides within the framework of the conclusions reached in this thesis. Moreover, performance gains in tsunami early warning systems and numerous investigations on tsunami characteristics, such as run-up time series and horizontal and excursion velocities, can be pioneered by utilizing the findings of this thesis study.

We propose to use our work to obtain the solutions of the long wave equation for additional geometries with different shapes, such as a vertical or inclined wall, in terms of Laguerre, Chebyshev, Hermite, or Legendre polynomials. Likewise, we state that all these parameters can be studied in 2D instead of 1D as well. Finally, we state in detail the studies we plan to do in the future using the findings of our thesis studies and how we will do them in the Conclusion section.

DOĞRUSAL OLAN VE OLMAYAN GENİŞLİK VE DERİNLİK PROFİLLERİ ÜZERİNDE UZUN DALGALARIN ÇÖZÜMLERİ VE DERİN ÖĞRENME İLE DEĞERLENDİRİLMESİ: 30 EKİM 2020 İZMİR TSUNAMİSİ ÖRNEĞİ

ÖZET

Liman mühendisliğinde uzun dalgalar, liman rezonansının önlenmesi gibi bazı zorlukları beraberinde getirmiştir. Benzer sorunlar nedeniyle uzun dalgaların dinamiklerini anlamak ve tahmin etmek önemlidir. Güç yasası formlarına sahip doğrusal olmayan geometriler, dinamikleri literatürde geniş bir geometri yelpazesi için kapsamlı bir şekilde incelenmiş olmasına rağmen, yeterince araştırılmamıştır. Bu tezin danışmanı tarafından yakın zamanda hazırlanan bir makale, $h(x) = c_1x^a$ ve $b(x) = c_2x^c$ şeklinde güç yasası formlarıyla uzun dalga denkleminin doğrusal olmayan derinlik ve genişlik profilleri üzerindeki analitik çözümlerini açıklamıştır. Burada c_1, c_2, a ve c parametreleri bazı sabitlerdir. Bundan motive olarak, bu tezde önceki çalışmalarımız genişletilmiş ve uzun dalga denkleminin hem doğrusal hem de doğrusal olmayan kesin analitik çözümleri, katı dikey veya eğimli bir duvarın bulunduğu güç yasası formundaki derinlik ve genişlik geometrilerinde türetilmiştir.

Bu tez 5 bölümden oluşmaktadır. Bölüm 1'de Giriş çerçevesinde, farklı genişlik ve derinlik değişimleri üzerinden uzun dalgaların bilinen çözümleri tartışılmıştır. Bessel Fonksiyonu çözümleri anlatılmıştır. Serbest Salınım Periyotları örnekleri sunulmuştur. Laguerre Polinomları ve Gauss Hipergeometrik Serilerinden bahsedilmiştir. Son olarak Uzun Dalga denklemi için Güç Yasası formunun çözümü tanıtılmıştır.

Bölüm 2'de 1 Numaralı Yayın çerçevesinde, katı dikey duvarın varlığında, derinlik ve genişlik profillerinin bu özel güç yasası formları için uzun dalga denkleminin Bessel-Z fonksiyonları ve Cauchy-Euler serisi cinsinden çözümleri kabul ettiği gösterilmiştir. Analitik çözümlerin tekil noktaları, liman/körfez geometrisinin orijini katı dikey bir duvar içerdiğinde etki alanından çıkarılmıştır. Sonuç olarak üretilen çözümler Bessel fonksiyonlarının hem birinci hem de ikinci türünü sergilemektedir. Bulgularımız, incelediğimiz katı dikey duvarlara sahip geometrilerin genel kategorisiyle ilgilidir. Ayrıca, katı dikey bir duvarın bulunduğu yukarıdaki geometriler için altı örnek daha analiz edilmiştir. Su yüzeyi dalgalanma fonksiyonları, altı farklı durumun her biri için Bessel-Z fonksiyonları cinsinden elde edilmiştir. Elde edilen bu fonksiyonlar ilgili geometri çizimi ile birlikte grafiksel olarak gösterilmiştir. Daha sonra bu grafikler liman içi rezonans ve dalga enerjisi dönüştürücü gibi alanlara göre yorumlanmıştır.

Bölüm 3'te 2 Numaralı Yayın çerçevesinde, daha önce Bölüm 2'de 1 Numaralı Yayın çerçevesinde, tamamladığımız dikey duvarlı durum için uzun dalga denkleminin kesin analitik çözümleri üzerine olan çalışma eğimli duvar durumu için tekrarlanmıştır. İlk olarak, bu konuyla ilgili önceki bölüme ek, eğimli duvar nedeniyle dikkate almamız gereken kısmi yansıma ve onu oluşturan kısımlar (eğim açısı, faz gecikmesi, yansıma

katsayısı ve Iribarren sayısı) hakkında genel bir bakış sunulmuştur. Öte yandan yine uzun dalga denklemlerinin çözümlerinin Bessel-Z fonksiyonları ile verildiği ve parabolik derinlik değişimini hesaba katarken bu çözümlerin Cauchy-Euler serisinin biçimini aldığı gösterilmiştir. Bir kez daha bulgularımız ve farklı konfigürasyonlardaki uzun dalgalar için analitik çözümlerimiz sunulmuştur. Önceki bölümde olduğu gibi, altı farklı durumun her biri için su yüzeyi dalgalanma fonksiyonları Bessel-Z fonksiyonları cinsinden elde edilmiştir. Elde edilen bu fonksiyonlar ilgili geometri çizimi ile birlikte grafiksel olarak gösterilmiştir. Daha sonra bu grafikler bir önceki bölümde anlatılan dikey duvar durumu grafikleri ile karşılaştırılarak liman içi rezonans ve dalga enerjisi dönüştürücü gibi alanlara ilişkin yorumlar yapılmıştır.

Dikey ve eğimli duvar durumları içeren uzun dalgaların analitik çözümlerini tamamladıktan sonra Bölüm 4'te 3 Numaralı Yayın çerçevesinde, tezimizin özel durumu olan 30 Ekim 2020 İzmir Tsunamisi çalışmasına geçilmiştir. Kıyıya yakın çevrede tsunamiler, diğer doğal afetlerden daha az sıklıkta meydana gelseler bile son derece ölümcül olabilmektedir. Türkiye'nin İzmir ilinin yaklaşık 23 km güneyinde, Yunanistan'ın Samos adası açıklarında, 30 Ekim 2020'de saat 12:51 p.m UTC'de (2:51 GMT+03:00) 6,9 Mw büyüklüğünde bir deprem meydana gelmiştir. Bu depremin yarattığı tsunami olayı, 30 Ekim 2020 İzmir-Samos (Ege) tsunamisi olarak bilinmektedir ve bu tezde, gözlemsel verilere uygulanan bazı yapay zeka (AI) yaklaşımları kullanılarak bu tsunaminin hidrodinamikleri incelenmiştir. LSTM derin öğrenme algoritmasının tarihçesi, yapısı, içeriği ve çalışma prensibi hakkında kapsamlı bilgiler verilmiştir. Veri akışının; unutma, giriş ve çıkış kapılarının yanı sıra girişin dışında, bilginin aktarılıp aktarılmayacağını, saklanacağını veya unutulacağını belirleyen bir bellek hücresi ile mümkün olduğu açıklanmıştır.

Daha iyi anlatmak gerekirse UNESCO veri portalından Bodrum, Syros, Kos ve Kos Marina'nın çeşitli yerlerinden elde ettiğimiz tsunami zaman serilerinden yararlanılmıştır. Daha sonra, Uzun Kısa Süreli Bellek (LSTM) DL yaklaşımının Fourier spektrumu ve tsunamilerin zaman serisi tahmini için uygulanması ve sınırlamaları incelenmiştir. Daha belirgin olarak, açık deniz su yüzeyi yüksekliği dinamiklerinin öngörülebilirliği, bunların spektral frekans ve genlik özellikleri, tahminler için potansiyel başarı faktörleri ve kesin erken tahmin zaman ölçeklerinin iyileştirilmesi araştırılmıştır. Bunu yapmak için, bu çalışmada kullanılan veriler, astronomik gelgit etkisini ortadan kaldırmak için spektral bir teknik kullanılarak gelgitten arındırılmıştır. Bir FFT-IFFT tekniği bu amaçla kullanılmıştır. Güncellemeli LSTM'nin tsunami zaman serisi için düşük frekanslı bileşenleri tahmin etmede daha başarılı olduğu gösterilmiştir. Sonuçlarımızın uygulamaları ve kullanımıyla birlikte potansiyel çalışma seçenekleri de araştırılmıştır.

Bölüm 5'te Sonuç çerçevesinde bulgularımız rapor edilmiştir. Bulgularımız, koylarda ve limanlarda uzun dalga rezonansı ve yükselişinin yanı sıra dalga enerjisi odaklayıcıları ve rezonatörlerin incelenmesinde kullanılabilir. Bu tezde ulaşılan sonuçlar çerçevesinde duvar örülmesi, tarama ve heyelanın oluşturduğu geometri değişikliklerinin uzun dalga hidrodinamiği üzerindeki etkilerinin de araştırılması mümkündür. Ayrıca, bu tez çalışmasının bulgularından yararlanılarak, tsunami erken uyarı sistemlerinde performans kazanımlarına ve dalga tırmanma zaman serileri, yatay ve sapma hızları gibi tsunaminin özelliklerine ilişkin çok sayıda araştırmaya öncülük edilebilir.

Laguerre, Chebyshev, Hermite veya Legendre polinomları cinsinden dikey veya eğimli duvar gibi farklı şekillerdeki ek geometriler için uzun dalga denkleminin çözümlerini elde etmek amacıyla çalışmamızın kullanımı önerilmiştir. Aynı şekilde tüm bu parametrelerin 1 Boyutlu yerine 2 Boyutlu olarak da çalışılabileceğinden bahsedilmiştir. Son olarak tez çalışmalarımızın bulgularını kullanarak gelecekte yapmayı planladığımız çalışmalar ve bunları nasıl yapacağımız Sonuç bölümünde detaylı olarak belirtilmiştir.

1. INTRODUCTION

One of the most difficult design challenges in the domains of ocean and coastal engineering is to mitigate the consequences of long waves, which produce huge volumes of wave runup, overwash, and inundation as well as oscillations with extremely long periods that are difficult to disperse. This well-researched topic has a wealth of literature [1]–[6]. Lamb published the linear long-wave equation for the first time in the first edition of his seminal book Hydrodynamics in 1879 [1], and Chrystal published it in a rough version in 1905 [2]. Since then, other studies have been conducted on these equations [1]–[6]. There are several research on the interaction of long-wave equations with sediments, beaches, barred beaches, and islands, such as those covered in [7]–[15], even though the majority of these works concentrate on the study of long-wave equations for various estuary, bay, and harbor geometries.

The scientific community has long investigated standing long waves with oblique incidence to the beach in great detail. One of the observed and investigated occurrences is the creation of several bars as a result of the reaction of loose sands beneath such standing waves. Lamb [1] provided the long-wave equation's solution for the reflection of usually incident, non-breaking waves originating from a horizontal beach slope, while Lettau [8] and Noda [16] showed that suspended sediments move toward the antinodes of such waves. The linear offshore bar development is shown to be accelerated by the deposition of sediments beneath standing wave nodes and antinodes, as anticipated by Bowen [9].

Munk [7] gave the phenomena of long-period progressive waves on the beach, which had been noticed for the first time until then, the name "surf beat." The mechanism of incident wind wave groups driving a second-order, long-period wave that is moving at the wind wave group velocity has been studied by Longuet-Higgins and Stewart [10]. Gallagher [17] investigated how 37 wind waves interacted nonlinearly to generate surf beats. Smith and Sprinks [12] and Summerfield [18] have both used numerical methods to study long wave resonance and its scattering around circular islands. Ball [15] conducted an investigation of the behavior of waves of various orders flowing in various directions, whereas Eckart [14] analyzed the surface waves where the water depth varies.

The edge waves are one of the fascinating and important phenomena investigated within the framework of the long-wave equations [13,19]. Edge wave solutions are examined using the Frobenius series due to the vanishing depth-related singularity at the shoreline, and solutions for some situations turned out to be in the form of the Laguerre polynomials [13]. Furthermore, it is shown that coastal edge waves can be actuated in the infragravital region using a constrained approach that only considers low edge-wave mode numbers [17]. Bowen and Guza [20] expanded these findings to edge waves with high mode numbers. The fieldwork by Suhayda [11], in which it is also demonstrated that the energy spectrum and phase difference in standing waves is shown to be consistent with the linear long-wave theory formulated by Lamb [1], revealed the existence of infragravity waves with offshore surface profiles similar to the Bessel function solution. The consequences of wave interactions have also been studied using several nonlinear theories applied to edge waves [19,21]–[24].

Long waves are often employed in the fields of optical and sound engineering as well [25]–[28]. To resonate at particular excitation frequencies, the sound and optical resonators have been adjusted.

Long-wave equations and certain of their expansions are frequently used to simulate such events with a wide variety and complexity of geometries. Numerous basic geometries, such as uniform depth [1,3]–[6], linearly increasing depth or linearly varying width (pie-shaped beach) [1,3]–[6], some combinations of trenches with these sorts of simple geometries [3], parabolic and elliptical depth variations [1,3,4], have well-known solutions for long-wave equations.

For the forced linear shallow water problem, Liu et. al. [29] derived the analytical solutions in which long waves caused by shifting atmospheric pressure distributions as well as tsunamis caused by landslides have both been described using these solutions. Madsen and White [30] presented the findings of their research on the reflection and transmission properties of porous rubble-mound breakwaters. The linear computation of shoreline oscillations and subsequent nonlinear modification of the result using the Riemann method are done by Pelinovsky and Mazova for determining run-up characteristics [31]. Their linear formulation provides a solution to the non-one-dimensional issues of wave run-up on a beach [31]. Carrier and Greenspan examined a wave's behavior as it ascends a sloping beach in their research [32]. For several different waveforms, they found some explicit solutions to the equations of the non-linear inviscid shallow-water theory [32].

1.1 Bessel Function Solutions

Due to the nature of the case, the function ϕ that we must work with here, together with its initial differential coefficients, is finite, continuous, and single-valued throughout the whole region under consideration [1]. In the instance of incompressible fluids, which we will now examine in further detail, ϕ additionally has to meet the continuity equation, or as we will refer to it going forward, to put it succinctly [1],

$$\nabla^2\phi = 0 \tag{1.1}$$

throughout the entire region. Therefore, at all points outside of such masses, ϕ is now subject to mathematical conditions that are the same as those met by the potential of masses that attract or repel according to the law of the inverse square of the distance [1]. As a result, many of the conclusions reached in the theories of attraction, electrostatics, magnetism, and the steady flow of heat also apply to hydrodynamics [1]. We then go on to construct the most significant ones from this perspective [1].

Conveniently, the surface-integral of the normal velocity obtained across any surface—open or closed—in any situation of motion of an incompressible fluid is referred to as the "flux" over the surface [1]. Naturally, it is equal to the amount of fluid that crosses the surface in a given amount of time [1].

In the case of irrotational motion, the flux is determined by [1]

$$-\int\int \frac{\partial \phi}{\partial n} dS \tag{1.2}$$

where the element of the surface is denoted by δS and the appropriately drawn element of the normal to it by δn [1]. If a region is completely filled with liquid, there is no total flux across the boundary [1].

$$\int\int \frac{\partial \phi}{\partial n} dS = 0. \tag{1.3}$$

The normal's element δn is always drawn on one side, let's say inwards, and the integration covers the entire border [1]. This could be thought of as the equation of continuity in a more generalized form [1].

A tube, referred to as a tube of flow, is defined by the lines of motion that are drawn across the different points in an infinitesimal circuit [1]. At every point along the tube, the product of the velocity (q) and the cross-section (σ, for example), is constant [1].

If we would like, we can imagine that the fluid occupies the entire space in the form of tubes of flow, with each tube's size being modified such that the product $q\sigma$ is the same [1]. The number of tubes that span a surface determines the flux that flows across it [1]. As many tubes traverse the surface inwardly as there are outwards if the surface is closed, as expressed by Eq. (1.3) [1]. A line of motion hence cannot start or stop inside the fluid [1].

The equation $\nabla^2\phi = 0$ has solutions. The conventional approach to solving linear equations with constant coefficients can also yield [33]. The equation is therefore fulfilled by [1]

$$\phi = e^{\alpha x + \beta y + \gamma z} \tag{1.4}$$

or, more usually, by

$$\phi = f(\alpha x + \beta y + \gamma z) \tag{1.5}$$

given

$$\alpha^2+\beta^2+\gamma^2=0. \tag{1.6}$$

For instance, we might place [1]

$$\alpha,\beta,\gamma=1,\ \ i\cos\vartheta,\ \ i\sin\vartheta \tag{1.7}$$

or once more [1],

$$\alpha,\beta,\gamma=1,\ \ i\cosh u,\ \ i\sinh u. \tag{1.8}$$

It can be demonstrated that the superposition of the solutions of Eq. (1.5) [34] yields the most general solution feasible [1].

Introducing the cylindrical co-ordinates x, $\overline{\omega}$, and ω using Eq. (1.7) [1]

$$y=\overline{\omega}\cos\omega,\quad z=\overline{\omega}\sin\omega \tag{1.9}$$

we construct a symmetrical solution about the axis of x if we pick [1]

$$\phi=\frac{1}{2\pi}\int_0^{2\pi} f\left(x+i\overline{\omega}\cos(\vartheta-\omega)\right)d\vartheta. \tag{1.10}$$

Because the integration covers the entire circumference, it doesn't matter where ϑ originates, hence the formula can be expressed as follows [1,35]:

$$\phi=\frac{1}{2\pi}\int_0^{2\pi} f(x+i\overline{\omega}\cos\vartheta)\,d\vartheta=\frac{1}{\pi}\int_0^{\pi} f(x+i\overline{\omega}\cos\vartheta)\,d\vartheta. \tag{1.11}$$

This is noteworthy because, in terms of its values $f(x)$ at locations along this axis, it yields a value of ϕ that is symmetrical along the axis of x [1]. It can be demonstrated that in such a scenario, the values along any finite length of the axis fully dictate the form of ϕ [1,36].

We have the functions as special cases of Eq. (1.11) [1]

$$\frac{1}{\pi}\int_0^{\pi}(x+i\overline{\omega}\cos\vartheta)^n\,d\vartheta,\quad \frac{1}{\pi}\int_0^{\pi}(x+i\overline{\omega}\cos\vartheta)^{-n-1}\,d\vartheta \tag{1.12}$$

where it is assumed that n is integral [1]. These harmonics are finite solid across the unit sphere and decrease to r^n and r^{-n-1} for $\overline{\varpi} = 0$ [1]. Therefore, they must be identical to $P_n(\mu)r^n$ and $P_n(\mu)r^{-n-1}$, respectively [1]. As a result, we acquire the forms [1]

$$P_n(\mu) = \frac{1}{\pi}\int_0^{\pi} \left(\mu + i\sqrt{(1-\mu^2)\cos\vartheta}\right)^n d\vartheta \tag{1.13}$$

$$P_n(\mu) = \frac{1}{\pi}\int_0^{\pi} \frac{d\vartheta}{\left(\mu + i\sqrt{(1-\mu^2)\cos\vartheta}\right)^{n+1}} \tag{1.14}$$

initial contributions were made by Laplace [37] and Jacobi [38], respectively.

With respect to the previously introduced cylindrical co-ordinates $x, \overline{\varpi}, \omega$, the equation $\nabla^2\phi = 0$ uses the format [1]

$$\frac{\partial^2\phi}{\partial x^2} + \frac{\partial^2\phi}{\partial\overline{\varpi}^2} + \frac{1}{\overline{\varpi}}\frac{\partial\phi}{\partial\overline{\varpi}} + \frac{1}{\overline{\varpi}^2}\frac{\partial^2\phi}{\partial\omega^2} = 0. \tag{1.15}$$

Direct transformation is one way to do this, or you could just say that the element $\delta x.\delta\overline{\varpi}.\overline{\varpi}\delta\omega$ has zero total flux across its border [1].

When symmetry exists around the axis of x, the equation takes on a distinct form. Then, $\phi = e^{\pm kx}\chi(\overline{\varpi})$ is a specific solution, given [1]

$$\chi''(\overline{\varpi}) + \frac{1}{\overline{\varpi}}\chi'(\overline{\varpi}) + k^2\chi(\overline{\varpi}) = 0. \tag{1.16}$$

This is the zero-order differential equation for "Bessel's Functions" [1]. Naturally, the total of two definite functions of $\overline{\varpi}$, each multiplied by an arbitrary constant, makes up its full primal [1]. It is simple to find the finite solution for $\overline{\varpi} = 0$ in the form of an ascending series; it is typically represented by $CJ_0(k\overline{\varpi})$ [1]

$$J_0(\zeta) = 1 - \frac{\zeta^2}{2^2} + \frac{\zeta^2}{2^2.4^2} - ... \tag{1.17}$$

Thus, we acquire the solutions for $\nabla^2\phi = 0$ of the following types [1,39]

$$\phi = e^{\pm kx} J_0(k\varpi). \tag{1.18}$$

One may notice that the stream function's corresponding value is [1]

$$\psi = \pm\varpi e^{\pm kx} J_0'(k\varpi). \tag{1.19}$$

Eq. (1.18) is equivalent to [1]

$$\phi = \frac{1}{\pi}\int_0^\pi e^{\pm k(x+i\varpi\cos\vartheta)}\, d\vartheta \tag{1.20}$$

due to

$$J_0(\zeta) = \frac{1}{\pi}\int_0^\pi \cos(\zeta\cos\vartheta)\, d\vartheta = \frac{1}{\pi}\int_0^\pi e^{i\zeta\cos\vartheta}\, d\vartheta \tag{1.21}$$

as may be confirmed by integrating term by term and developing the cosine [1].

Once more, when the order (n) is made infinite, Eq. (1.18) may also be recognized as the limiting form assumed by a spherical solid zonal harmonic, provided that the origin's distance from the point under consideration is also made infinitely great, with the two infinities being subject to a specific relation [1,36].

So that we can take

$$\phi = \frac{r^n}{\alpha^n} P_n(\mu) = \left(1 + \frac{x}{\alpha}\right)^n \chi_n(\varpi) \tag{1.22}$$

where x and ϖ have been given temporary new meanings, namely [1]

$$r = \alpha + x, \quad \varpi = 2\alpha \sin\frac{1}{2}\theta \tag{1.23}$$

while

$$\chi_n(\varpi) = 1 - \frac{n(n+1)}{2^2}\frac{\varpi}{\alpha^2} + \frac{(n-1)n(n+1)(n+2)}{2^2.4^2}\frac{\varpi^4}{\alpha^4} - \dots \tag{1.24}$$

The symbols x and ϖ will revert to their original meanings if we now set $k = n/\alpha$ and assume that α and n become infinite while k remains finite. This will allow us to recreate Eq. (1.18) with the upper sign in the exponential. We acquire the lower sign if we begin with [1]

$$\phi = \frac{\alpha^{n+1}}{r^{n+1}} P_n(\mu). \tag{1.25}$$

An arbitrary function of ϖ can be expressed in terms of the Bessel's Function of zero order using the same approach [1,40]. It is possible to expand any latitude function on a sphere's surface in spherical zonal harmonics, so [1]

$$F(\mu) = \Sigma \left(n + \frac{1}{2}\right) P_n(\mu) \int_{-1}^{1} F(\mu') P_n(\mu')\, d\mu'. \tag{1.26}$$

If we indicate the length of the chord drawn from the sphere's pole ($\theta = 0$) to the variable point by ϖ, we obtain [1]

$$\varpi = 2\alpha \sin\frac{1}{2}\theta, \quad \varpi\delta\varpi = -\alpha^2 \delta\mu. \tag{1.27}$$

Here α is the radius. The formula can be expressed as [1]

$$f(\varpi) = \frac{1}{\alpha^2} \Sigma \left(n + \frac{1}{2}\right) H_n(\varpi) \int_0^{2\alpha} f(\varpi') H_n(\varpi') \varpi'\, d\varpi' \tag{1.28}$$

$$f(\varpi) = F(\mu), \;\; H_n(\varpi) = P_n(\mu). \tag{1.29}$$

If we now place [1]

$$k = \frac{n}{\alpha}, \;\; \delta k = \frac{1}{\alpha} \tag{1.30}$$

and ultimately render α infinite, which brings us to the significant theorem (see to [41]) [1]:

$$f(\varpi) = \int_0^{\infty} J_0(k\varpi) k\, dk \int_0^{\infty} f(\varpi') J_0(k\varpi') \varpi'\, d\varpi'. \tag{1.31}$$

1.2 Free Oscillation Period Examples

Wilson has presented the outcomes for a number of geometries for complex one-dimensional basins, to determine the period of seiching with using a modified Merian formula as it shown in Figs. 1.1 and 1.2 [42].

Basin Type		Profile Equation	Periods of Free Oscillation				
			Fundamental	Mode Ratios T_n/T_1			
Description	Dimensions		T_1	$n = 1$	2	3	4
Rectangular	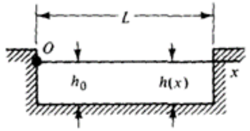	$h(x) = h_0$	$\frac{2L}{\sqrt{gh_0}}$	1.000	0.500	0.333	0.250
Triangular (isosceles)	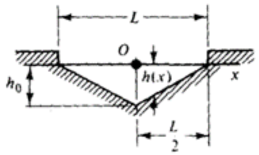	$h(x) = h_0\left(1 - \frac{2x}{L}\right)$	$1.305\,\frac{2L}{\sqrt{gh_0}}$	1.000	0.628	0.436	0.343
Parabolic	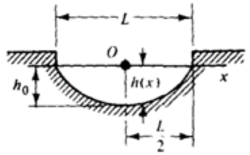	$h(x) = h_0\left(1 - \frac{4x^2}{L^2}\right)$	$1.110\,\frac{2L}{\sqrt{gh_0}}$	1.000	0.577	0.408	0.316

Figure 1.1 : Free oscillation periods of simple geometries (constant width) part 1 [5,42].

Quartic	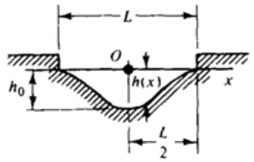	$h(x) = h_0\left(1 - \frac{4x^2}{L^2}\right)^2$	$1.242\,\frac{2L}{\sqrt{gh_0}}$	1.000	0.686	0.500	0.388
Triangular (right-angled)	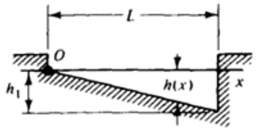	$h(x) = \frac{h_1 x}{L}$	$1.640\,\frac{2L}{\sqrt{gh_1}}$	1.000	0.546	0.377	0.288
Coupled, rectangular	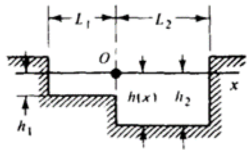	$h(x) = h_1\ (x < 0)$ $h(x) = h_2\ (x > 0)$ $\left(\frac{h_1}{h_2} = \frac{1}{4}\right)$	$\frac{L_1}{L_2} = \frac{1}{2}$ $\quad \frac{4L_2}{\sqrt{gh_2}}$	1.000	0.500	0.250	0.125
			$\frac{L_1}{L_2} = \frac{1}{3}$ $\quad \frac{3.13L_2}{\sqrt{gh_2}}$	1.000	0.559	0.344	0.217
			$\frac{L_1}{L_2} = \frac{1}{4}$ $\quad \frac{2.73L_2}{\sqrt{gh_2}}$	1.000	0.579	0.367	0.252
			$\frac{L_1}{L_2} = \frac{1}{8}$ $\quad \frac{2.31L_2}{\sqrt{gh_2}}$	1.000	0.525	0.371	0.279

Figure 1.2 : Free oscillation periods of simple geometries (constant width) part 2 [5,42].

1.3 Laguerre Polynomials

According to Eckart [14] and Berkhoff [43], the linear equations describing the motion of water waves can be roughly expressed as follows:

$$\nabla(p\nabla\eta) + \sigma^2 q\eta = 0 \tag{1.32}$$

considering σ-frequency monochromatic waves in water with local depth $h(x,y)$.

In this case, the wave profile is represented by $\eta(x,y,t)$, while p and q are provided by [13]:

$$q = \frac{1}{2}\left(1 + \frac{2kh}{\sinh 2kh}\right) = \frac{C_g}{C} \tag{1.33}$$

$$p = gh\frac{\tanh kh}{kh}q = CC_g \tag{1.34}$$

where k is the wave number determined by the dispersion relationship in the linear theory:

$$\sigma^2 = gk\tanh kh. \tag{1.35}$$

Eq. (1.32) is often known as the "mild slope" equation since it is derived on the assumption that the bottom gradient is a tiny quantity when scaled by the water wavelength. If the typical vertical component (hyperbolic cosine) of the solution is accepted, Eq. (1.32) simplifies to the shallow-water wave equation in shallow water of constant depth and also offers exact linear solutions in deep water. Solutions with variable depths are only approximations. Smith and Sprinks [12] provided evidence for the model's efficacy in predicting reflection and transmission coefficients over a topographic step as well as edge waves on a plane beach, showing that the model is not overly sensitive to deviations from the hypotheses that were used to derive it [13].

Eq. (1.32) may be simplified to the following by assuming that waves have sinusoidal longshore profiles with wave number λ and water depth is uniform in the longshore direction:

$$\frac{d}{dx}\left(p\frac{d\eta}{dx}\right)+(\sigma^2 q-\lambda^2 p)\eta=0 \tag{1.36}$$

where x is the offshore-oriented coordinate. Edge-wave dispersion estimated using Eq. (1.36) for the case of a plane beach has been demonstrated by Smith and Sprinks [12] to nearly match Ursell's precise solution [19]:

$$\sigma^2=g\lambda\sin[(2n+1)m]; \qquad n=0,1,2,\ldots \tag{1.37}$$

where m defines the beach slope and n defines the edge-wave mode number. The solution of the equation $\eta(x,y,t)$ has the following form in shallow water [14]:

$$\eta=\alpha L_n(2\lambda x)e^{-\lambda x}\cos(\lambda y-\sigma t) \tag{1.38}$$

for a progressive wave, where L_n is the Laguerre polynomial of order n and α is the coastline amplitude. For the shallow-water solution, the frequency and longshore wave number are connected by a partway modified dispersion relation [13]:

$$\sigma^2=g\lambda(2n+1)m; \qquad n=0,1,2,\ldots \tag{1.39}$$

The Sturm-Liouville system's eigenvalues and eigenvectors are represented by the λ's and η's for each of the n solutions in Eq. (1.36).

Ball [15] has also found a solution for the shallow-water motion equations for the situation of an exponentially shaped beach. Holman and Bowen [23] state that numerical methods for deriving solutions to the motion equations, which in this instance are represented by the mild-lope equation, Eq. (1.36), must be used for the case of real bottoms with varied depth profiles. Eq. (1.36) was viewed as a Sturm-Liouville system in the Kirby et al.'s work [13] in order to tackle the numerical challenge. Eq. (1.36) was made nondimensional by the addition of nondimensional variables:

$$\widetilde{x} = \frac{\sigma^2 x}{gm} \tag{1.40}$$

$$\widetilde{h} = \frac{\sigma^2 h}{gm} \tag{1.41}$$

$$\widetilde{\lambda} = \frac{gm}{\sigma^2}\lambda \tag{1.42}$$

$$\widetilde{\eta} = \frac{\sigma^2}{gm}\eta. \tag{1.43}$$

With the replacement, the surface profile was altered:

$$\xi = \widetilde{\eta}\widetilde{x} \tag{1.44}$$

by eliminating the dimensionless symbol $\widetilde{}$, the equation for ξ is obtained as follows:

$$px^2\xi_{xx} + (x^2 p_x - 2xp)\xi_x + [2p - xp_x + x^2(q - \lambda^2 p)]\xi = 0. \tag{1.45}$$

When η is supposed to be small at big x (offshore), the value of ξ decreases until it is zero as x approaches toward infinity. With the understanding that the highest desirable edge-wave mode for the plane beach situation must be let to decrease in an unbounded manner in the offshore direction prior to x_{MAX}, a maximum offshore distance, x_{MAX}, was then wisely selected for computational reasons. Thus, homogeneous boundary conditions become applicable to the altered surface profile [13]:

$$\xi = 0; x = 0, x_{MAX}. \tag{1.46}$$

The replacement shifted the x coordinate:

$$x = e^{\alpha z} - 1 \tag{1.47}$$

where $\alpha = 0.25$ which is the stretching factor to give the nearshore area more specificity. Eq. (1.36) changes to:

$$\begin{aligned}
p(e^{\alpha z}-1)^2\xi_{zz} &+ \{(e^{\alpha z}-1)^2 p_z - \alpha[(e^{\alpha z}-1)^2 + 2e^{\alpha z}(e^{\alpha z}+1)]p\}\xi_z \\
&+ \{2\alpha^2(e^{\alpha z}-1)^2 p - \alpha e^{\alpha z}(e^{\alpha z}-1)p_z + \alpha^2 e^{2\alpha z}(e^{\alpha z}-1)^2 q\}\xi \\
&= \lambda^2\alpha^2 e^{2\alpha z}(e^{\alpha z}-1)^2 p\xi. \qquad (1.48)
\end{aligned}$$

A finite difference method is used to solve Eq. (1.48). It was decided to split the range $0 < z < z_{MAX}$ into I intervals, $1 < i < I$. Difference equations for each z_i, $2 \leq i \leq I-1$, were created utilizing central difference forms for the derivations of ξ. From the $(I-2)$ equations, ξ_1 and ξ_I were removed due of boundary conditions. The system that results has the following form [13]:

$$A\xi = \lambda^2 B\xi \qquad (1.49)$$

where ξ defined as a vector and A and B are defined as matrices

$$\xi = (\xi_2, \xi_3, \xi_4, ..., \xi_{I-1}) = (\xi(z_2), \xi(z_3), \xi(z_4), ..., \xi(z_{I-1})) \qquad (1.50)$$

In order to invert Eq. (1.49) for the $(I-2)$ values of λ and related eigenvectors ξ, the IMSL procedure EIGZF was used [13]. The water-surface profile for each eigenvalue λ_i was then determined by writing a finite difference form of Eq. (1.36) around the point x_2, utilizing the formerly determined values of η_2 and η_3, and dividing each value in the related ξ_i array by the local offshore distance $x_i\eta(x = O)$. Each numerically generated profile was normalized to have a coastline amplitude of unity [13].

By calculating Eq. (1.36) with λ set to zero, thus assuming an infinite longshore wavelength, standing wave profiles were discovered [13]. Using the IMSL function DVERK, Runge-Kutta integration was used to find solutions [13]. Solutions matched Lamb's Eq. (1.75) Bessel function solution for the situation of a plane beach.

Profiles and wavelengths obtained from the model equation for a beach with a slope of $m = 0.0085$ were evaluated against profiles and wavelengths obtained by changing the shallow-water variables p and q in the model. This was done to determine how well the model equation predicted shallow-water wavelengths [13].

$$p = CC_g = gh. \tag{1.51}$$

$$q = C_g/C = 1. \tag{1.52}$$

The linear shallow-water equation is created by substituting Eqs. (1.51) and (1.52) into Eq. (1.36):

$$\frac{d}{dx}\left(gh\frac{d\eta}{dx}\right) + (\sigma^2 - \lambda^2 gh)\eta = 0. \tag{1.53}$$

1.4 Gauss Hypergeometric Series

The equation $\nabla^2\phi = 0$ is originally written in terms of spherical polar co-ordinates, r, θ, ω, in Laplace's original inquiry [44], where [1]

$$x = r\cos\theta, \quad y = r\sin\theta\cos\omega, \quad z = r\sin\theta\sin\omega. \tag{1.54}$$

Applying the Eq. (1.3) theorem on the surface of a volume-element $r\delta\theta.r\sin\theta\delta\omega.\delta r$ is the easiest method for performing the transformation [1]. Consequently, the flux difference between the two faces perpendicular to r is [1]

$$\frac{\partial}{\partial r}\left(\frac{\partial\phi}{\partial r}.r\delta\theta.r\sin\theta\delta\omega\right)\delta r. \tag{1.55}$$

In a similar manner, we discover that for the two faces perpendicular to the meridian ($\omega =$ constant) [1],

$$\frac{\partial}{\partial\theta}\left(\frac{\partial\phi}{r\partial\theta}.r\sin\theta\delta\omega.\delta r\right)\delta\theta. \tag{1.56}$$

Additionally, given the two faces that are perpendicular to a latitude parallel ($\theta =$ constant) [1]

$$\frac{\partial}{\partial \omega}\left(\frac{\partial \phi}{r\sin\theta \partial \omega}.r\delta\theta.\delta r\right)\delta\omega. \tag{1.57}$$

Thus, moreover [1],

$$\sin\theta\frac{\partial}{\partial r}\left(r^2\frac{\partial \phi}{\partial r}\right)+\frac{\partial}{\partial \theta}\left(\sin\theta\frac{\partial \phi}{\partial \theta}\right)+\frac{1}{\sin\theta}\frac{\partial^2 \phi}{\partial \omega^2}=0. \tag{1.58}$$

Considering for instance that ϕ is homogeneous, of degree n, and placed [1]

$$\phi = r^n S_n \tag{1.59}$$

we acquire [1]

$$\frac{1}{\sin\theta}\frac{\partial}{\partial \theta}\left(\sin\theta\frac{\partial S_n}{\partial \theta}\right)+\frac{1}{\sin^2\theta}\frac{\partial^2 S_n}{\partial \omega^2}+n(n+1)S_n=0. \tag{1.60}$$

This is the spherical surface-harmonics general differential equation [1].

When we write $-n-1$ for n, the value of the product $n(n+1)$ remains unchanged, suggesting that [1]

$$\phi = r^{-n-1} S_n \tag{1.61}$$

also provides a solution for Eq. (1.58) [1].

The equation $\partial^2 S_n/\partial\omega^2$ vanishes in the situation of symmetry about the axis of x, and when we plug in $\cos\theta = \mu$, we obtain [1]

$$\frac{d}{d\mu}\left\{\left(1-\mu^2\right)\frac{dS_n}{d\mu}\right\}+n(n+1)S_n=0 \tag{1.62}$$

the spherical "zonal" harmonics differential equation [1,36]. This equation, which only has two terms of distinct dimensions in μ, is modified for series integration [1]. Therefore, we get

$$S_n = A\left\{1-\frac{n(n+1)}{1.2}\mu^2+\frac{(n-2)n(n+1)(n+3)}{1.2.3.4}\mu^4-...\right\}$$
$$+B\left\{\mu-\frac{(n-1)(n+2)}{1.2.3}\mu^3+\frac{(n-3)(n-1)(n+2)(n+4)}{1.2.3.4.5}\mu^5-...\right\}. \quad (1.63)$$

The series that are shown here belong to the category known as "hypergeometric" series; that is, if we write, following Gauss [1,45]

$$F(\alpha,\beta,\gamma,x)=1+\frac{\alpha.\beta}{1.\gamma}x+\frac{\alpha.\alpha+1.\beta.\beta+1}{1.2.\gamma.\gamma+1}x^2+\frac{\alpha.\alpha+1.\alpha+2.\beta.\beta+1.\beta+2}{1.2.3.\gamma.\gamma+1.\gamma+2}x^3+... \quad (1.64)$$

we have [1]

$$S_n = AF\left(-\frac{1}{2}n,\ \frac{1}{2}+\frac{1}{2}n,\ \frac{1}{2},\ \mu^2\right)+B\mu F\left(\frac{1}{2}-\frac{1}{2}n,\ 1+\frac{1}{2}n,\ \frac{3}{2},\ \mu^2\right). \quad (1.65)$$

Indeed, when x is between 0 and 1, the series of Eq. (1.64) is convergent; but, when $x=1$, it is convergent if, and only if [1],

$$\gamma-\alpha-\beta>0. \quad (1.66)$$

Here, we have [1]

$$F(\alpha,\beta,\gamma,1)=\frac{\Pi(\gamma-1).\Pi(\gamma-\alpha-\beta-1)}{\Pi(\gamma-\alpha-1).\Pi(\gamma-\beta-1)} \quad (1.67)$$

and the equivalent of Euler's $\Gamma(m+1)$ in Gauss's notation is $\Pi(m)$ [1].

The series of Eq. (1.64)'s degree of divergence when [1]

$$\gamma-\alpha-\beta<0 \quad (1.68)$$

as x gets closer to the value 1, is provided by the theorem [1,33]

$$F(\alpha,\beta,\gamma,x)=(1-x)^{\gamma-\alpha-\beta}F(\gamma-\alpha,\ \gamma-\beta,\ \gamma,x). \quad (1.69)$$

Given that the latter series will now be convergent when $x = 1$, we can observe that $F(\alpha,\ \beta,\ \gamma,\ x)$ diverges as $(1-x)^{\gamma-\alpha-\beta}$; that is, for values of x that are almost equal to unity, we have [1]

$$F(\alpha,\beta,\gamma,x) = \frac{\Pi(\gamma-1).\Pi(\alpha+\beta-\gamma-1)}{\Pi(\alpha-1).\Pi(\beta-1)}(1-x)^{\gamma-\alpha-\beta} \tag{1.70}$$

finally.

In the crucial situation where [1]

$$\gamma-\alpha-\beta = 0 \tag{1.71}$$

we might utilize the formula in this case [1]

$$\frac{d}{dx}F(\alpha,\beta,\gamma,x) = \frac{\alpha\beta}{\gamma}F(\alpha+1,\ \beta+1,\ \gamma+1,\ x) \tag{1.72}$$

hence, when used with Eq. (1.69), provides in the assumed [1]

$$\begin{aligned}\frac{d}{dx}F(\alpha,\beta,\gamma,x) =& \frac{\alpha\beta}{\gamma}(1-x)^{-1}.F(\gamma-\alpha,\ \alpha-\beta,\ \gamma+1,\ x)\\ =& \frac{\alpha\beta}{\gamma}(1-x)^{-1}.F(\alpha,\ \beta,\ \alpha+\beta+1,\ x).\end{aligned} \tag{1.73}$$

As $x = 1$, the final factor now converges, making $F(\alpha,\beta,\gamma,x)$ ultimately divergent as $\log(1-x)$. More specifically, we have, for x values close to this limit [1],

$$F(\alpha,\ \beta,\ \alpha+\beta,\ x) = \frac{\Pi(\alpha+\beta-1)}{\Pi(\alpha-1).\Pi(\beta-1)}\log\frac{1}{1-x}. \tag{1.74}$$

1.5 The Solution of the Long Wave Equation in the Power-Law Form

Lamb [1] and Chrystal [2] were the first to construct the linear long-wave equation, and several scholars have subsequently thoroughly investigated it, including [1]–[6]. Eq. (1.75) provides the long-wave equation.

$$\frac{g}{b(x)}\frac{d}{dx}\left[b(x)h(x)\frac{d\eta(x)}{dx}\right]-\eta_{tt}=0 \tag{1.75}$$

where g stands for gravitational acceleration, $\sigma=2\pi/T$ stands for angular frequency, T stands for the long-wave period, $h(x)$ stands for the depth (bathymetry) function, and $b(x)$ stands for the breadth (width) function of the estuary. The time harmonics, i.e.$\eta(x,t)=\widehat{\eta}(x)\cos(\sigma t)$, can be used to generate transient solutions once the solution for $\eta(x)$ has been found. It is widely known that Eq. (1.75) permits a solution in terms of the Bessel functions of order zero if either the depth function, $h(x)$, or the breadth function, $b(x)$, are utilized with linearly variable profiles [1].

However, there is limited research available for the nonlinear breadth and depth functions expressed as power-law nonlinearities. The long waves in an estuary with nonlinear depth and breadth functions in power-law form can be represented by the formulas $h(x)=c_1x^a$ and $b(x)=c_2x^c$. Here, we have some constants c_1,c_2,a,c. The advisor of this thesis, [46], has lately examined the long wave equation solution for such kinds of nonlinear geometries in the literature. The long-wave equation provided by Eq. (1.75) can be expressed as follows [46]:

$$\frac{d}{dx}\left[x^{a+c}\frac{d\widehat{\eta}(x)}{dx}\right]+\frac{\sigma^2}{c_1g}x^c\widehat{\eta}=0 \tag{1.76}$$

regarding the previously described geometries. This equation can be reduced to the Bessel equation via a power-law transformation [46,47]. After that, Eq. (1.75) admits solutions that are expressed in terms of Bessel-Z functions, which are presented as [46]

$$\widehat{\eta}(x)=x^{\nu/\alpha}Z_{|\nu|}\left(\alpha\sqrt{\left|\frac{\sigma^2}{c_1g}\right|}x^{1/\alpha}\right). \tag{1.77}$$

The parameters in this case are $\alpha=\frac{2}{2-a}$ and $\nu=\frac{1-a-c}{2-a}$. $Z_{|\nu|}$ represents the Bessel functions $J_{|\nu|}$ and $Y_{|\nu|}$ if $\frac{\sigma^2}{c_1g}>0$. On the other hand, the modified Bessel functions of $I_{|\nu|}$ and $K_{|\nu|}$ are represented by $Z_{|\nu|}$ if $\frac{\sigma^2}{c_1g}<0$. We investigate the solutions of the long wave equation in terms of the Bessel functions of $J_{|\nu|}$ and $Y_{|\nu|}$ since we limit our analysis to the situation $\frac{\sigma^2}{c_1g}>0$. Yet, our findings are readily generalized to the complex σ case, allowing for the derivation of solutions expressed in terms of modified

Bessel functions that display decay behavior. Furthermore, the solution to the long wave equation is known to be expressed in terms of the Cauchy-Euler series [47] if the depth function, $h(x)$, is parabolic.

To our knowledge, the advisor of this thesis is the only one who has lately solved long wave equations for the geometries where the depth and/or breadth profiles show nonlinear power-law changes [46]. To the best of our knowledge, however, if a solid vertical or inclined wall exists in the domain, the solution of long wave equations has not been researched for the aforementioned geometries. This thesis consists of 5 chapters, of which we are currently in Chapter 1, Introduction. In this chapter, we mentioned the known solutions of long waves over various breadth and depth variations. We expressed the Bessel Function solutions. We exemplified Free Oscillation Periods. We adverted Laguerre Polynomials and Gauss Hypergeometric Series. Finally, we introduced the solution of the Long Wave equation in the Power-Law form.

In Chapter 2 within the frame of Publication Number 1, we obtain the long-wave equation's exact analytical solutions for such profiles, which include solid vertical walls. The long wave equations' solutions are found in terms of Bessel-Z functions, but when a parabolic depth variation is taken into account, they take the form of the Cauchy-Euler series. We describe our results and give the analytical solution of long waves in various forms.

In Chapter 3 within the frame of Publication Number 2, we repeated the same work we did in Chapter 2 within the frame of Publication Number 1, that is, the long-wave equation's exact analytical solutions with vertical walls, this time for the case with inclined walls. First, in addition to the previous chapter on this issue, we give a broad review of partial reflection and its components, which we must take into account due to the inclined wall: the slope angle, phase lag, reflection coefficient, and Iribarren number. Then again we found the long wave equations' solutions in terms of Bessel-Z functions, but when a parabolic depth variation is taken into account, they take the form of the Cauchy-Euler series. Again we describe our results and give the analytical solution of long waves in various forms.

In Chapter 4 within the frame of Publication Number 3, we present the predictability of the 30 October 2020 İzmir-Samos Tsunami hydrodynamics and the enhancement of its early warning time by the LSTM Deep Learning network. To achieve this, we apply the LSTM deep learning network to forecast the tsunami water surface fluctuation time series at various stations and analyze their predictability. The spectrum properties of the predictions given by FFT procedures are discussed, together with the time series dynamics and root-mean-square-error (RMSE).

In Chapter 5, we present our conclusion. Our results can be used in the study of wave energy focusers and resonators, as well as long wave resonance and runup in harbors and bays. Within the framework of the conclusions drawn in this thesis, it is also possible to examine the impacts of wall building, dredging, and landslide-induced geometry changes on long-wave hydrodynamics. Again, by using the results in this thesis study, performance improvements can be made in tsunami early warning systems and many studies related to tsunami parameters such as the horizontal and excursion velocities, and run-up time series can be pioneered.

2. THE ANALYTICAL SOLUTIONS OF LONG WAVES OVER GEOMETRIES WITH LINEAR AND NONLINEAR VARIATIONS IN THE FORM OF POWER-LAW NONLINEARITIES WITH SOLID VERTICAL WALL[1]

The solution of the long wave equation for variations in the form of power-law nonlinearities is derived by one of the authors (see [46]). However, to our best knowledge, there is no study in the literature that examines similar geometries if there is a solid vertical wall within the geometry. With this motivation, we consider such nonlinear geometries with a solid vertical wall present in the domain and extending for $x \in [0, l_1]$. With such a solid vertical wall including the origin of the coordinate system, the singular point is eliminated from the domain, and Bessel functions of the second kind begin to appear in the solution. The schematic view of this geometry can be seen in Figs. 2.1, 2.5, 2.7, 2.9, 2.11, and 2.13 below. Such a geometry can be used to model the case of a harbor with a wall constructed before or after starting service, the case of a landslide, or a wave energy converter such as Wave Dragon with a wall.

For such a geometry, the corresponding boundary condition at wall (BC1) can be given as $\frac{\partial \eta(x,t)}{\partial x} = 0$ at $x = l_1$ for all t. The second boundary condition is the open ocean boundary condition (BC2) which can be formulated as $\eta(x,t) = \frac{H}{2}\cos(\sigma t)$ at $x = l_2$. These boundary conditions together with the long wave equation summarizes the boundary value problem (BVP) analyzed.

Letting $\sigma^2/c_1 g = k^2 > 0$ and thus taking $Z_{|\nu|}$ to be $J_{|\nu|}$ and $Y_{|\nu|}$, the solution of the long wave equation for arbitrary nonlinear geometry in the power-law form can be rewritten as

$$\widehat{\eta}(x) = Ax^{\nu/\alpha} J_{|\nu|}\left(\alpha k x^{1/\alpha}\right) + Bx^{\nu/\alpha} Y_{|\nu|}\left(\alpha k x^{1/\alpha}\right). \tag{2.1}$$

Using well-known derivative relations for the Bessel functions

$$\frac{\partial J_\nu(z)}{\partial z} = \frac{\nu}{z} J_\nu(z) - J_{\nu+1}(z) \tag{2.2}$$

[1]This chapter is based on the paper "Alan A. R., Bayındır, C. (2024). The Analytical Solutions of Long Waves Over Geometries with Linear and Nonlinear Variations in the Form of Power-Law Nonlinearities with Solid Vertical Wall, *Ocean Engineering,* 295, 117031.".

and

$$\frac{\partial Y_\nu(z)}{\partial z} = \frac{\nu}{z} Y_\nu(z) - Y_{\nu+1}(z) \tag{2.3}$$

the derivative of $\widehat{\eta(x)}$ can be computed as

$$\begin{aligned}\frac{\partial \widehat{\eta}(x)}{\partial x} = A &\left[\frac{\nu}{\alpha} x^{\frac{\nu-\alpha}{\alpha}} J_{|\nu|}\left(\alpha k x^{1/\alpha}\right) + \frac{|\nu|}{\alpha} x^{\frac{\nu-\alpha}{\alpha}} J_{|\nu|}\left(\alpha k x^{1/\alpha}\right) - k x^{\frac{\nu+1-\alpha}{\alpha}} J_{|\nu|+1}\left(\alpha k x^{1/\alpha}\right)\right] \\ &+ B \left[\frac{\nu}{\alpha} x^{\frac{\nu-\alpha}{\alpha}} Y_{|\nu|}\left(\alpha k x^{1/\alpha}\right) + \frac{|\nu|}{\alpha} x^{\frac{\nu-\alpha}{\alpha}} Y_{|\nu|}\left(\alpha k x^{1/\alpha}\right) - k x^{\frac{\nu+1-\alpha}{\alpha}} Y_{|\nu|+1}\left(\alpha k x^{1/\alpha}\right)\right].\end{aligned} \tag{2.4}$$

We give the solution of this BVP for two cases, first for nonnegative (case 1) and then for negative (case 2) values of $|\nu|$.

i) Case 1: If $\nu \geq 0$ then $|\nu| = \nu$, applying BC1 at $x = l_1$ and applying BC2 at $x = l_2$, after some algebra solution of this BVP can be given as

$$\begin{aligned}\eta(x,t) = \frac{H}{2 l_2^{\nu/\alpha}} &\left[\frac{-\Theta_2}{\Theta_1 Y_\nu\left(\alpha k l_2^{1/\alpha}\right) - \Theta_2 J_\nu\left(\alpha k l_2^{1/\alpha}\right)} x^{\nu/\alpha} J_\nu\left(\alpha k x^{1/\alpha}\right) \right. \\ &\left. + \frac{\Theta_1}{\Theta_1 Y_\nu\left(\alpha k l_2^{1/\alpha}\right) - \Theta_2 J_\nu\left(\alpha k l_2^{1/\alpha}\right)} x^{\nu/\alpha} Y_\nu\left(\alpha k x^{1/\alpha}\right)\right] \cos(\sigma t)\end{aligned} \tag{2.5}$$

where the first Θ_1 parameter is $\Theta_1 = \frac{2\nu}{\alpha} J_\nu\left(\alpha k {l_1}^{1/\alpha}\right) - k {l_1}^{1/\alpha} J_{\nu+1}\left(\alpha k {l_1}^{1/\alpha}\right)$ and the second Θ_2 parameter is $\Theta_2 = \frac{2\nu}{\alpha} Y_\nu\left(\alpha k {l_1}^{1/\alpha}\right) - k {l_1}^{1/\alpha} Y_{\nu+1}\left(\alpha k {l_1}^{1/\alpha}\right)$.

ii) Case 2: If $\nu < 0$ then $|\nu| = -\nu$, applying BC1 at $x = l_1$ and applying BC2 at $x = l_2$, after some algebra solution of this BVP can be given as

$$\begin{aligned}\eta(x,t) = \frac{H}{2 l_2^{\nu/\alpha}} &\left[\frac{-Y_{1-\nu}\left(\alpha k {l_1}^{1/\alpha}\right)}{\Theta} x^{\nu/\alpha} J_{-\nu}\left(\alpha k x^{1/\alpha}\right) \right. \\ &\left. + \frac{J_{1-\nu}\left(\alpha k {l_1}^{1/\alpha}\right)}{\Theta} x^{\nu/\alpha} Y_{-\nu}\left(\alpha k x^{1/\alpha}\right)\right] \cos(\sigma t)\end{aligned} \tag{2.6}$$

where $\Theta = J_{1-\nu}\left(\alpha k {l_1}^{1/\alpha}\right) Y_{-\nu}\left(\alpha k {l_2}^{1/\alpha}\right) - J_{-\nu}\left(\alpha k {l_2}^{1/\alpha}\right) Y_{1-\nu}\left(\alpha k {l_1}^{1/\alpha}\right)$.

In the next section, we analyze six different numerical examples of these solutions for various nonlinear geometries with a solid vertical wall.

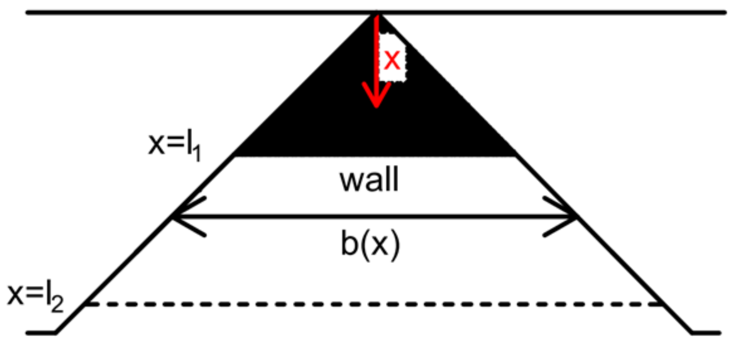

Figure 2.1 : Linear breadth variation with a wall.

2.1 Linear Breadth Variation ($b(x) = c_2 x^c$ with $c = 1$) with a Solid Vertical Wall

In this section, we analyze the case of linear breadth variation where a solid vertical wall extends from $x = 0$ to $x = l_1$ as illustrated in Fig. 2.1.

For this case, $c = 1$ and depth is a constant ($a = 0$) that lies within the limits imposed by the long wave theory. The Bessel-Z equation parameters given in Eq. (1.76) can be computed as $\alpha = \frac{2}{2-a} = 1$ and $\nu = \frac{1-a-c}{2-a} = 0$. Thus, the Bessel-Z equation given by Eq. (1.76) reduces to [46]

$$\frac{d^2\widehat{\eta}}{dx^2} + \frac{1}{x}\frac{d\widehat{\eta}}{dx} + k^2\widehat{\eta} = 0 \tag{2.7}$$

where $k^2 = \sigma^2/c_1 g$. The transient solution of the long wave equation with these parameters is in the form of

$$\eta(x,t) = [AJ_0(kx) + BY_0(kx)]\cos(\sigma t) \tag{2.8}$$

where $J_0(kx)$ and $Y_0(kx)$ are the Bessel functions of the first and second kind, with order 0, respectively. The Bessel functions of the first kind with the first three orders are illustrated in Fig. 2.2, and the Bessel functions of the second kind with the first three orders are illustrated in Fig. 2.3.

In order to find the coefficients A and B, we need to apply the BCs. The first BC (BC1) is the solid vertical wall BC. For a wall located at $x = l_1$, BC1 reads as $\frac{\partial \eta}{\partial x} = 0$ at $x = l_1$ for all t. Taking the derivative of Eq. (2.8) with respect to x, one gets

$$\frac{\partial \widehat{\eta}(x)}{\partial x} = [-AkJ_1(kx) - BkY_1(kx)] \tag{2.9}$$

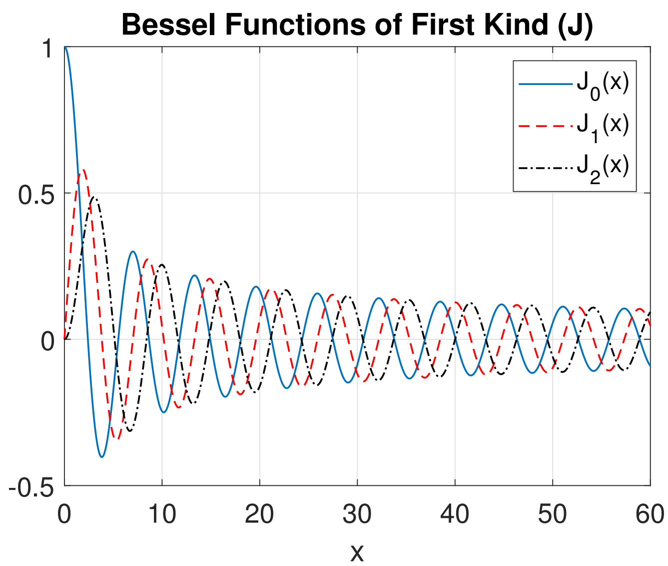

Figure 2.2 : Bessel $J_0(x)$, $J_1(x)$, $J_2(x)$ functions.

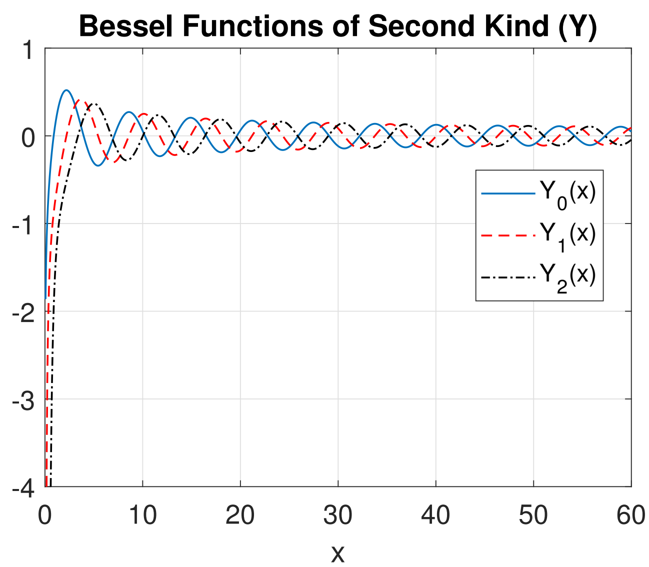

Figure 2.3 : Bessel $Y_0(x)$, $Y_1(x)$, $Y_2(x)$ functions.

where the relations of $\frac{\partial J_0(kx)}{\partial x} = -kJ_1(kx)$ and $\frac{\partial Y_0(kx)}{\partial x} = -kY_1(kx)$ are utilized. Applying BC1 one can obtain

$$\left.\frac{\partial \eta(x,t)}{\partial x}\right|_{x=l_1} = 0 = [-AkJ_1(kl_1) - BkY_1(kl_1)]\cos(\sigma t) \tag{2.10}$$

which yields

$$-AJ_1(kl_1) = BY_1(kl_1) \tag{2.11}$$

so that

$$A = \frac{-BY_1(kl_1)}{J_1(kl_1)}. \tag{2.12}$$

The open ocean BC (BC2) can be given at $x = l_2$ as

$$\eta(x,t) = \frac{H}{2}\cos(\sigma t) \tag{2.13}$$

where H is the wave height of the wave incoming from the ocean and it is taken to be $H = 1\ m$ throughout this paper and only non-breaking waves are considered. Applying BC2 to Eq. (2.8) yields

$$\eta(l_2,t) = [AJ_0(kl_2) + BY_0(kl_2)]\cos(\sigma t) = \frac{H}{2}\cos(\sigma t) \tag{2.14}$$

after eliminating the $\cos(\sigma t)$ terms one obtains

$$AJ_0(kl_2) + BY_0(kl_2) = \frac{H}{2}. \tag{2.15}$$

Substituting the value of A obtained in Eq. (2.12), one can obtain

$$\frac{-BY_1(kl_1)}{J_1(kl_1)}J_0(kl_2) + BY_0(kl_2) = \frac{H}{2}. \tag{2.16}$$

After eliminations one can obtain

$$B = \frac{HJ_1(kl_1)}{2\left[J_1(kl_1)Y_0(kl_2) - Y_1(kl_1)J_0(kl_2)\right]}. \tag{2.17}$$

If we substitute the B value that we found in Eq. (2.17) into Eq. (2.12), A becomes

$$A = -\frac{HY_1(kl_1)}{2\left[J_1(kl_1)Y_0(kl_2) - Y_1(kl_1)J_0(kl_2)\right]}. \tag{2.18}$$

If the coefficients given by Eqs. (2.17) and (2.18) are substituted back in Eq.(2.8), the solution of the long wave for the considered geometry becomes

$$\eta(x,t) = \frac{H}{2}\left(\frac{J_1(kl_1)Y_0(kx) - Y_1(kl_1)J_0(kx)}{J_1(kl_1)Y_0(kl_2) - Y_1(kl_1)J_0(kl_2)}\right)\cos(\sigma t). \tag{2.19}$$

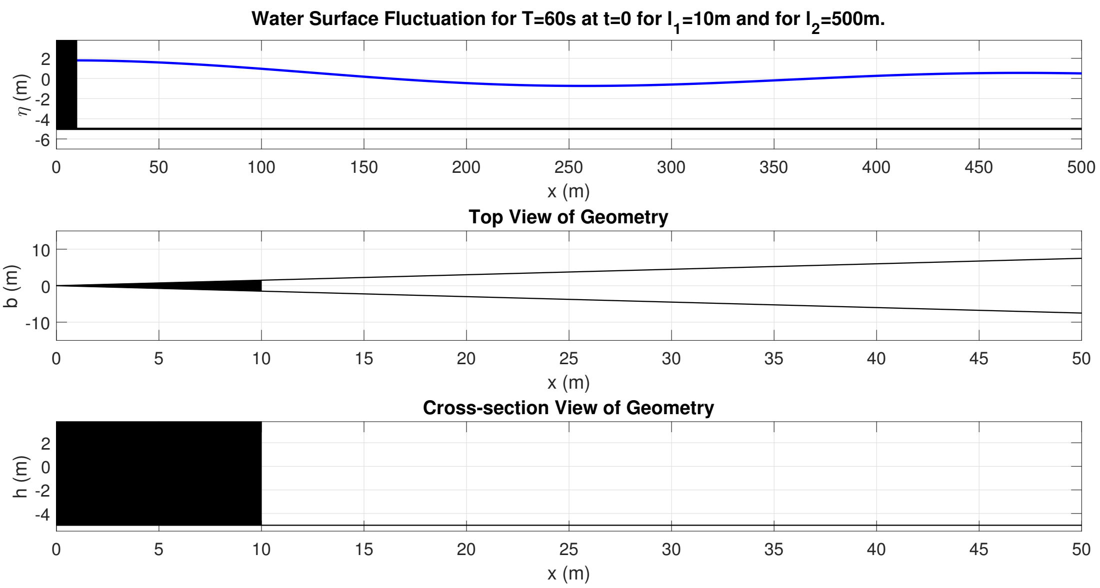

Figure 2.4 : Water surface fluctuation (η) for constant depth $h(x) = -5$ and linear breadth profile of $b(x) = 0.3x$ with a solid vertical wall.

The same result can be obtained by setting $\alpha = 1, \nu = 0$ in Eq. (2.5). The water surface fluctuation, η, of the long wave for the considered geometry is depicted in Fig. 2.4 for $T = 60\ s$, $c_1 = 5\ m$, $c_2 = 0.3$, $a = 0$, $c = 1$, $l_1 = 10\ m$ and $l_2 = 500\ m$ values at time $t = 0\ s$.

As expected, the first derivative of η vanishes at $x = l_1$ forming an antinode where the solid vertical wall is located. It is also possible to find the zeros and maximal points of η by computing the zeros of the Bessel functions numerically.

2.2 Linear Depth Variation ($h(x) = c_1 x^a$ with $a = 1$) with a Solid Vertical Wall

We continue our analysis by considering a linear depth variation in the form of $h(x) = c_1 x^a$ for $a = 1$, where the breadth remains unbounded. The illustration of such a geometry is presented in Fig. 2.5 where the effect of the solid vertical wall is included. The Bessel-Z equation parameters given in Eq. (1.76) can be computed as $\alpha = \frac{2}{2-a} = 2$ and $\nu = \frac{1-a-c}{2-a} = 0$ for this case.

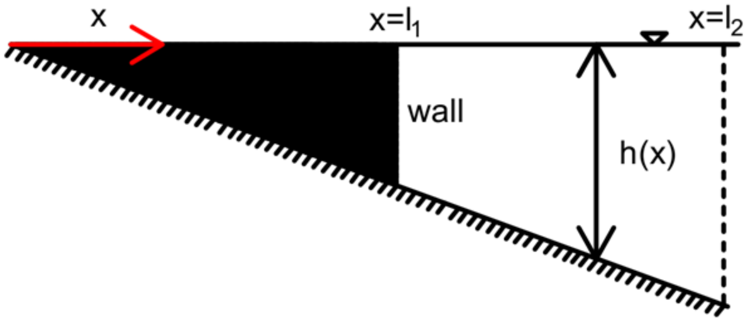

Figure 2.5 : Linear depth variation with a wall (cross-section view).

It is well-known that for such a linear depth variation the governing long wave equation admits a solution in terms of Bessel functions [5,46] which can be given as

$$\eta(x,t) = [AJ_0(2k\sqrt{x}) + BY_0(2k\sqrt{x})]\cos(\sigma t) \tag{2.20}$$

where $k^2 = \sigma^2/c_1 g$. As before, the wall boundary condition (BC1) is $\frac{\partial \eta}{\partial x} = 0$ at $x = l_1$ for all t. In order to impose BC1, we take the partial derivative of Eq. (2.20) with respect to x and obtain

$$\frac{\partial \eta(x,t)}{\partial x} = [-Akx^{-1/2}J_1(2k\sqrt{x}) - Bkx^{-1/2}Y_1(2k\sqrt{x})]\cos(\sigma t) \tag{2.21}$$

where we made use of the relations $\frac{\partial J_0(z)}{\partial z} = -J_1(z)$ and $\frac{\partial Y_0(z)}{\partial z} = -Y_1(z)$. Imposing BC1, one can obtain

$$\left.\frac{\partial \eta(x,t)}{\partial x}\right|_{x=l_1} = 0 = [-Akl_1{}^{-1/2}J_1(2k\sqrt{l_1}) - Bkl_1{}^{-1/2}Y_1(2k\sqrt{l_1})]\cos(\sigma t) \tag{2.22}$$

which yields

$$A = \frac{-BY_1(2k\sqrt{l_1})}{J_1(2k\sqrt{l_1})}. \tag{2.23}$$

In order to solve for A and B coefficients, the open ocean boundary condition (BC2) is applied. As before, BC2 reads as

$$\eta(x,t)|_{x=l_2} = \frac{H}{2}\cos(\sigma t). \tag{2.24}$$

Applying BC2 to Eq. (2.20)

$$\eta(l_2,t) = [AJ_0(2k\sqrt{l_2}) + BY_0(2k\sqrt{l_2})]\cos(\sigma t) = \frac{H}{2}\cos(\sigma t) \tag{2.25}$$

and after eliminating the $\cos(\sigma t)$ terms, and simultaneously solving Eqs. (2.23) and (2.25) for A and B coefficients, one can get

$$B = \frac{HJ_1(2k\sqrt{l_1})}{2\left[J_1(2k\sqrt{l_1})Y_0(2k\sqrt{l_2}) - Y_1(2k\sqrt{l_1})J_0(2k\sqrt{l_2})\right]}. \tag{2.26}$$

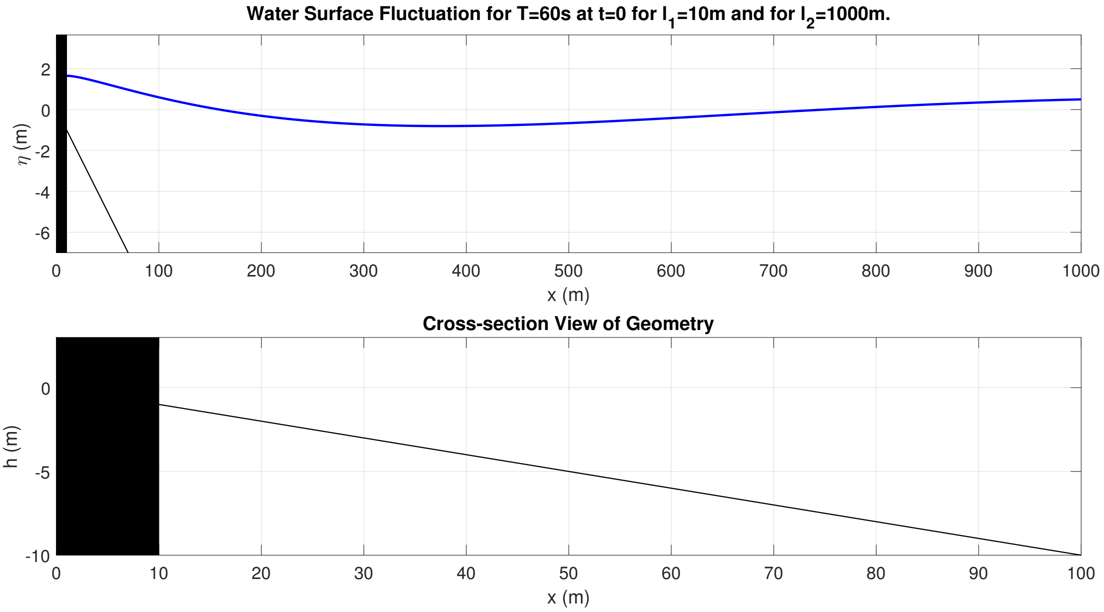

Figure 2.6 : Water surface fluctuation (η) for unbounded breadth and linear depth profile of $h(x) = 0.1x$ with a solid vertical wall.

If we substitute the B parameter found into Eq. (2.23), A becomes

$$A = -\frac{HY_1(2k\sqrt{l_1})}{2\left[J_1(2k\sqrt{l_1})Y_0(2k\sqrt{l_2}) - Y_1(2k\sqrt{l_1})J_0(2k\sqrt{l_2})\right]}. \tag{2.27}$$

If the calculated A and B parameters are substituted back into Eq. (2.20), the water surface fluctuation can be calculated as

$$\eta(x,t) = \frac{H}{2}\left(\frac{-Y_1(2k\sqrt{l_1})J_0(2k\sqrt{x})}{J_1(2k\sqrt{l_1})Y_0(2k\sqrt{l_2}) - Y_1(2k\sqrt{l_1})J_0(2k\sqrt{l_2})} + \frac{J_1(2k\sqrt{l_1})Y_0(2k\sqrt{x})}{J_1(2k\sqrt{l_1})Y_0(2k\sqrt{l_2}) - Y_1(2k\sqrt{l_1})J_0(2k\sqrt{l_2})}\right)\cos(\sigma t). \tag{2.28}$$

The same solution can also be obtained by setting $\alpha = 2, \nu = 0$ in Eq. (2.5).

The water surface fluctuation, η, of the long wave for the considered linear depth varying geometry is depicted in Fig. 2.6 for $T = 60\,s$, $c_1 = 0.1$, $a = 1$, $c = 0$, $l_1 = 10\,m$ and $l_2 = 1000\,m$ values at time $t = 0\,s$. The solution is independent from c_2. As before, it is possible to identify the antinodes and nodes of the η by computing the zeros of Bessel functions using a numerical procedure.

2.3 Linear Breadth and Depth Variation ($b(x) = c_2x^c$ with $c = 1$ and $h(x) = c_1x^a$ with $a = 1$) with a Solid Vertical Wall

Next, we turn our attention to the case where the breadth and depth variations are both linear, and a solid vertical wall exists in this wedge-shaped geometry which is illustrated in Fig. 2.7. For this case, since $a = 1$ and $c = 1$, the Bessel-Z equation parameters given in Eq. (1.76) can be computed as $\alpha = \frac{2}{2-a} = 2$ and $\nu = \frac{1-a-c}{2-a} = -1$. Thus, the Bessel-Z equation given by Eq. (1.76) reduces to

$$\frac{d}{dx}\left[x^2\frac{d\widehat{\eta}(x)}{dx}\right] + \frac{\sigma^2}{c_1g}x\widehat{\eta} = 0 \tag{2.29}$$

and the solution of this equation given by Eq. (1.77) becomes

$$\widehat{\eta}(x) = x^{-1/2}Z_1\left(2\sqrt{\left|\frac{\sigma^2}{c_1g}\right|}x^{1/2}\right). \tag{2.30}$$

As before, letting $\sigma^2/c_1g = k^2 > 0$ and thus taking Z_1 to be J_1 and Y_1, the solution of the long wave equation can be rewritten as

$$\widehat{\eta}(x) = Ax^{-1/2}J_1(2k\sqrt{x}) + Bx^{-1/2}Y_1(2k\sqrt{x}). \tag{2.31}$$

The wall boundary condition (BC1) is $\frac{\partial\eta}{\partial x} = 0$ at $x = l_1$ for all t. In order to impose BC1, we take the partial derivative of Eq. (2.31) with respect to x and obtain

$$\frac{\partial\widehat{\eta}(x)}{\partial x} = A\left(-kx^{-1}J_2(2k\sqrt{x})\right) + B\left(-kx^{-1}Y_2(2k\sqrt{x})\right) \tag{2.32}$$

where derivative relations for the Bessel functions given by Eqs. (2.2) and (2.3) are used. Imposing BC1 yields

$$A = \frac{-BY_2(2k\sqrt{l_1})}{J_2(2k\sqrt{l_1})}. \tag{2.33}$$

As before, the BC2 is the open ocean boundary condition. Applying BC2 yields

$$\eta|_{x=l_2} = \frac{H}{2}\cos(\sigma t) = \left(Al_2{}^{-1/2}J_1(2k\sqrt{l_2}) + Bl_2{}^{-1/2}Y_1(2k\sqrt{l_2})\right)\cos(\sigma t). \tag{2.34}$$

After simplifications one can obtain

$$\frac{H}{2} = \left[Al_2{}^{-1/2}J_1(2k\sqrt{l_2}) + Bl_2{}^{-1/2}Y_1(2k\sqrt{l_2})\right] \tag{2.35}$$

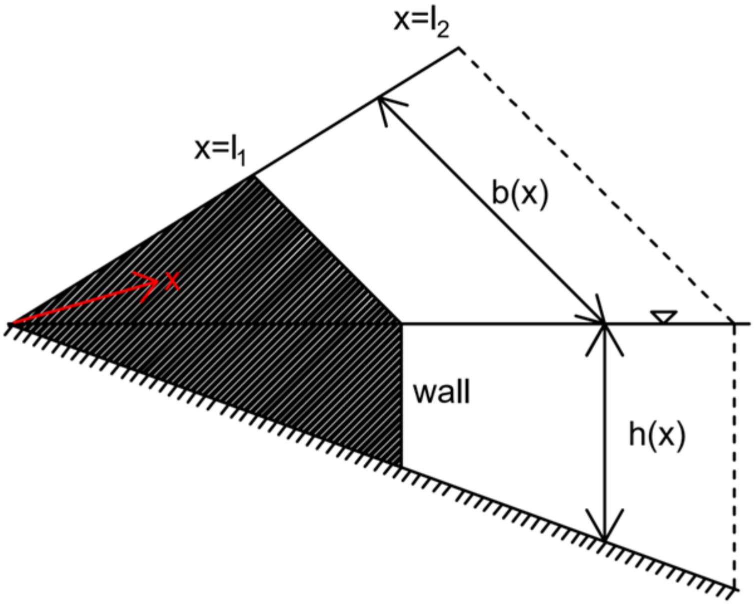

Figure 2.7 : Linear breadth and depth variation with a solid vertical wall.

which can be simultaneously solved with Eq. (2.33) to give

$$B = \frac{H}{2{l_2}^{-1/2}} \frac{J_2(2k\sqrt{l_1})}{\Delta} \tag{2.36}$$

where $\Delta = \left(J_2(2k\sqrt{l_1})Y_1(2k\sqrt{l_2}) - J_1(2k\sqrt{l_2})Y_2(2k\sqrt{l_1})\right)$. If we substitute the B parameter found here into Eq. (2.33), A becomes

$$A = -\frac{H}{2{l_2}^{-1/2}} \frac{Y_2(2k\sqrt{l_1})}{\Delta}. \tag{2.37}$$

Using the expressions for A and B, the solution in Eq. (2.31) can be expressed as

$$\eta(x,t) = \frac{H}{2{l_2}^{-1/2}} \left(\frac{J_2(2k\sqrt{l_1})}{\Delta} x^{-1/2} Y_1(2k\sqrt{x}) - \frac{Y_2(2k\sqrt{l_1})}{\Delta} x^{-1/2} J_1(2k\sqrt{x}) \right) \cos(\sigma t). \tag{2.38}$$

Similar to before, the same solution can be obtained by setting $\alpha = 2, \nu = -1$ in Eq. (2.5). This water surface fluctuation obtained for the linear breadth and depth variation is depicted in Fig. 2.8. The computational parameters are selected to be $T = 60\ s$, $c_1 = 0.15$, $c_2 = 0.3$, $a = 1$, $c = 1$, $l_1 = 10\ m$ and $l_2 = 2000\ m$ values at time $t = 0\ s$. In Fig. 2.8, it can be observed that an antinode is present at the solid vertical wall at $x = l_1$ thus the first derivative of η is vanishing. It is also observed that this wedge-shaped geometry has a significant resonator effect since η is magnified approximately ten times compared to its open ocean value. For the design

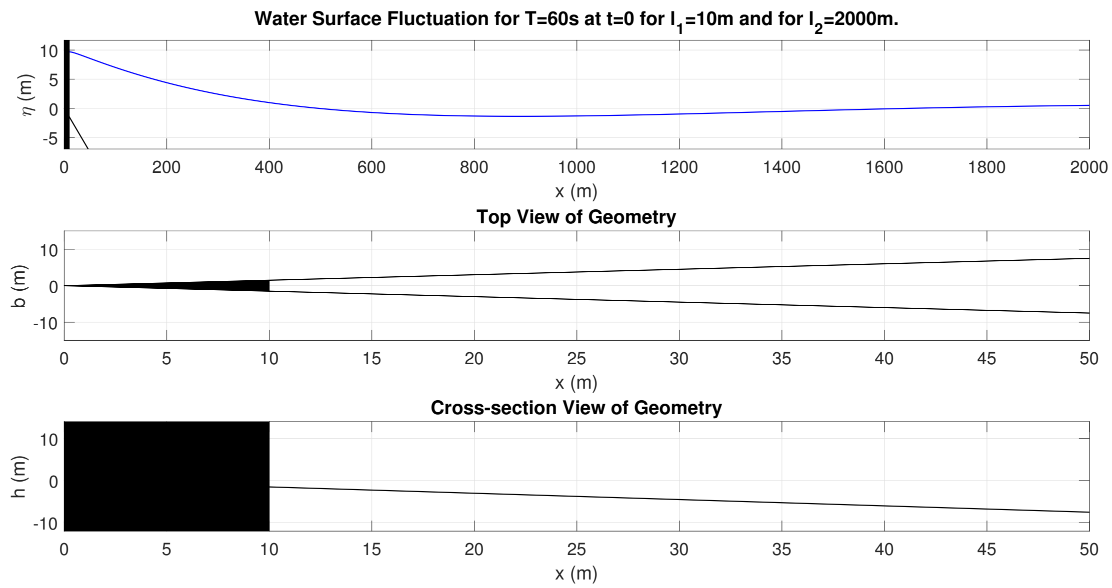

Figure 2.8 : Water surface fluctuation (η) for the profile with linear breadth variation $b(x) = 0.3x$ and linear depth variation $h(x) = 0.15x$ with a solid vertical wall.

of wave energy converters, such a geometry is a good candidate for resonating the water surface.

2.4 Nonlinear Breadth Variation ($b(x) = c_2 x^c$ with $c = 1/3$) with a Solid Vertical Wall

We now investigate the nonlinear breadth variation for the case of $c = 1/3$. The depth is constant ($a = 0$) with only restrictions imposed by the long wave theory, as before. Such a domain with a solid vertical wall is illustrated in Fig. 2.9. For this case, since $a = 0$ and $c = 1/3$, the Bessel-Z equation parameters given in Eq. (1.76) can be computed as $\alpha = \frac{2}{2-a} = 1$ and $\nu = \frac{1-a-c}{2-a} = 1/3$. Thus, the Bessel-Z equation given by Eq. (1.76) reduces to

$$\frac{d}{dx}\left[x^{1/3}\frac{d\widehat{\eta}(x)}{dx}\right] + \frac{\sigma^2}{c_1 g}x^{1/3}\widehat{\eta} = 0 \tag{2.39}$$

and the solution of this equation given by Eq. (1.77) becomes

$$\widehat{\eta}(x) = x^{1/3} Z_{1/3}\left(\sqrt{\left|\frac{\sigma^2}{c_1 g}\right|}x\right). \tag{2.40}$$

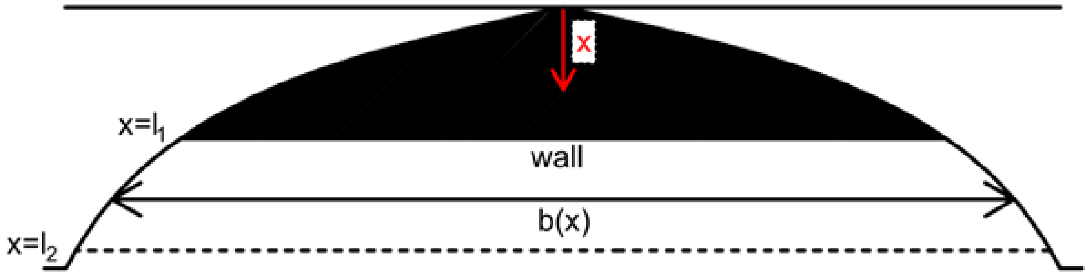

Figure 2.9 : Nonlinear breadth variation with a solid vertical wall.

As before, letting $\sigma^2/c_1 g = k^2 > 0$ and thus taking $Z_{1/3}$ to be $J_{1/3}$ and $Y_{1/3}$, the solution can be rewritten as

$$\widehat{\eta}(x) = Ax^{1/3} J_{1/3}(kx) + Bx^{1/3} Y_{1/3}(kx). \tag{2.41}$$

In order to impose BC1, we take the partial derivative of Eq. (2.41) with respect to x and obtain

$$\frac{\partial \widehat{\eta}(x)}{\partial x} = A\left[\frac{2}{3}x^{-2/3} J_{1/3}(kx) - kx^{1/3} J_{4/3}(kx)\right] + B\left[\frac{2}{3}x^{-2/3} Y_{1/3}(kx) - kx^{1/3} Y_{4/3}(kx)\right]. \tag{2.42}$$

Imposing BC1 yields $\left.\frac{\partial \eta}{\partial x}\right|_{x=l_1} = 0$

$$A = -B\frac{\left[\frac{2}{3}Y_{1/3}(kl_1) - kl_1 Y_{4/3}(kl_1)\right]}{\left[\frac{2}{3}J_{1/3}(kl_1) - kl_1 J_{4/3}(kl_1)\right]}. \tag{2.43}$$

As before imposing open ocean BC (BC2) gives

$$\eta|_{x=l_2} = \frac{H}{2}\cos(\sigma t) = \left(A{l_2}^{1/3} J_{1/3}(kl_2) + B{l_2}^{1/3} Y_{1/3}(kl_2)\right)\cos(\sigma t) \tag{2.44}$$

which yields

$$A{l_2}^{1/3} J_{1/3}(kl_2) + B{l_2}^{1/3} Y_{1/3}(kl_2) = \frac{H}{2}. \tag{2.45}$$

Solving Eqs. (2.43) and (2.45) simultaneously, the solution can be derived as

$$\begin{aligned}\eta(x,t) = \frac{H}{2{l_2}^{1/3}}\Bigg(&\frac{-\kappa_2}{Y_{1/3}(kl_2)\kappa_1 - J_{1/3}(kl_2)\kappa_2}x^{1/3} J_{1/3}(kx) \\ &+ \frac{\kappa_1}{Y_{1/3}(kl_2)\kappa_1 - J_{1/3}(kl_2)\kappa_2}x^{1/3} Y_{1/3}(kx)\Bigg)\cos(\sigma t)\end{aligned} \tag{2.46}$$

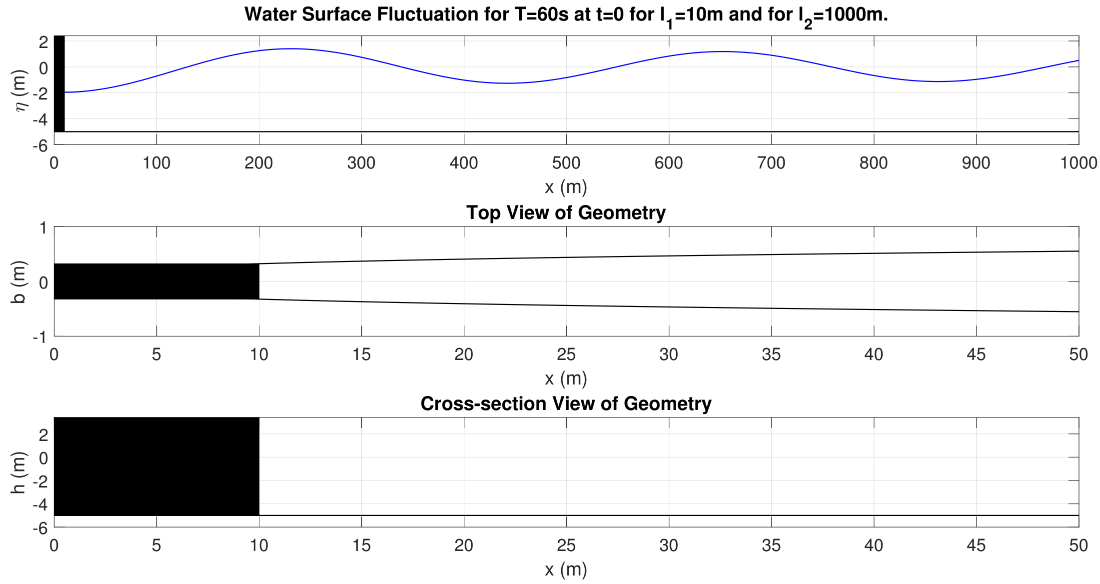

Figure 2.10 : Water surface fluctuation (η) for constant depth $h(x) = -5$ with nonlinear breadth variation $b(x) = 0.3x^{1/3}$ with a solid vertical wall.

where $\kappa_1 = \left[\frac{2}{3}J_{1/3}(kl_1) - kl_1 J_{4/3}(kl_1)\right]$ and $\kappa_2 = \left[\frac{2}{3}Y_{1/3}(kl_1) - kl_1 Y_{4/3}(kl_1)\right]$. The same solution can also be obtained by setting $\alpha = 1, \nu = 1/3$ in Eq. (2.5).

This water surface fluctuation obtained for the nonlinear breadth variation is depicted in Fig. 2.10. The computational parameters are selected to be $T = 60\ s$, $c_1 = 5\ m$, $c_2 = 0.3\ m^{2/3}$, $a = 0$, $c = 1/3$, $l_1 = 10\ m$ and $l_2 = 1000\ m$ values at time $t = 0\ s$. It can be observed that antinode appears on the wall, satisfying BC1, as well as the BC2.

2.5 Nonlinear Depth Variation ($h(x) = c_1 x^a$ with $a = 2/3$) with a Solid Vertical Wall

We continue our analysis by considering a nonlinear depth variation in the form of $h(x) = c_1 x^a$ for $a = 2/3$, where the breadth remains unbounded. As discussed in Eq. (1.77), such a selection of the depth profile corresponds to the equilibrium beach profile form first derived by [48]. The illustration of such a geometry is presented in Fig. 2.11, where the effect of the solid vertical wall is included.

For this case, since $a = 2/3$ and $c = 0$, the Bessel-Z equation parameters given in Eq. (1.76) can be computed as $\alpha = \frac{2}{2-a} = 3/2$ and $\nu = \frac{1-a-c}{2-a} = 1/4$. Thus, the

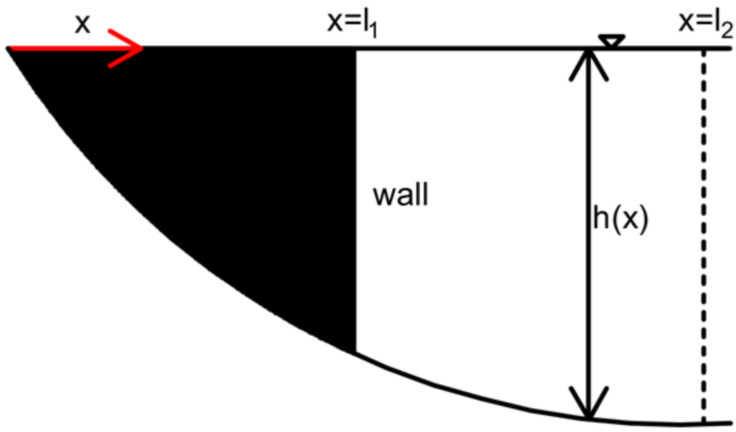

Figure 2.11 : Nonlinear depth variation with a solid vertical wall.

Bessel-Z equation given by Eq. (1.76) reduces to

$$\frac{d}{dx}\left[x^{2/3}\frac{d\widehat{\eta}(x)}{dx}\right]+\frac{\sigma^2}{c_1 g}\widehat{\eta}=0 \tag{2.47}$$

and Eq. (1.77) becomes

$$\widehat{\eta}(x)=x^{1/6}Z_{1/4}\left(\frac{3}{2}\sqrt{\left|\frac{\sigma^2}{c_1 g}\right|}x^{2/3}\right). \tag{2.48}$$

As before, letting $\sigma^2/c_1 g=k^2>0$ and thus taking $Z_{1/4}$ to be $J_{1/4}$ and $Y_{1/4}$, the solution can be rewritten as

$$\widehat{\eta}(x)=Ax^{1/6}J_{1/4}\left(\frac{3}{2}kx^{2/3}\right)+Bx^{1/6}Y_{1/4}\left(\frac{3}{2}kx^{2/3}\right). \tag{2.49}$$

The wall boundary condition (BC1) is $\frac{\partial\eta}{\partial x}=0$ at $x=l_1$ for all t. In order to impose BC1, we take the partial derivative of Eq. (2.49) with respect to x and obtain

$$\begin{aligned}\frac{\partial\widehat{\eta}(x)}{\partial x}&=A\left[\frac{1}{3}x^{-5/6}J_{1/4}\left(\frac{3}{2}kx^{2/3}\right)-kx^{-1/6}J_{5/4}\left(\frac{3}{2}kx^{2/3}\right)\right]\\&+B\left[\frac{1}{3}x^{-5/6}Y_{1/4}\left(\frac{3}{2}kx^{2/3}\right)-kx^{-1/6}Y_{5/4}\left(\frac{3}{2}kx^{2/3}\right)\right].\end{aligned} \tag{2.50}$$

Imposing BC1, $\left.\frac{\partial\eta}{\partial x}\right|_{x=l_1}=0$ yields

$$A=-B\frac{\left[\frac{1}{3}Y_{1/4}\left(\frac{3}{2}kl_1{}^{2/3}\right)-l_1{}^{2/3}kY_{5/4}(\frac{3}{2}kl_1{}^{2/3})\right]}{\left[\frac{1}{3}J_{1/4}(\frac{3}{2}kl_1{}^{2/3})-l_1{}^{2/3}kJ_{5/4}(\frac{3}{2}kl_1{}^{2/3})\right]} \tag{2.51}$$

As before imposing open ocean BC (BC2) gives

$$Al_2{}^{1/6}J_{1/4}\left(\frac{3}{2}kl_2{}^{2/3}\right)+Bl_2{}^{1/6}Y_{1/4}\left(\frac{3}{2}kl_2{}^{2/3}\right)=\frac{H}{2}. \tag{2.52}$$

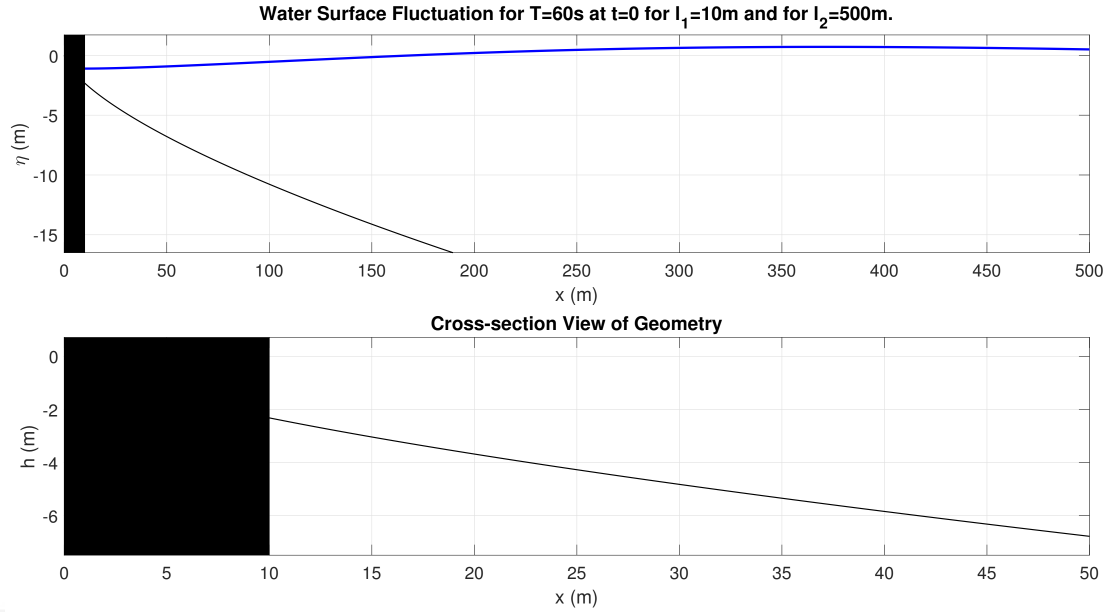

Figure 2.12 : Water surface fluctuation (η) for unbounded breadth and nonlinear depth profile of $h(x) = 0.5x^{2/3}$ with a solid vertical wall.

Solving Eqs. (2.51) and (2.52) simultaneously, the solution for the water surface fluctuation can be derived as

$$\eta(x,t) = \frac{H}{2{l_2}^{1/6}} \left[\frac{-\psi_2}{Y_{1/4}\left(\frac{3}{2}k{l_2}^{2/3}\right)\psi_1 - J_{1/4}\left(\frac{3}{2}k{l_2}^{2/3}\right)\psi_2} x^{1/6} J_{1/4}\left(\frac{3}{2}kx^{2/3}\right) \right.$$
$$\left. + \frac{\psi_1}{Y_{1/4}\left(\frac{3}{2}k{l_2}^{2/3}\right)\psi_1 - J_{1/4}\left(\frac{3}{2}k{l_2}^{2/3}\right)\psi_2} x^{1/6} Y_{1/4}\left(\frac{3}{2}kx^{2/3}\right) \right] \cos(\sigma t) \tag{2.53}$$

where $\psi_1 = \left[\frac{1}{3}J_{1/4}(\frac{3}{2}k{l_1}^{2/3}) - k{l_1}^{2/3}J_{5/4}(\frac{3}{2}k{l_1}^{2/3})\right]$ and $\psi_2 = \left[\frac{1}{3}Y_{1/4}(\frac{3}{2}k{l_1}^{2/3}) - k{l_1}^{2/3}Y_{5/4}(\frac{3}{2}k{l_1}^{2/3})\right]$. Again, the same solution can also be obtained by setting $\alpha = 3/2, \nu = 1/4$ in Eq. (2.5).

This water surface fluctuation obtained as the solution of the long wave problem for the nonlinear breadth variation is depicted in Fig. 2.12. The computational parameters are selected to be $T = 60\ s$, $c_1 = 0.5\ m^{1/3}$, $c_2 = 1$, $a = 2/3$, $c = 0$, $l_1 = 10\ m$ and $l_2 = 500\ m$ values at time $t = 0\ s$.

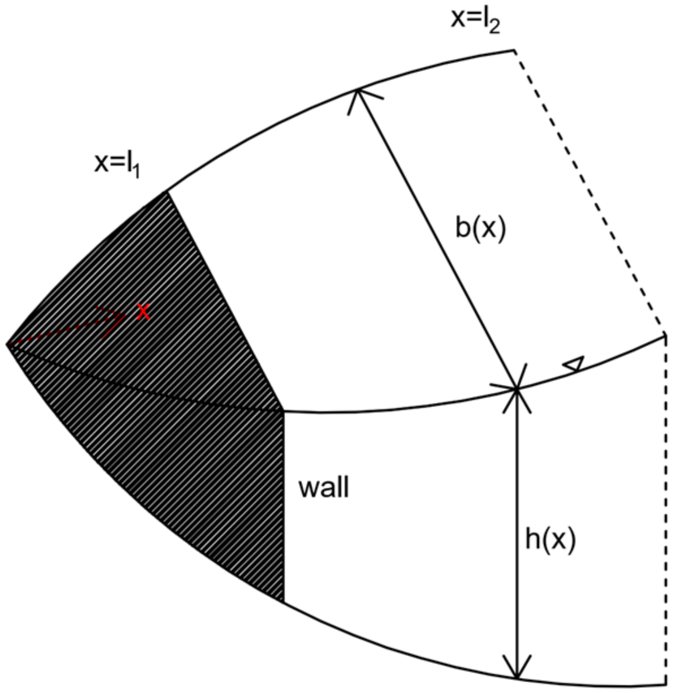

Figure 2.13 : Nonlinear breadth and depth variation with a solid vertical wall.

2.6 Nonlinear Breadth and Depth Variation ($b(x) = c_2 x^c$ with $c = 1/2$ and $h(x) = c_1 x^a$ with $a = 1/2$) with a Solid Vertical Wall

Lastly, we analyze the case where the breadth and depth variations are both nonlinear, and a solid vertical wall exists in this nonlinear wedge-shaped geometry which is illustrated in Fig. 2.13. For this case, since the parameters are selected to be $a = 1/2$ and $c = 1/2$, the Bessel-Z equation parameters given in Eq. (1.76) can be computed as $\alpha = \frac{2}{2-a} = 4/3$ and $\nu = \frac{1-a-c}{2-a} = 0$ and the Bessel-Z equation given by Eq. (1.76) reduce to

$$\frac{d}{dx}\left[x\frac{d\widehat{\eta}(x)}{dx}\right] + \frac{\sigma^2}{c_1 g}x^{1/2}\widehat{\eta} = 0 \tag{2.54}$$

and the solution of this equation given by Eq. (1.77) becomes

$$\widehat{\eta}(x) = Z_0\left(\frac{4}{3}\sqrt{\left|\frac{\sigma^2}{c_1 g}\right|}x^{3/4}\right). \tag{2.55}$$

As before, letting $\sigma^2/c_1 g = k^2 > 0$ and thus taking Z_0 to be J_0 and Y_0, the solution can be rewritten as

$$\widehat{\eta}(x) = AJ_0\left(\frac{4}{3}kx^{3/4}\right) + BY_0\left(\frac{4}{3}kx^{3/4}\right). \tag{2.56}$$

Taking the partial derivative of Eq. (2.31) with respect to x one can obtain

$$\frac{\partial\widehat{\eta}(x)}{\partial x} = -Akx^{-1/4}J_1\left(\frac{4}{3}kx^{3/4}\right) - Bkx^{-1/4}Y_1\left(\frac{4}{3}kx^{3/4}\right). \tag{2.57}$$

Imposing BC1, $\left.\frac{\partial\eta}{\partial x}\right|_{x=l_1} = 0$ yields

$$A = -B\frac{Y_1\left(\frac{4}{3}k{l_1}^{3/4}\right)}{J_1\left(\frac{4}{3}k{l_1}^{3/4}\right)}. \tag{2.58}$$

As before imposing open ocean BC (BC2) gives

$$AJ_0\left(\frac{4}{3}k{l_2}^{3/4}\right) + BY_0\left(\frac{4}{3}k{l_2}^{3/4}\right) = \frac{H}{2}. \tag{2.59}$$

Solving Eqs. (2.58) and (2.59) simultaneously, the solution for the water surface fluctuation can be derived as

$$\eta(x,t) = \frac{H}{2}\left[\frac{J_1\left(\frac{4}{3}k{l_1}^{3/4}\right)}{\Delta}Y_0\left(\frac{4}{3}kx^{3/4}\right) - \frac{Y_1\left(\frac{4}{3}k{l_1}^{3/4}\right)}{\Delta}J_0\left(\frac{4}{3}kx^{3/4}\right)\right]\cos(\sigma t) \tag{2.60}$$

where $\Delta = J_1\left(\frac{4}{3}k{l_1}^{3/4}\right)Y_0\left(\frac{4}{3}k{l_2}^{3/4}\right) - J_0\left(\frac{4}{3}k{l_2}^{3/4}\right)Y_1\left(\frac{4}{3}k{l_1}^{3/4}\right)$. Similar to before, the same solution can also be obtained by setting $\alpha = 4/3, \nu = 0$ in Eq. (2.5).

This water surface fluctuation obtained for the nonlinear breadth variation is depicted in Fig. 2.14. The computational parameters are selected to be $T = 60\ s$, $c_1 = 0.3\ m^{1/2}$, $c_2 = 0.3\ m^{1/2}$, $a = 1/2$, $c = 1/2$, $l_1 = 10\ m$ and $l_2 = 1000\ m$ values at time $t = 0\ s$. Significant increase of η at the solid vertical wall compared to the open ocean can be observed, thus the geometry investigated in this part is another good candidate for resonating waves when deems necessary.

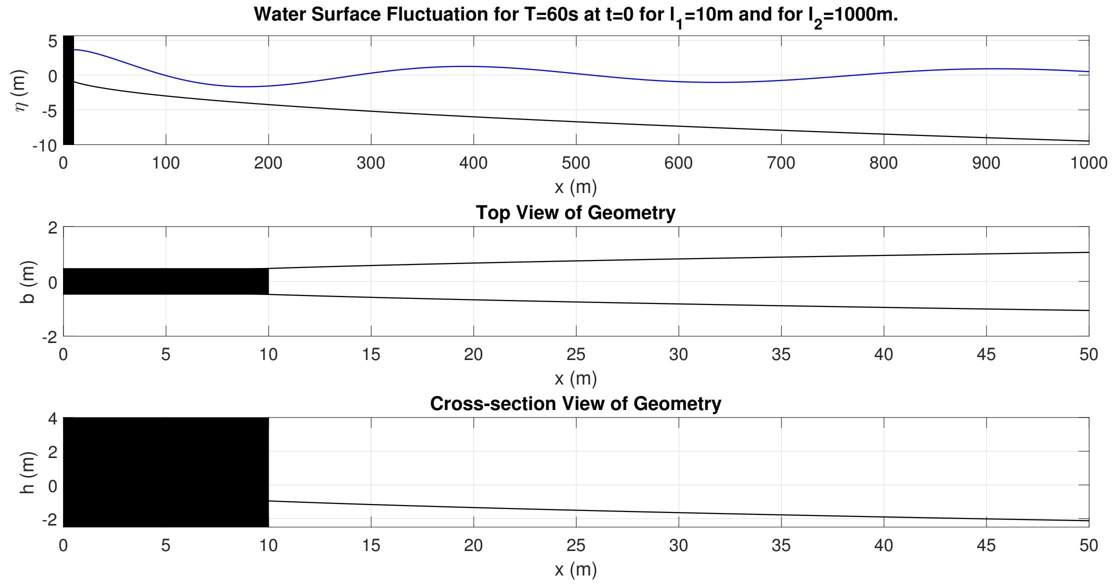

Figure 2.14 : Water surface fluctuation (η) for nonlinear breadth variation $b(x) = 0.3x^{1/2}$ and nonlinear depth variation $h(x) = 0.3x^{1/2}$ with a solid vertical wall.

2.7 Solutions in Terms of Cauchy-Euler Series for Geometries with Solid Vertical Wall

It is well-known that for a uniform estuary breadth and a parabolic bathymetry, the solutions of the long-wave equation given by Eq. (1.75) turn out to be in terms of the Cauchy-Euler series [47]. For any arbitrary breadth profile, this remains true for parabolic bathymetry in the form $h_{par}(x) = c_1x^2$, which is obtained by setting $a = 2$. For this case governing equation reduces to

$$x^2\widehat{\eta}_{xx} + (c+2)x\widehat{\eta}_x + \sigma^2/(c_1g)\widehat{\eta} = 0. \tag{2.61}$$

This equation is known as the Cauchy-Euler equation [47], which can be solved by assuming a solution in the form of $\widehat{\eta} = Mx^r$ where M is an arbitrary constant [47]. The resulting characteristic equation can be solved to give two roots

$$r_{1,2} = \frac{-c-1 \pm \sqrt{(c+1)^2 - 4\sigma^2/(c_1g)}}{2}. \tag{2.62}$$

The sign of the square-root term in Eq. (2.62) determines the behavior of the solutions [47]. Possible families of solutions can be

i) If $(c+1)^2 > 4\sigma^2/(c_1 g)$, then the roots of the characteristic equation $r_{1,2}$ are real. The solution becomes $\widehat{\eta} = Mx^{r_1} + Nx^{r_2}$ where M and N are arbitrary constants [47].

ii) If $(c+1)^2 = 4\sigma^2/(c_1 g)$, the roots of the characteristic equation $r_{1,2} = (-c-1)/2$ are repeated. The solution becomes $\widehat{\eta} = Mx^{r_1} + Nx^{r_2}\ln(x)$ [47].

iii) If $(c+1)^2 < 4\sigma^2/(c_1 g)$, the roots of the characteristic equation $r_{1,2}$ are complex. The solution becomes $\widehat{\eta} = Mx^{r_1} + Nx^{r_2}$. If we re-express the complex roots by $r_{1,2} = \lambda \pm \mu i$, then the solution can be expressed as $\widehat{\eta} = Mx^{\lambda}\cos(\mu\ln(x)) + iNx^{\lambda}\sin(\mu\ln(x))$ [47].

Due to the linearity of the governing long-wave equation, the superposition principle holds true. So any linear combinations of these expressions are also valid solutions to the problem. For the physical significance of the problem, we also require the water surface fluctuation to be finite and real. Thus, when there is no wall present in the domain, the singular point $x = 0$ causes the terms x^r for negative roots or the $\ln(x)$ to become infinite. Thus, these functions are typically eliminated from the solution. However, as per the contribution of this paper, when there is a solid vertical wall in the domain of investigation, these functions should remain as part of the solution because the singular point $x = 0$ is removed from the domain due to the presence of the wall. BC1 and BC2 must be imposed as before.

3. THE ANALYTICAL SOLUTIONS OF LONG WAVES OVER GEOMETRIES WITH LINEAR AND NONLINEAR VARIATIONS IN THE FORM OF POWER-LAW NONLINEARITIES WITH SOLID INCLINED WALL[2]

To the best of our knowledge, no research has been done in the literature to look at similar geometries where a solid inclined wall is present. Motivated by this, we take into consideration such nonlinear geometries that extend for $x \in [l_1, l_2]$ and have a solid inclined wall that is located at $x = l_1$. For such geometries, the singular point is removed from the domain with such a solid inclined wall encompassing the coordinate system's origin, and Bessel functions of the second kind start to show up in the solution. Figs. 3.1, 3.3, 3.5, 3.7, 3.9, and 3.11 below illustrate this geometry schematically. A landslide situation, a harbor with an inclined wall built before or after it began operations, and a wave energy converter like Wave Dragon with an inclined wall and similar structures may all be modeled using this kind of geometry as in Chapter 2.

Based on linear wave theory, the following boundary condition (BC1) may be provided for such a geometry in order to produce partial reflection from an inclined wall $x = l_1$ for all t

$$\frac{\partial \eta(x,t)}{\partial x} + C_w k \eta(x,t) = 0 \tag{3.1}$$

where $C_w = C_r + iC_i$. Here, C_w is a complex parameter associated with the degree of wave reflection. To find the expressions of C_w, the $\eta(x,t)$ can be expressed as

$$\eta(x,t) = Ae^{-i[k(x-l_1)+\omega t]} + A|R|e^{i[k(x-l_1)-\omega t-\delta]} \tag{3.2}$$

where A: is the incident wave amplitude, ω: angular frequency, $|R|$: wave reflection coefficient, and δ: reflected wave phase lag. After substituting Eq. (3.2) into BC1, we can obtain Eq. (3.3) as follows

[2]This chapter is based on the paper "Alan A. R., Bayındır, C. (2024). The Analytical Solutions of Long Waves Over Geometries with Linear and Nonlinear Variations in the Form of Power-Law Nonlinearities with Solid Inclined Wall, *Dynamics of Atmospheres and Oceans,* 106, 101458.".

$$-Aike^{-i\omega t} + Aik|R|e^{-i(\omega t-\delta)} + C_w k[Ae^{-i\omega t} + A|R|e^{-i(\omega t-\delta)}] = 0 \tag{3.3}$$

which yields

$$C_w = \frac{i(1-|R|e^{i\delta})}{1+|R|e^{i\delta}} \tag{3.4}$$

so that

$$C_w = \frac{2\sin\delta|R| + i(1-|R|^2)}{1+2|R|\cos\delta+|R|^2}. \tag{3.5}$$

Since $C_w = C_r + iC_i$, we can define C_r and C_i as follows

$$C_r = \frac{2\sin\delta|R|}{1+2|R|\cos\delta+|R|^2}. \tag{3.6}$$

$$C_i = \frac{1-|R|^2}{1+2|R|\cos\delta+|R|^2}. \tag{3.7}$$

To obtain horizontal velocity u corresponding to Eq. (3.2), linear long wave theory can be used to give

$$u = \sqrt{\frac{g}{h}}Ae^{-i[k(x-l_1)+\omega t]} - \sqrt{\frac{g}{h}}A|R|e^{i[k(x-l_1)-\omega t-\delta]}. \tag{3.8}$$

If we apply the (BC1) to Eq. (3.8), we get

$$u|_{x=l_1} = \sqrt{\frac{g}{h}}Ae^{-i\omega t}(1-|R|e^{i\delta}). \tag{3.9}$$

No flux boundary condition at $x = l_1$ requires that $u = 0$ at $x = l_1$. This gives $|R|e^{i\delta} = 1$, which is the case of perfect reflection $|R| = 1$ with no phase lag $\delta = 0$. Since these $|R|$ and δ values make $C_r = 0$ and $C_i = 0$, the resulting complex coefficient becomes $C_w = 0$. This case reduced to the perfect vertical wall which is analyzed in Chapter 2.

Sommerfeld radiation boundary condition at $x = l_1$ requires $\frac{\partial\eta(x,t)}{\partial x} + ik\eta(x,t) = 0$, where a wave coming from the open ocean and moving in the $-x$ direction is considered. Since $C_w = i$ for this case, thus one gets

$$\frac{1-|R|e^{i\delta}}{1+|R|e^{i\delta}} = 1 \tag{3.10}$$

which yields

$$|R|e^{i\delta} = 0 \tag{3.11}$$

so that $|R| = 0$ for any δ. Thus $C_r = 0$ and $C_i = 1$ which means that there is no reflected waves from the radiation boundary (outgoing waves only).

For partial reflection, $0 < |R| < 1$ and $\delta \neq 0$, we need empirical formulas to estimate $|R|$ and δ for given incident waves characterized by incident wave amplitude, angular frequency, depth and slope characteristics. Many formulas for $|R|$ are available but majority of them are not very accurate. Only a few formulas are available for the phase lag, δ. Furthermore, (BC1) is limited to normally incident waves on a long slope (1D problem only). In short, (BC1) avoids nonlinear waves (normally breaking waves) on the slope by employing the empirical parameter C_w ($|R|$ and δ), but introduces the uncertainty associated with $|R|$ and δ.

As a crucial metric for defining the wall boundary condition and breaker type classification on a sloping bottom or structure, the surf similarity parameter, also known as the Iribarren number (ξ), has long been acknowledged [49]. In Eq. (3.12), where β is the slope angle, H_0 is the incident deep water wave height, and L_0 is the wavelength in deep water, Iribarren first identified the combination of structural slope and wave steepness [50], and the definition of the surf similarity ξ_0 is given as [51]

$$\xi_0 = \frac{\tan\beta}{\sqrt{H_0/L_0}}. \tag{3.12}$$

Battjes [52] and Bruun [53] verified the physical interpretation of the surf similarity parameter. The use of ξ_0 has been expanded to include equations that explain wave-breaking processes such energy dissipation, wave reflection, and wave run-up/run-down [51].

The way a structure dissipates wave energy is, in fact, directly and substantially associated with the kind of wave breaker [51]. In this regard, Iversen [54] created the first categorization of breaker types as:

- **Spilling breakers** ($\xi_0 < 0.47$) Most of them form on gently sloping regions [51,54]. Foam spills down the wave's face as a result of the crest becoming unstable and spreading over a wide area, dissipating energy [51,54]. When compared to other types of breakers, the reflection is noticeably lower [51,54].

- **Plunging breakers** ($0.47 < \xi_0 < 3.30$) When a wave coils forward and breaks into the wave trough, it creates plunging breakers [51,54]. The majority of the wave energy is discharged all at once in a really strong collision [51,54]. This means that the majority of the energy dissipates across a relatively small area [51,54].

- **Surging breakers** ($3.30 < \xi_0$) They are often reflected and occur on extremely steep slopes [51,54]. A small or nonexistent surf zone is another feature that distinguishes them [51,54].

Galvin [55] created a different form of breaker termed collapsing breakers as a transition between plunging and surging breakers ($2.5 < \xi_0 < 3.3$) [51]. The collapsing breaker type, however, should not be taken into consideration according to Dean and Dalrymple [5] and other writers (e.g., [56,57]) as it is the outcome of the combination of other breaker types (plunging and surging breakers) [51]. As the collapsing breaker represents the transition between plunging and surging breakers, guidelines like [58,59] take it into consideration [51]. For this reason, it's crucial to characterize the ξ_0-limits where this change takes place [51].

The hydrodynamics close to a structure may be analyzed and simulated, or wave transformation can be computed, by determining the processes involved in wave breaking, the kind of breaker, and the breaking start [51,60]. This has led to several investigations on the beginning of breaking waves and how to characterize it using a breaker depth index [51]. The function of the wave breaker height (H_b) and the depth at which the wave breaking begins (h_b) characterizes the latter [51]. Consequently, four functional variants of the breaker index equations may be distinguished [51,61] as:

$$H_b/h_b = f_1(0) = \text{ constant }. \tag{3.13}$$

$$H_b/h_b = f_2(h_b/L_0 \text{ or } h_b/L_b). \tag{3.14}$$

$$H_b/h_b = f_3(m). \tag{3.15}$$

$$H_b/h_b = f_4(m\ , h_b/L_0 \text{ or } h_b/L_b). \tag{3.16}$$

where the deep water wavelength is L_0, the bed slope is $m = \tan\beta$. Here, the breaking point is indicated by the subscript b [51].

For solitary waves, McCowan's formula [62] is a classic example of the first kind; it assumes a constant value of 0.78. Further, Yamada's research [63] yields a value of 0.826 [51]. The wavelength and water depth were regarded by Miche [64] and Battjes [65] as the primary criteria for the breaker index; however, the impact of the slope steepness $\tan\beta$ on the breaking process was overlooked [51]. The third functional version was used in the research by Collins et al. [66], Galvin [67], and Kishi and Saeki [68] with the slope steepness incorporated into the breaker index [51]. Rattanapitikon and Vivattanasirisak [69] compare many breaker index formulae and find that the four functional version of the breaking index has the greatest prediction performance [51]. Ostendorf and Madsen [70], Larson and Kraus [71], Gourlay [72], Goda [73] modified by Rattanapitikon and Shibayama [74], and Kamphuis [75] for irregular waves are some ways based on this functional form [51].

Wave energy is reflected by the structure and released in part via the wave breaking process [51]. The hydrodynamic performance of revetments may thus be described by considering wave reflection, which influences the wave-wave interaction [51]. The reflection is measured for this purpose using a reflection coefficient ($|R|$), which is defined as the ratio of the reflected (H_r) to the incident wave height (H_i), or the square root of the ratio of the reflected (E_r) to the incident energy (E_i) as follows [51]:

$$|R| = \frac{H_r}{H_i} = \sqrt{\frac{E_r}{E_i}}. \tag{3.17}$$

The value of $|R|$ has been determined by laboratory research, which are often expressed as a function of the surf similarity parameter ξ_0 [51]. An equation for the reflection coefficient $|R|$ in terms of the wave steepness was originally attempted by Miche [76]. A reinterpretation of Miche's method was given by Battjes [52], who included the surf similarity parameter as a crucial parameter for the wave reflection Eq. (3.18) [51].

$$|R| = 0.1\xi_0^2. \tag{3.18}$$

In addition to taking into account various coastal constructions, such as smooth impermeable slopes, multi-layered rubble mound breakwaters, Seelig and Ahrens [77] presented a technique based on laboratory testing for regular and irregular waves [51]. As a consequence, Eq. (3.19) was created, in which coefficient B is entirely empirical and coefficient A takes into consideration the position of the wave breaking start as well as fluctuations in the slope surface (via d_{eq}= equivalent grain diameter) [51].

$$|R| = \min\left[\frac{A\xi_0^2}{\xi_0^2 + B}\right] \; with\, A = \exp\left[-1.7\sqrt{\frac{d_{eq}}{L_0}}\cot\beta - 0.5\left(\frac{H_i}{H_b}\right)^{1.2}\right]. \tag{3.19}$$

For smooth, impermeable walls, Seelig and Ahrens [77] propose $A = 1$ and $B = 5.5$, but for rubble mound breakwaters, they prefer $A = 0.6$ and $B = 6.6$ [51]. For idealized smooth, impermeable structures, the reflection coefficient is set to 1 because A gives the limiting value of the reflection coefficient for large Iribarren numbers [51].

For rough permeable slopes, Losada and Giménez-Curto [78] proposed an exponential model (Eq. (3.20)) in terms of the surf similarity parameter [51]. For this reason, the coefficients A_U and B_U for rip-rap revetments, dolos, rubble mound breakwaters, and quadripods have been defined in Tab. 3.1 [51].

$$|R| = A_U\left[1 - \exp\left(B_U \xi\right)\right]. \tag{3.20}$$

Table 3.1 : The values of A_U and B_U coefficients for estimating $|R|$ with Eq. (3.20) [51,78].

Type of armor units	A_U	B_U
Rip-rap	1.451-1.7887	-0.4552
Rubble	1.3698	-0.5964
Dolos	1.2158	-0.5675
Quadripods	1.5382	-0.2483

Postma [79] conducted more research on irregular waves over rubble mound breakwaters, and found that the permeability had an influence (Eq. (3.21)), when taken into account through the notional permeability P [51,80]. Moreover, it was shown that the wave period had a greater impact on the reflection behavior than the wave height [51].

$$|R| = 0.071 P^{-0.082} \cot^{-0.62}\beta \left(\frac{H_s}{L_{op}}\right)^{-0.46} \tag{3.21}$$

with the deep water wave length associated with peak period T_p being $L_{op} = gT_p^2/(2\pi)$.

Davidson et al. [81] conducted measurements of wave reflection across a rock island barrier. Eq. (3.22), which is expressed in terms of a reflection number r and takes into account the local water depth at the structure's toe (h_{toe}), the slope angle, the wave length in deep water, and the diameter of the rock armor units, was produced by comparing the results of these measurements with those of earlier methods [51].

$$|R| = 0.151 r^{0.11} \text{ with } r = \frac{h_{toe} L_0^2 \tan\beta}{H_i d_{eq}}. \tag{3.22}$$

Davidson et al. [81] identified the critical factors influencing the reflection process and came to the following conclusions:

- i) the wave length L_0 is one of the most significant variables, as an increase in L_0 increases the reflection coefficient until a ξ_0-value at which $|R|$ becomes constant [51,81];

- ii) the local water depth and wave height at the structure's toe, h_{toe}, have a slight impact on $|R|$ [51,81];

- iii) the slope angle plays a significant role in a wide range of the reflection coefficient [51,81].

The reflection behavior of a variety of structures, including berm breakwaters, vertical structures, slopes with manufactured armor units, and permeable rock slopes with impermeable slopes, was examined by [51,82]. Additionally, a vast and uniform database was produced by analyzing pre-existing equations [51,52,77,78]. After analyzing the database, it was determined that Seelig and Ahrens [77] adequately fits the data for smooth slopes; however, limitations were discovered when attempting to predict the reflection behavior of other armor units, impermeable slopes, and slopes covered in rock material [51,77]. Eq. (3.23) was therefore created to offer a special expression for all kinds of structures [51]. To achieve this, the reflection coefficient is described by Eq. (3.23) using the surf similarity parameter ξ_0 and two coefficients, A and B, which may be written as functions of the slope roughness [51].

$$|R| = \tanh A\xi_0^B. \tag{3.23}$$

By representing the physical bounds (for $\xi_0 \to 0$, $|R| = 0$, and for $\xi_0 \to \infty$, $|R| = 1$), in addition to applying Zanuttigh's formula for a number of structure variations, the approach is extensible to other structure variations, such as porous bonded revetments, because the coefficients are related to the slope roughness [51].

Hughes and Fowler's [83] paper is the first to attempt characterizing the phase-shift spectrum and the reflection coefficient spectrum for irregular waves [84]. They employed a collocated velocities approach to compute reflection coefficient spectra and recorded irregular waves in front of smooth, impermeable walls, and a rubble mound breakwater [84]. Three toe depths and three peak frequencies were employed, with each toe depth having a little different significant wave height in [84]. Plotting the reflection coefficients versus a non-dimensional parameter, δ in this case, which is specified as [84],

$$\delta = \frac{f_n}{\tan\beta}\sqrt{\frac{d_t}{g}} = \frac{x_m}{L_s} \tag{3.24}$$

where the following are given: $x_m = d_t/\tan\beta$ is identified as the cross-shore length of the structure from the toe to still water level; f_n is identified as the frequency of the nth component; d_t is identified as the water depth at the structure's toe; and $L_s = \sqrt{gd_t/f_n}$ is identified as the linear theory shallow water wavelength [84]. For both the rubble mound breakwater and the impermeable walls, empirical correlations for the phase spectra and reflection coefficient were discovered in [84].

Hughes and Fowler [83] and Sutherland and O'Donoghue [85] employed the parameter δ_s to calculate the wave phase shift spectrum on reflection [84]. Because the phase shift is almost independent of the wave height, that's why this works good [84]. It is unclear that δ_s can characterize the reflection coefficient spectrum across a large range of incidence wave heights, though, because the reflection coefficient is predicted to change on wave height [84].

The format of the reflection coefficient spectrum for random wave reflection from coastal properties has been attempted to be characterized by a variety of wave reflection tests [84]. Tests were conducted on breakwaters with rubble mounds and smooth, impervious walls [84]. The effects of toe depth and significant wave height are not sufficiently taken into account by the parameter that Hughes and Fowler [83] offered for describing the reflection coefficient spectrum δ which is given by Eq. (3.24) [84]. Nonetheless, at frequencies where the spectra overlap and where there is a significant amount of energy, seas with different peak frequencies but the same incident significant wave height reflecting off a given structure have similar reflection coefficients [84].

It is possible to relate the inclined wall slope angle, β, with the reflection coefficient $|R|$ and phase lag δ using aforementioned formulas, thus C_w can be determined. Especially Eq. (3.20) and Eq. (3.24) would be useful in this regard. It is also possible to relate C_w with the wave breaking, however in this paper we only consider non-breaking waves.

The open ocean boundary condition (BC2) $x = l_2$ may be expressed as

$$\eta(x,t) = \frac{H}{2}\cos(\sigma t) \tag{3.25}$$

considering a forcing by a harmonic wave with waveheight H. The boundary value problem (BVP) analysis is summarized by these boundary conditions and the long wave equation.

The long wave equation for arbitrary nonlinear geometry may be redefined as follows if $\sigma^2/c_1 g = k^2 > 0$ and $Z_{|\nu|}$ are taken to be $J_{|\nu|}$ and $Y_{|\nu|}$

$$\widehat{\eta}(x) = Ax^{\nu/\alpha} J_{|\nu|}\left(\alpha k x^{1/\alpha}\right) + Bx^{\nu/\alpha} Y_{|\nu|}\left(\alpha k x^{1/\alpha}\right). \tag{3.26}$$

Utilizing the Bessel functions' well-known derivative relations

$$\frac{\partial J_\nu(z)}{\partial z} = \frac{\nu}{z} J_\nu(z) - J_{\nu+1}(z) \tag{3.27}$$

and

$$\frac{\partial Y_\nu(z)}{\partial z} = \frac{\nu}{z} Y_\nu(z) - Y_{\nu+1}(z). \tag{3.28}$$

One may calculate the derivative of $\widehat{\eta(x)}$ as

$$\begin{aligned}\frac{\partial \widehat{\eta}(x)}{\partial x} =& A\left[\frac{\nu}{\alpha} x^{\frac{\nu-\alpha}{\alpha}} J_{|\nu|}\left(\alpha k x^{1/\alpha}\right) + \frac{|\nu|}{\alpha} x^{\frac{\nu-\alpha}{\alpha}} J_{|\nu|}\left(\alpha k x^{1/\alpha}\right) - k x^{\frac{\nu+1-\alpha}{\alpha}} J_{|\nu|+1}\left(\alpha k x^{1/\alpha}\right)\right] \\ &+ B\left[\frac{\nu}{\alpha} x^{\frac{\nu-\alpha}{\alpha}} Y_{|\nu|}\left(\alpha k x^{1/\alpha}\right) + \frac{|\nu|}{\alpha} x^{\frac{\nu-\alpha}{\alpha}} Y_{|\nu|}\left(\alpha k x^{1/\alpha}\right) - k x^{\frac{\nu+1-\alpha}{\alpha}} Y_{|\nu|+1}\left(\alpha k x^{1/\alpha}\right)\right].\end{aligned} \tag{3.29}$$

We provide the solution of this BVP for the two following cases:

i) Case 1: When $\nu \geq 0$, so $|\nu| = \nu$. This may be solved algebraically by applying BC1 at $x = l_1$ and BC2 at $x = l_2$.

$$\begin{aligned}\eta(x,t) = \frac{H}{2{l_2}^{\nu/\alpha}} \Bigg[&\frac{-\Theta_2}{\Theta_1 Y_\nu\left(\alpha k {l_2}^{1/\alpha}\right) - \Theta_2 J_\nu\left(\alpha k {l_2}^{1/\alpha}\right)} x^{\nu/\alpha} J_\nu\left(\alpha k x^{1/\alpha}\right) \\ &+ \frac{\Theta_1}{\Theta_1 Y_\nu\left(\alpha k {l_2}^{1/\alpha}\right) - \Theta_2 J_\nu\left(\alpha k {l_2}^{1/\alpha}\right)} x^{\nu/\alpha} Y_\nu\left(\alpha k x^{1/\alpha}\right)\Bigg] \cos(\sigma t).\end{aligned} \tag{3.30}$$

Here, the parameter Θ_1 is $\Theta_1 = \left(\frac{2\nu}{\alpha} + C_w k l_1\right) J_\nu\left(\alpha k {l_1}^{1/\alpha}\right) - k{l_1}^{1/\alpha} J_{\nu+1}\left(\alpha k {l_1}^{1/\alpha}\right)$ and Θ_2 is $\Theta_2 = \left(\frac{2\nu}{\alpha} + C_w k l_1\right) Y_\nu\left(\alpha k {l_1}^{1/\alpha}\right) - k{l_1}^{1/\alpha} Y_{\nu+1}\left(\alpha k {l_1}^{1/\alpha}\right)$.

The $\eta(x,t)$ value we obtained for the inclined wall, which we expressed with Eq. (3.30), is symbolically the same as the $\eta(x,t)$ value we obtained for the vertical wall, which we expressed with Eq. (2.5) in Chapter 2. However, when the Θ_1 and Θ_2 parameters here are compared with the parameters in Chapter 2, it is observed that there are extra $C_w k l_1$ terms in the coefficients of the $J_\nu\left(\alpha k {l_1}^{1/\alpha}\right)$ and $Y_\nu\left(\alpha k {l_1}^{1/\alpha}\right)$ functions due to the inclined wall.

ii) Case 2: If $\nu < 0$ in which case $|\nu| = -\nu$, a solution to this BVP may be obtained algebraically applying BC1 at $x = l_1$ and BC2 at $x = l_2$

$$\eta(x,t) = \frac{H}{2{l_2}^{\nu/\alpha}} \left[\frac{-\Gamma_2}{\Gamma_1 Y_{-\nu}\left(\alpha k {l_2}^{1/\alpha}\right) - \Gamma_2 J_{-\nu}\left(\alpha k {l_2}^{1/\alpha}\right)} x^{\nu/\alpha} J_{-\nu}\left(\alpha k x^{1/\alpha}\right) \right.$$
$$\left. + \frac{\Gamma_1}{\Gamma_1 Y_{-\nu}\left(\alpha k {l_2}^{1/\alpha}\right) - \Gamma_2 J_{-\nu}\left(\alpha k {l_2}^{1/\alpha}\right)} x^{\nu/\alpha} Y_{-\nu}\left(\alpha k x^{1/\alpha}\right) \right] \cos(\sigma t). \tag{3.31}$$

Here, the parameter Γ_1 is $\Gamma_1 = -{l_1}^{\frac{1-\alpha}{\alpha}} J_{1-\nu}\left(\alpha k {l_1}^{1/\alpha}\right) + C_w l_1 J_{-\nu}\left(\alpha k {l_1}^{1/\alpha}\right)$ and Γ_2 is $\Gamma_2 = -{l_1}^{\frac{1-\alpha}{\alpha}} Y_{1-\nu}\left(\alpha k {l_1}^{1/\alpha}\right) + C_w l_1 Y_{-\nu}\left(\alpha k {l_1}^{1/\alpha}\right)$.

Although we cannot make a direct interpretation of the $\eta(x,t)$ value we obtained for the inclined wall, which we expressed with Eq. (3.31), and the $\eta(x,t)$ value we obtained for the vertical wall, which we expressed with Eq. (2.6) in Chapter 2, since they are slightly different in representation, we can say that there are extra $C_w l_1$ terms in Eq. (3.31) due to the inclined wall by looking at the Γ_1 and Γ_2 parameters in it.

In the next section we examine six distinct numerical examples of these solutions for a range of nonlinear geometries including a solid inclined wall.

3.1 Linear Breadth Variation ($b(x) = c_2 x^c$ with $c = 1$) with a Solid Inclined Wall

The case of linear breadth variation with a solid inclined wall extending from $x = 0$ to $x = l_1$ which is illustrated in Fig. 3.1 is analyzed in this section.

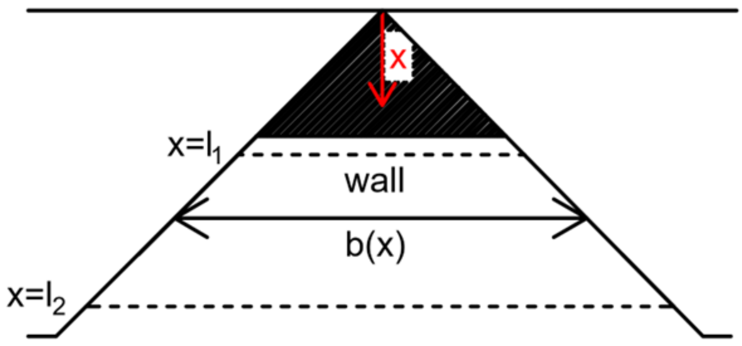

Figure 3.1 : Linear breadth variation with an inclined wall.

Here, depth is a constant ($a = 0$) that falls inside the limits defined by the long wave theory and $c = 1$. Equations $\alpha = \frac{2}{2-a} = 1$ and $\nu = \frac{1-a-c}{2-a} = 0$ may be used to get the parameters of the Bessel-Z equation provided in Eq. (1.76). For these parameters Eq. (1.76) can be reduced to [46]

$$\frac{d^2\widehat{\eta}}{dx^2} + \frac{1}{x}\frac{d\widehat{\eta}}{dx} + k^2\widehat{\eta} = 0 \tag{3.32}$$

where $k^2 = \sigma^2/c_1 g$. With these values, the long wave equation can be solved to give

$$\eta(x,t) = [AJ_0(kx) + BY_0(kx)]\cos(\sigma t) \tag{3.33}$$

where $J_0(kx)$ and $Y_0(kx)$ are the Bessel functions' first and second kind forms with order 0, respectively. For the illustrations of the Bessel functions of the first kind and the second kind with the first three orders please kindly check Fig. 2.2 and Fig. 2.3 in Chapter 2.

BCs must be applied to be able to determine the coefficients A and B. The solid inclined wall BC is the first BC considered (BC1). In the case of an inclined wall at $x = l_1$, BC1 can be defined as $\frac{\partial \eta}{\partial x} + C_w k\eta = 0$ for every t at $x = l_1$. When the derivative of Eq. (3.33) is taken with respect to x, Eq. (3.34) can be obtained as

$$\frac{\partial \widehat{\eta}(x)}{\partial x} = [-AkJ_1(kx) - BkY_1(kx)] \tag{3.34}$$

where the relations of $\frac{\partial J_0(kx)}{\partial x} = -kJ_1(kx)$ and $\frac{\partial Y_0(kx)}{\partial x} = -kY_1(kx)$ are used. Imposing BC1 using Eq. (3.35) gives

$$\begin{aligned}\left.\frac{\partial\eta(x,t)}{\partial x}+C_wk\eta(x,t)\right|_{x=l_1}&=0\\&=[-AkJ_1(kl_1)-BkY_1(kl_1)]\cos(\sigma t)\\&\quad+C_wk[AJ_0(kl_1)+BY_0(kl_1)]\cos(\sigma t).\end{aligned}\tag{3.35}$$

This equation can be rearranged to give

$$-A[-J_1(kl_1)+C_wJ_0(kl_1)]=B[-Y_1(kl_1)+C_wY_0(kl_1)]\tag{3.36}$$

and

$$A=\frac{-B[-Y_1(kl_1)+C_wY_0(kl_1)]}{[-J_1(kl_1)+C_wJ_0(kl_1)]}.\tag{3.37}$$

At $x=l_2$, the open ocean BC (BC2) may be expressed as

$$\eta(x,t)=\frac{H}{2}\cos(\sigma t).\tag{3.38}$$

Here, H indicates the wave height of the wave entering from the ocean. Throughout this paper the value of $H=1\ m$ is assumed and only non-breaking waves are considered. Imposing BC2 on Eq. (3.33) yields

$$\eta(l_2,t)=[AJ_0(kl_2)+BY_0(kl_2)]\cos(\sigma t)=\frac{H}{2}\cos(\sigma t).\tag{3.39}$$

Once the $\cos(\sigma t)$ terms are cancelled, Eq. (3.40) is obtained as

$$AJ_0(kl_2)+BY_0(kl_2)=\frac{H}{2}.\tag{3.40}$$

When the value of A in Eq. (3.37) is substituted, Eq. (3.41) is obtained as

$$\frac{-B[-Y_1(kl_1)+C_wY_0(kl_1)]}{[-J_1(kl_1)+C_wJ_0(kl_1)]}J_0(kl_2)+BY_0(kl_2)=\frac{H}{2}.\tag{3.41}$$

Following eliminations, one might acquire

$$B=\frac{H[J_1(kl_1)-C_wJ_0(kl_1)]}{2\{[J_1(kl_1)-C_wJ_0(kl_1)]Y_0(kl_2)-[Y_1(kl_1)-C_wY_0(kl_1)]J_0(kl_2)\}}.\tag{3.42}$$

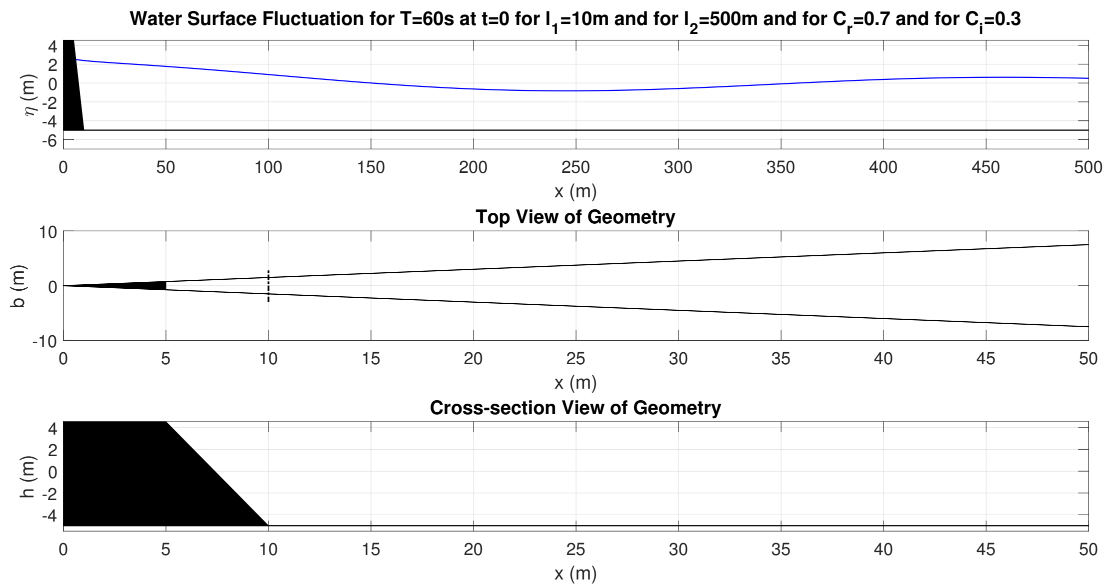

Figure 3.2 : Water surface fluctuation (η) for constant depth $h(x) = -5$ and linear breadth profile of $b(x) = 0.3x$ with $C_r = 0.7$, and $C_i = 0.3$ with a solid inclined wall.

When the B value which is found in Eq. (3.42) is substituted into Eq. (3.37), A is obtained as

$$A = -\frac{H[Y_1(kl_1) - C_w Y_0(kl_1)]}{2\{[J_1(kl_1) - C_w J_0(kl_1)]Y_0(kl_2) - [Y_1(kl_1) - C_w Y_0(kl_1)]J_0(kl_2)\}}. \tag{3.43}$$

After the coefficients from Eq. (3.42) and Eq. (3.43) are reinserted into Eq. (3.33), the long wave solution for the geometry under consideration is obtained as

$$\eta(x,t) = \frac{H}{2}\left\{\frac{[J_1(kl_1) - C_w J_0(kl_1)]Y_0(kx) - [Y_1(kl_1) - C_w Y_0(kl_1)]J_0(kx)}{[J_1(kl_1) - C_w J_0(kl_1)]Y_0(kl_2) - [Y_1(kl_1) - C_w Y_0(kl_1)]J_0(kl_2)}\right\}\cos(\sigma t). \tag{3.44}$$

For the values of $\alpha = 1, \nu = 0$ the Eq. (3.30) results in the same outcome. For $T = 60\,s$, $c_1 = 5\,m$, $c_2 = 0.3$, $a = 0$, $c = 1$, $l_1 = 10\,m$, $l_2 = 500\,m$, $C_r = 0.7$, and $C_i = 0.3$ values at time $t = 0\,s$, the water surface fluctuation, η, of the long wave for the studied geometry is illustrated in Fig. 3.2. Throughout this paper, the water surface fluctuation (blue line) as well as the breath and depth variations (black lines) are depicted.

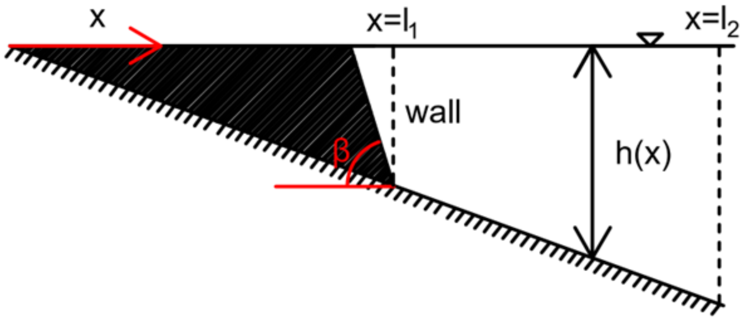

Figure 3.3 : Linear depth variation with an inclined wall (cross-section view).

By numerically calculating the zeros of the Bessel functions, the zeros and maximum points of η may also be found, which would be useful in evaluating the resonance point and properties.

If we compare this $\eta(x,t)$ value we obtained for the inclined wall, which we expressed with Eq. (3.44), with the $\eta(x,t)$ value we obtained for the vertical wall, which we expressed with Eq. (2.19) in Chapter 2, we notice that there is an extra $-C_w Y_0(kl_1)$ expression in the multipliers of the expressions with J_0 in both the numerator and denominator. Likewise, we notice that there is an extra $-C_w J_0(kl_1)$ expression in the multipliers of expressions with Y_0 in both the numerator and denominator. We can make a graphical interpretation of this difference by comparing Fig. 3.2 and Fig. 2.4. When we examine these figures, we observe that in Fig. 3.2, that is, in the case of the inclined wall, there is approximately 1 m more wave height than the vertical wall.

3.2 Linear Depth Variation ($h(x) = c_1 x^a$ with $a = 1$) with a Solid Inclined Wall

To further our study, we take into account a linear change in depth, where the breadth is unbounded, and takes the form of $h(x) = c_1 x^a$ for $a = 1$. The layout of the solid inclined wall is illustrated in Fig. 3.3, which illustrates this type of geometry. In this scenario, the parameters of the Bessel-Z equation, as stated in Eq. (1.76), may be calculated as $\alpha = \frac{2}{2-a} = 2$ and $\nu = \frac{1-a-c}{2-a} = 0$.

It is widely known that the governing long wave equation admits solution in terms of Bessel functions for such a linear depth variation [5,46]. This solution may be expressed as

$$\eta(x,t) = [AJ_0(2k\sqrt{x}) + BY_0(2k\sqrt{x})]\cos(\sigma t) \tag{3.45}$$

where $k^2 = \sigma^2/c_1 g$. The wall boundary condition (BC1) remains the same for all t for fixed solid inclined wall: $\frac{\partial\eta}{\partial x} = 0$ at $x = l_1$. By taking the partial derivative of Eq. (3.45) with respect to x, we may impose BC1 by getting

$$\frac{\partial\eta(x,t)}{\partial x} = [-Akx^{-1/2}J_1(2k\sqrt{x}) - Bkx^{-1/2}Y_1(2k\sqrt{x})]\cos(\sigma t) \tag{3.46}$$

where the relations $\frac{\partial J_0(z)}{\partial z} = -J_1(z)$ and $\frac{\partial Y_0(z)}{\partial z} = -Y_1(z)$ were utilized. If BC1 is imposed, one can get

$$\begin{aligned}\left.\frac{\partial\eta(x,t)}{\partial x} + C_w k\eta(x,t)\right|_{x=l_1} &= 0 \\ &= [-Akl_1{}^{-1/2}J_1(2k\sqrt{l_1}) - Bkl_1{}^{-1/2}Y_1(2k\sqrt{l_1})]\cos(\sigma t) \\ &\quad + C_w k[AJ_0(2k\sqrt{x}) + BY_0(2k\sqrt{x})]\cos(\sigma t)\end{aligned} \tag{3.47}$$

that results in

$$A = \frac{-B\left[Y_1(2k\sqrt{l_1}) - C_w Y_0(2k\sqrt{l_1})\sqrt{l_1}\right]}{\left[J_1(2k\sqrt{l_1}) - C_w J_0(2k\sqrt{l_1})\sqrt{l_1}\right]}. \tag{3.48}$$

The open ocean boundary condition (BC2) is utilized to solve for the coefficients A and B. As before BC2 is

$$\eta(x,t)|_{x=l_2} = \frac{H}{2}\cos(\sigma t). \tag{3.49}$$

Imposing BC2 to Eq. (3.45) one can get

$$\eta(l_2,t) = \left[AJ_0(2k\sqrt{l_2}) + BY_0(2k\sqrt{l_2})\right]\cos(\sigma t) = \frac{H}{2}\cos(\sigma t). \tag{3.50}$$

After the $\cos(\sigma t)$ terms are canceled and after some algebra involving Eq. (3.48) and Eq. (3.50), one might acquire

$$B = \frac{H\left[J_1(2k\sqrt{l_1}) - C_w J_0(2k\sqrt{l_1})\sqrt{l_1}\right]}{2\Sigma} \tag{3.51}$$

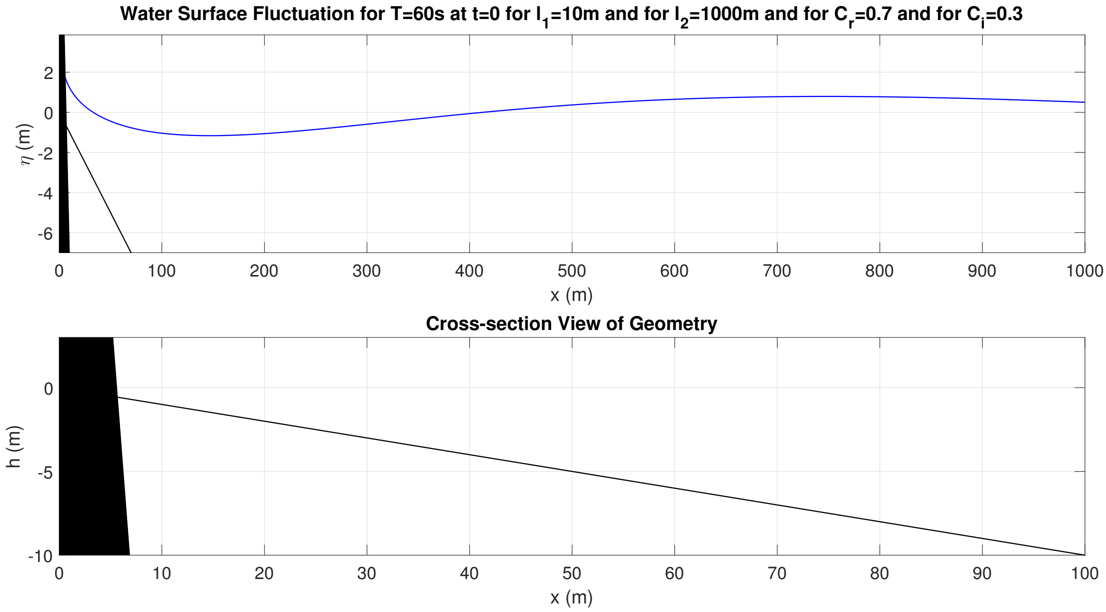

Figure 3.4 : Water surface fluctuation (η) for unbounded breadth and linear depth profile of $h(x) = 0.1x$ with $C_r = 0.7$, and $C_i = 0.3$ with a solid inclined wall.

where $\Sigma = \left[J_1(2k\sqrt{l_1}) - C_w J_0(2k\sqrt{l_1})\sqrt{l_1}\right] Y_0(2k\sqrt{l_2})$
$- \left[Y_1(2k\sqrt{l_1}) - C_w Y_0(2k\sqrt{l_1})\sqrt{l_1}\right] J_0(2k\sqrt{l_2})$.

When we replace the B parameter in Eq. (3.48), A is obtained as

$$A = -\frac{H\left[Y_1(2k\sqrt{l_1}) - C_w Y_0(2k\sqrt{l_1})\sqrt{l_1}\right]}{2\Sigma}. \tag{3.52}$$

Calculation of the water surface fluctuation may be performed by substituting the computed A and B parameters back into Eq. (2.20) as it follows

$$\eta(x,t) = \frac{H}{2}\left(\frac{[-Y_1(2k\sqrt{l_1}) + C_w Y_0(2k\sqrt{l_1})\sqrt{l_1}]J_0(2k\sqrt{x})}{\Sigma}\right.$$
$$\left. + \frac{[J_1(2k\sqrt{l_1}) - C_w J_0(2k\sqrt{l_1})\sqrt{l_1}]Y_0(2k\sqrt{x})}{\Sigma}\right)\cos(\sigma t). \tag{3.53}$$

For the case specific values of $\alpha = 2, \nu = 0$ the Eq. (3.30) leads to the same result.

For $T = 60\ s$, $c_1 = 0.1$, $a = 1$, $c = 0$, $l_1 = 10\ m$, $l_2 = 1000\ m$, $C_r = 0.7$, and $C_i = 0.3$ values at time $t = 0\ s$, the water surface fluctuation, η, of the long wave for the studied linear depth varying geometry is illustrated in Fig. 3.4. There is no dependence of the solution on c_2. As previously, the η may be used to determine its antinodes and nodes by utilizing a numerical approach to calculate the zeros of Bessel functions.

If we compare this $\eta(x,t)$ value we obtained for the inclined wall, which we expressed with Eq. (3.53), with the $\eta(x,t)$ value we obtained for the vertical wall, which we expressed with Eq. (2.28) in Chapter 2, we notice that there is an extra $C_w Y_0(2k\sqrt{l_1})\sqrt{l_1}$ expression in the multipliers of the expressions with J_0 in both the numerator and denominator. Likewise, we notice that there is an extra $-C_w J_0(2k\sqrt{l_1})\sqrt{l_1}$ expression in the multipliers of expressions with Y_0 in both the numerator and denominator. We can make a graphical interpretation of this difference by comparing Fig. 3.4 and Fig. 2.6. When we examine these figures, it can be observed that although Fig. 3.4, that is, the inclined wall case, has almost the same wave height as the vertical wall case, the water surface fluctuation in the inclined wall case is higher than that in the vertical wall.

3.3 Linear Breadth and Depth Variation ($b(x) = c_2 x^c$ with $c = 1$ and $h(x) = c_1 x^a$ with $a = 1$) with a Solid Inclined Wall

Our focus then shifts to the scenario in which there is a solid inclined wall in a wedge-shaped geometry, as shown in Fig. 3.5, where the breadth and depth fluctuations are both linear. In this case, $\alpha = \frac{2}{2-a} = 2$ and $\nu = \frac{1-a-c}{2-a} = -1$ since $a = 1$ and $c = 1$. Thus, for this case Eq. (1.76) can be simplified to

$$\frac{d}{dx}\left[x^2 \frac{d\widehat{\eta}(x)}{dx}\right] + \frac{\sigma^2}{c_1 g} x\widehat{\eta} = 0 \tag{3.54}$$

and the corresponding solution in Eq. (1.77) reduces to

$$\widehat{\eta}(x) = x^{-1/2} Z_1\left(2\sqrt{\left|\frac{\sigma^2}{c_1 g}\right|} x^{1/2}\right). \tag{3.55}$$

As before, letting $\sigma^2/c_1 g = k^2 > 0$ and thus taking Z_1 to be J_1 and Y_1, the solution of the long wave equation can be rewritten as

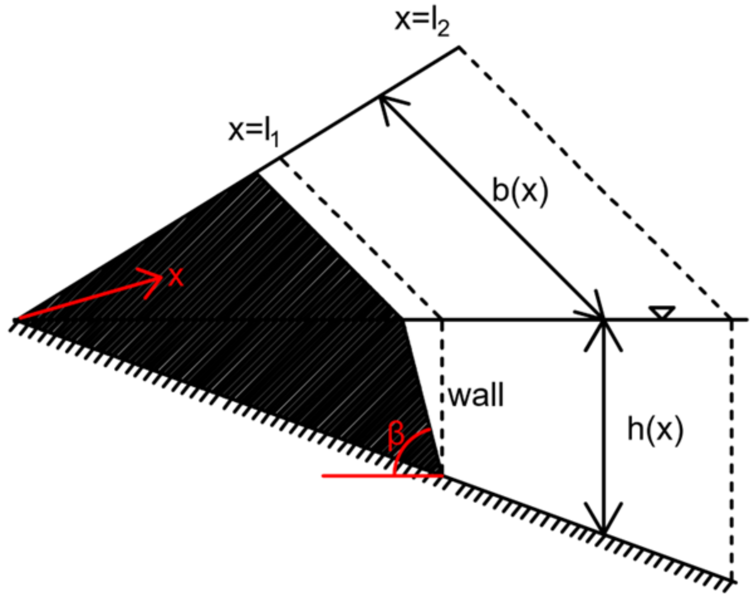

Figure 3.5 : Linear breadth and depth variation with a solid inclined wall.

$$\widehat{\eta}(x) = Ax^{-1/2}J_1(2k\sqrt{x}) + Bx^{-1/2}Y_1(2k\sqrt{x}). \tag{3.56}$$

For all t, $\frac{\partial \eta}{\partial x} + C_w k\eta = 0$ at $x = l_1$ is the solid inclined wall boundary condition (BC1). By taking the partial derivative of Eq. (3.56) with respect to x, we may impose BC1 and get

$$\frac{\partial \widehat{\eta}(x)}{\partial x} = A\left[-kx^{-1}J_2(2k\sqrt{x})\right] + B\left[-kx^{-1}Y_2(2k\sqrt{x})\right] \tag{3.57}$$

where the Bessel functions relations given by Eq. (3.27) and Eq. (3.28) are employed in the derivative relations. If BC1 is imposed one gets

$$A = \frac{-B\left[Y_2(2k\sqrt{l_1}) + Y_1(2k\sqrt{l_1})C_w\sqrt{l_1}\right]}{\left[J_2(2k\sqrt{l_1}) + J_1(2k\sqrt{l_1})C_w\sqrt{l_1}\right]}. \tag{3.58}$$

As previously, the boundary condition for the open ocean is BC2. When BC2 is applied, it is possible to obtain

$$\eta|_{x=l_2} = \frac{H}{2}\cos(\sigma t) = \left[Al_2^{-1/2}J_1(2k\sqrt{l_2}) + Bl_2^{-1/2}Y_1(2k\sqrt{l_2})\right]\cos(\sigma t). \tag{3.59}$$

Following simplifications, one can derive

$$\frac{H}{2} = \left[A{l_2}^{-1/2} J_1(2k\sqrt{l_2}) + B{l_2}^{-1/2} Y_1(2k\sqrt{l_2}) \right]. \tag{3.60}$$

Together with this equation, one can simultaneously use Eq. (3.58) to get

$$B = \frac{H}{2{l_2}^{-1/2}} \frac{J_2(2k\sqrt{l_1}) - J_1(2k\sqrt{l_1})C_w\sqrt{l_1}}{\Delta}. \tag{3.61}$$

Here, $\Delta = Y_1(2k\sqrt{l_2})[J_2(2k\sqrt{l_1}) - J_1(2k\sqrt{l_1})C_w\sqrt{l_1}]$
$-J_1(2k\sqrt{l_2})[Y_2(2k\sqrt{l_1}) - Y_1(2k\sqrt{l_1})C_w\sqrt{l_1}]$. When one plugs the parameter B into Eq. (3.58), A can be obtained as

$$A = -\frac{H}{2{l_2}^{-1/2}} \frac{Y_2(2k\sqrt{l_1}) - Y_1(2k\sqrt{l_1})C_w\sqrt{l_1}}{\Delta}. \tag{3.62}$$

By using the expressions obtained for A and B, the solution in Eq. (3.56) may be written as

$$\begin{aligned}\eta(x,t) = \frac{H}{2{l_2}^{-1/2}} \Bigg(& \frac{J_2(2k\sqrt{l_1}) - J_1(2k\sqrt{l_1})C_w\sqrt{l_1}}{\Delta} x^{-1/2} Y_1(2k\sqrt{x}) \\ & - \frac{Y_2(2k\sqrt{l_1}) - Y_1(2k\sqrt{l_1})C_w\sqrt{l_1}}{\Delta} x^{-1/2} J_1(2k\sqrt{x}) \Bigg) \cos(\sigma t).\end{aligned} \tag{3.63}$$

Since the parameters are $\alpha = 2, \nu = -1$ for this case, the solution given by Eq. (3.30) can be reduced to the same solution. Fig. 3.6 shows this water surface fluctuation that was produced for the linear variation in both breadth and depth. $T = 60\ s$, $c_1 = 0.15$, $c_2 = 0.3$, $a = 1$, $c = 1$, $l_1 = 10\ m$, $l_2 = 2000\ m$, $C_r = 0.7$, and $C_i = 0.3$ values at time $t = 0\ s$ are chosen as the computational parameters. As can be seen in Fig. 3.6, η is magnified by twenty times relative to its open ocean value, thus it is possible to conclude that wedge-shaped geometry has a considerable resonator effect. Such a form is an excellent choice for resonating the waves.

If we compare this $\eta(x,t)$ value we obtained for the inclined wall, which we expressed with Eq. (3.63), with the $\eta(x,t)$ value we obtained for the vertical wall,

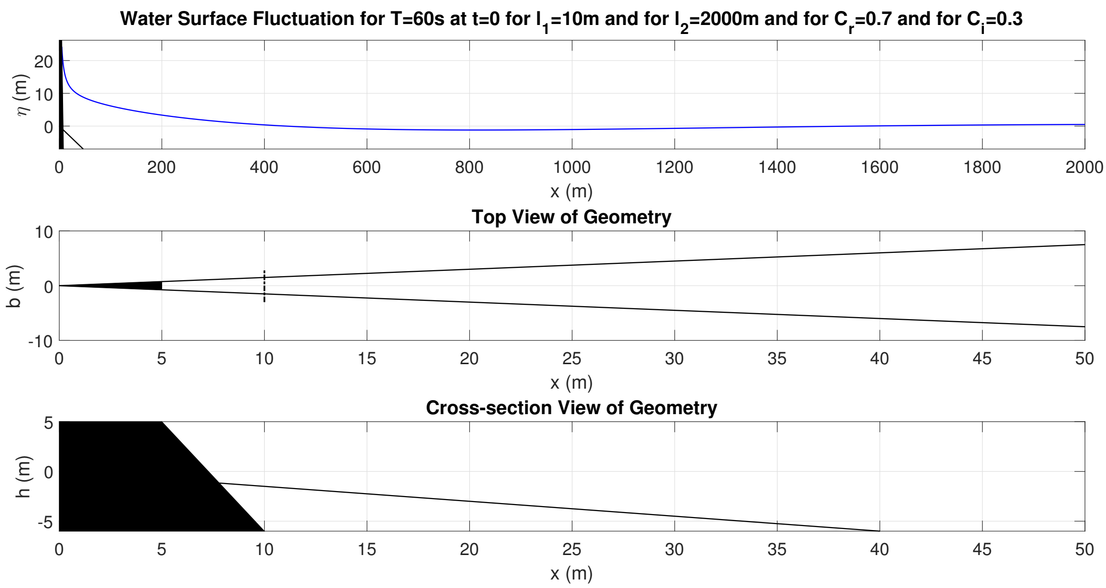

Figure 3.6 : Water surface fluctuation (η) for the profile with linear breadth variation $b(x) = 0.3x$ and linear depth variation $h(x) = 0.15x$ with $C_r = 0.7$, and $C_i = 0.3$ with a solid inclined wall.

which we expressed with Eq. (2.38) in Chapter 2, we notice that there is an extra $-Y_1(2k\sqrt{l_1})C_w\sqrt{l_1}$ expression in the multipliers of the expressions with J_1 functions in both the numerator and denominator. Likewise, we notice that there is an extra $-J_1(2k\sqrt{l_1})C_w\sqrt{l_1}$ expression in the multipliers of expressions with Y_1 functions in both the numerator and denominator. We can make a graphical interpretation of this difference by comparing Fig. 3.6 and Fig. 2.8. When we examine these figures, it is observed that in Fig. 3.6, that is, in the case of the inclined wall, the wave height is approximately 2.5 times that in the case of the vertical wall.

3.4 Nonlinear Breadth Variation ($b(x) = c_2x^c$ with $c = 1/3$) with a Solid Inclined Wall

Now, we study the nonlinear breadth variation for the $c = 1/3$ case. As previously, the depth is constant ($a = 0$), bringing the only limitations coming from the long wave theory. A solid inclined wall in such a domain is seen in Fig. 3.7. In this instance, the Bessel-Z equation parameters provided in Eq. (1.76) may be calculated as $\alpha = \frac{2}{2-a} = 1$

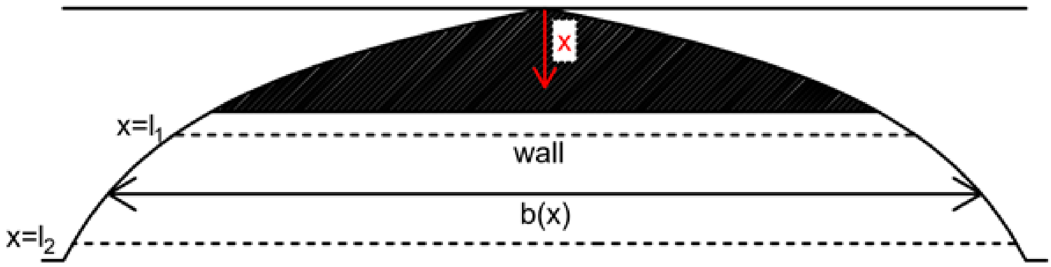

Figure 3.7 : Nonlinear breadth variation with a solid inclined wall.

and $\nu = \frac{1-a-c}{2-a} = 1/3$ for the values of $a = 0$ and $c = 1/3$. Consequently, the equation for Bessel-Z provided by Eq. (1.76) simplifies to

$$\frac{d}{dx}\left[x^{1/3}\frac{d\widehat{\eta}(x)}{dx}\right] + \frac{\sigma^2}{c_1 g}x^{1/3}\widehat{\eta} = 0 \tag{3.64}$$

and the solution given by Eq. (1.77) becomes

$$\widehat{\eta}(x) = x^{1/3}Z_{1/3}\left(\sqrt{\left|\frac{\sigma^2}{c_1 g}\right|}x\right). \tag{3.65}$$

For $\sigma^2/c_1 g = k^2 > 0$, $Z_{1/3}$ gives $J_{1/3}$ and $Y_{1/3}$ as before so that solution becomes

$$\widehat{\eta}(x) = Ax^{1/3}J_{1/3}(kx) + Bx^{1/3}Y_{1/3}(kx). \tag{3.66}$$

BC1 is imposed by taking the partial derivative of Eq. (3.66) with respect to x, giving

$$\frac{\partial\widehat{\eta}(x)}{\partial x} = A\left[\frac{2}{3}x^{-2/3}J_{1/3}(kx) - kx^{1/3}J_{4/3}(kx)\right] + B\left[\frac{2}{3}x^{-2/3}Y_{1/3}(kx) - kx^{1/3}Y_{4/3}(kx)\right]. \tag{3.67}$$

Applying BC1, $\frac{\partial\eta}{\partial x} + C_w k\eta\Big|_{x=l_1} = 0$, results in

$$A = -B\frac{\left[(\frac{2}{3} + C_w kl_1)Y_{1/3}(kl_1) - kl_1 Y_{4/3}(kl_1)\right]}{\left[(\frac{2}{3} + C_w kl_1)J_{1/3}(kl_1) - kl_1 J_{4/3}(kl_1)\right]}. \tag{3.68}$$

Again, application of BC2 as before gives

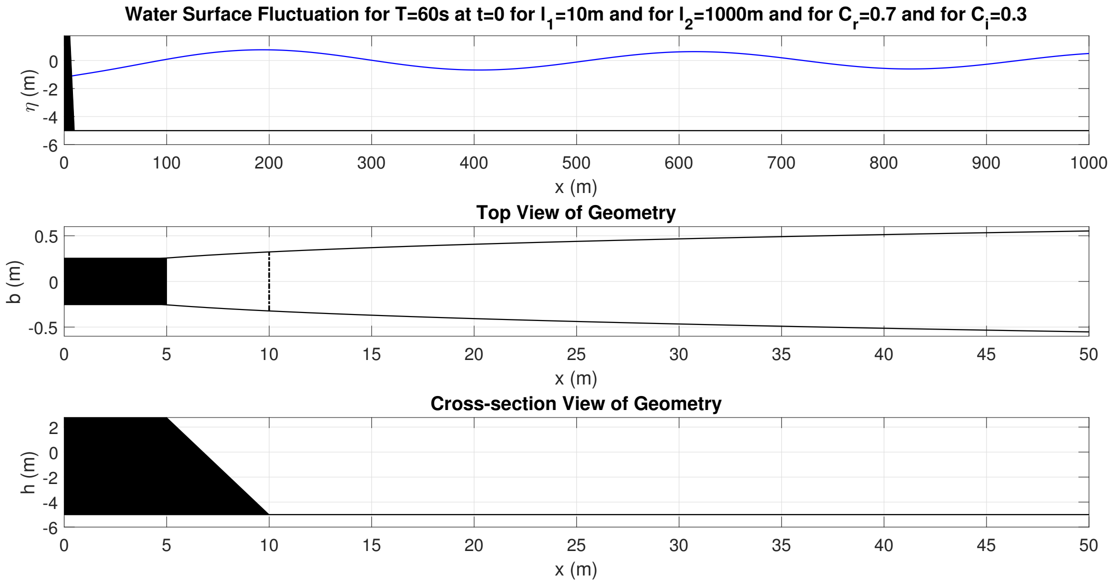

Figure 3.8 : Water surface fluctuation (η) for constant depth $h(x) = -5$ with nonlinear breadth variation $b(x) = 0.3x^{1/3}$ with $C_r = 0.7$, and $C_i = 0.3$ with a solid inclined wall.

$$\eta|_{x=l_2} = \frac{H}{2}\cos(\sigma t) = \left[A{l_2}^{1/3}J_{1/3}(kl_2) + B{l_2}^{1/3}Y_{1/3}(kl_2)\right]\cos(\sigma t) \tag{3.69}$$

that results in

$$A{l_2}^{1/3}J_{1/3}(kl_2) + B{l_2}^{1/3}Y_{1/3}(kl_2) = \frac{H}{2}. \tag{3.70}$$

By concurrently solving Eq. (3.68) and Eq. (3.70), the solution may be obtained as

$$\begin{aligned}\eta(x,t) = \frac{H}{2{l_2}^{1/3}}\Bigg(&\frac{-\kappa_2}{Y_{1/3}(kl_2)\kappa_1 - J_{1/3}(kl_2)\kappa_2}x^{1/3}J_{1/3}(kx) \\ &+ \frac{\kappa_1}{Y_{1/3}(kl_2)\kappa_1 - J_{1/3}(kl_2)\kappa_2}x^{1/3}Y_{1/3}(kx)\Bigg)\cos(\sigma t)\end{aligned} \tag{3.71}$$

where $\kappa_1 = \left[(\frac{2}{3} + C_w kl_1)J_{1/3}(kl_1) - kl_1 J_{4/3}(kl_1)\right]$ and $\kappa_2 = \left[(\frac{2}{3} + C_w kl_1)Y_{1/3}(kl_1) - kl_1 Y_{4/3}(kl_1)\right]$. If $\alpha = 1, \nu = 1/3$ are set in Eq. (3.30), the same solution may also be obtained.

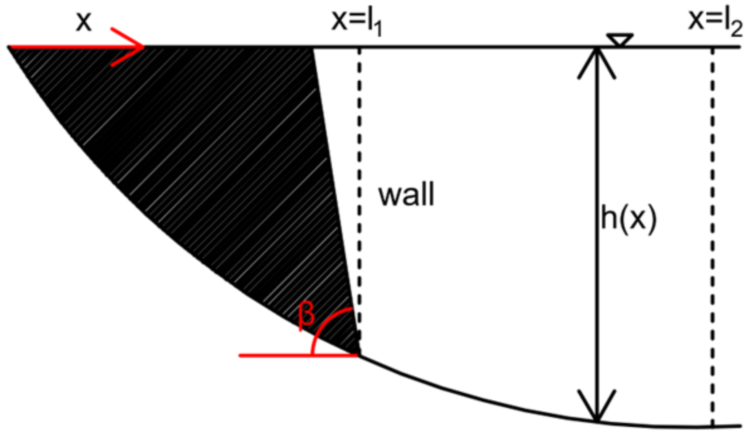

Figure 3.9 : Nonlinear depth variation with a solid inclined wall.

Fig. 3.8 illustrates the water surface fluctuation that was produced for the nonlinear breadth variation. $T = 60\ s$, $c_1 = 5\ m$, $c_2 = 0.3\ m^{2/3}$, $a = 0$, $c = 1/3$, $l_1 = 10\ m$, $l_2 = 1000\ m$, $C_r = 0.7$, and $C_i = 0.3$ values at time $t = 0\ s$ are chosen as the computational parameters for this illustrative case.

The $\eta(x,t)$ value we obtained for the inclined wall, which we expressed with Eq. (3.71), is symbolically the same as the $\eta(x,t)$ value we obtained for the vertical wall, which we expressed with Eq. (2.46) in Chapter 2. However, when the κ_1 and κ_2 parameters here are compared with the parameters in Chapter 2, it is observed that there are extra $C_w k l_1$ terms in the coefficients of the $J_{1/3}(kl_1)$ and $Y_{1/3}(kl_1)$ functions due to the inclined wall. We can make a graphical interpretation of this difference by comparing Fig. 3.8 and Fig. 2.10. When we examine these figures, it is observed that in Fig. 3.8, that is, in the case of the inclined wall, there is less water surface fluctuation compared to the case of the vertical wall.

3.5 Nonlinear Depth Variation ($h(x) = c_1 x^a$ with $a = 2/3$) with a Solid Inclined Wall

In this section, we take into account a nonlinear depth variation of the form $h(x) = c_1 x^a$ for $a = 2/3$, where the breadth is unbounded. Such a choice of depth profile matches the equilibrium beach profile shape initially determined by [48], as explained in Eq. (1.77). The impact of the solid inclined wall is represented in Fig. 3.9, which illustrates such a geometry.

In this case, $\alpha = \frac{2}{2-a} = 3/2$ and $\nu = \frac{1-a-c}{2-a} = 1/4$ are the Bessel-Z equation parameters that can be calculated for the values of $a = 2/3$ and $c = 0$. Consequently, the equation for Bessel-Z provided by Eq. (1.76) simplifies to

$$\frac{d}{dx}\left[x^{2/3}\frac{d\widehat{\eta}(x)}{dx}\right] + \frac{\sigma^2}{c_1 g}\widehat{\eta} = 0 \tag{3.72}$$

and Eq. (1.77) turns into

$$\widehat{\eta}(x) = x^{1/6} Z_{1/4}\left(\frac{3}{2}\sqrt{\left|\frac{\sigma^2}{c_1 g}\right|} x^{2/3}\right). \tag{3.73}$$

Once again, the function $Z_{1/4}$ represents $J_{1/4}$ and $Y_{1/4}$ assuming $\sigma^2/c_1 g = k^2 > 0$.

$$\widehat{\eta}(x) = A x^{1/6} J_{1/4}\left(\frac{3}{2}kx^{2/3}\right) + B x^{1/6} Y_{1/4}\left(\frac{3}{2}kx^{2/3}\right). \tag{3.74}$$

At $x = l_1$ for all t, the solid inclined wall boundary condition (BC1) is equal to $\frac{\partial \eta}{\partial x} + C_w k \eta = 0$, which is again imposed by taking the partial derivative of Eq. (3.74) with respect to x. This gives the derivative as

$$\begin{aligned}\frac{\partial \widehat{\eta}(x)}{\partial x} = &A\left[\frac{1}{3}x^{-5/6} J_{1/4}\left(\frac{3}{2}kx^{2/3}\right) - kx^{-1/6} J_{5/4}\left(\frac{3}{2}kx^{2/3}\right)\right] \\ &+ B\left[\frac{1}{3}x^{-5/6} Y_{1/4}\left(\frac{3}{2}kx^{2/3}\right) - kx^{-1/6} Y_{5/4}\left(\frac{3}{2}kx^{2/3}\right)\right].\end{aligned} \tag{3.75}$$

Imposing BC1 as before yields

$$A = -B\frac{\left[(\frac{1}{3} + C_w k l_1) Y_{1/4}\left(\frac{3}{2}k{l_1}^{2/3}\right) - {l_1}^{2/3} k Y_{5/4}(\frac{3}{2}k{l_1}^{2/3})\right]}{\left[(\frac{1}{3} + C_w k l_1) J_{1/4}(\frac{3}{2}k{l_1}^{2/3}) - {l_1}^{2/3} k J_{5/4}(\frac{3}{2}k{l_1}^{2/3})\right]}. \tag{3.76}$$

Just like previously, imposing the open ocean boundary condition (BC2) yields

$$A{l_2}^{1/6} J_{1/4}\left(\frac{3}{2}k{l_2}^{2/3}\right) + B{l_2}^{1/6} Y_{1/4}\left(\frac{3}{2}k{l_2}^{2/3}\right) = \frac{H}{2}. \tag{3.77}$$

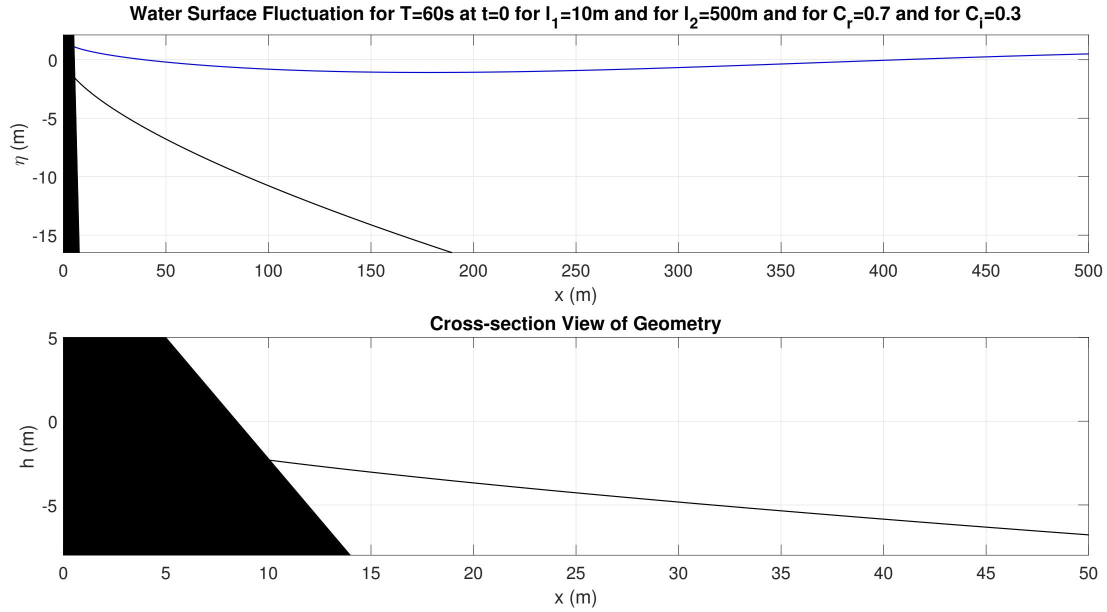

Figure 3.10 : Water surface fluctuation (η) for unbounded breadth and nonlinear depth profile of $h(x) = 0.5x^{2/3}$ with $C_r = 0.7$, and $C_i = 0.3$ with a solid inclined wall.

By simultaneously solving Eq. (3.76) and Eq. (3.77), the water surface fluctuation solution may be obtained as

$$\eta(x,t) = \frac{H}{2{l_2}^{1/6}}\left[\frac{-\psi_2}{Y_{1/4}\left(\frac{3}{2}k{l_2}^{2/3}\right)\psi_1 - J_{1/4}\left(\frac{3}{2}k{l_2}^{2/3}\right)\psi_2}x^{1/6}J_{1/4}\left(\frac{3}{2}kx^{2/3}\right)\right.$$
$$\left.+\frac{\psi_1}{Y_{1/4}\left(\frac{3}{2}k{l_2}^{2/3}\right)\psi_1 - J_{1/4}\left(\frac{3}{2}k{l_2}^{2/3}\right)\psi_2}x^{1/6}Y_{1/4}\left(\frac{3}{2}kx^{2/3}\right)\right]\cos(\sigma t). \tag{3.78}$$

Here $\psi_1 = \left[(\frac{1}{3} + C_w k l_1)J_{1/4}(\frac{3}{2}k{l_1}^{2/3}) - {l_1}^{2/3}kJ_{5/4}(\frac{3}{2}k{l_1}^{2/3})\right]$ and $\psi_2 = \left[(\frac{1}{3} + C_w k l_1)Y_{1/4}\left(\frac{3}{2}k{l_1}^{2/3}\right) - {l_1}^{2/3}kY_{5/4}(\frac{3}{2}k{l_1}^{2/3})\right]$. As previously, by inserting $\alpha = 3/2, \nu = 1/4$ in Eq. (3.30), the same solution may be achieved.

Fig. 3.10 illustrates this fluctuation in the water surface that was derived as the solution of the long wave problem for the nonlinear depth variation. The following values are used for the computational parameters: $T = 60\,s$, $c_1 = 0.5\,m^{1/3}$, $c_2 = 1$, $a = 2/3$, $c = 0$, $l_1 = 10\,m$, $l_2 = 500\,m$, $C_r = 0.7$, and $C_i = 0.3$ at time $t = 0\,s$.

The $\eta(x,t)$ value we obtained for the inclined wall, which we expressed with Eq. (3.78), is symbolically the same as the $\eta(x,t)$ value we obtained for the vertical wall, which we expressed with Eq. (2.53) in Chapter 2. However, when the ψ_1 and ψ_2 parameters here are compared with the parameters in Chapter 2, it is observed that there are extra $C_w kl_1$ terms in the coefficients of the $J_{1/4}(\frac{3}{2}kl_1{}^{2/3})$ and $Y_{1/4}(\frac{3}{2}kl_1{}^{2/3})$ functions due to the inclined wall. We can make a graphical interpretation of this difference by comparing Fig. 3.10 and Fig. 2.12. When we examine these figures, it is observed that although the level of water surface fluctuation in Fig. 3.10, that is, the inclined wall situation and the vertical wall situation, is almost the same, there is a difference in the water levels at $x = 0$. In the case of the inclined wall, the water level is positive at $x = 0$.

3.6 Nonlinear Breadth and Depth Variation ($b(x) = c_2x^c$ with $c = 1/2$ and $h(x) = c_1x^a$ with $a = 1/2$) with a Solid Inclined Wall

Finally, we examine the scenario in which there is a solid inclined wall in a nonlinear wedge-shaped geometry which is illustrated in Fig. 3.11. Here, both the breadth and depth changes are nonlinear. In this instance, the Bessel-Z equation parameters provided in Eq. (1.76) may be computed as $\alpha = \frac{2}{2-a} = 4/3$ and $\nu = \frac{1-a-c}{2-a} = 0$, since the parameters are chosen to be $a = 1/2$ and $c = 1/2$. Eq. (1.76) reduces to

$$\frac{d}{dx}\left[x\frac{d\widehat{\eta}(x)}{dx}\right] + \frac{\sigma^2}{c_1 g}x^{1/2}\widehat{\eta} = 0 \tag{3.79}$$

and the solution given by Eq. (1.77) reduces to

$$\widehat{\eta}(x) = Z_0\left(\frac{4}{3}\sqrt{\left|\frac{\sigma^2}{c_1 g}\right|}x^{3/4}\right). \tag{3.80}$$

As before, for real values of σ, the solution can be written as

$$\widehat{\eta}(x) = AJ_0\left(\frac{4}{3}kx^{3/4}\right) + BY_0\left(\frac{4}{3}kx^{3/4}\right). \tag{3.81}$$

By calculating the partial derivative of Eq. (3.56) with regards to x, Eq. (3.82) is obtained as

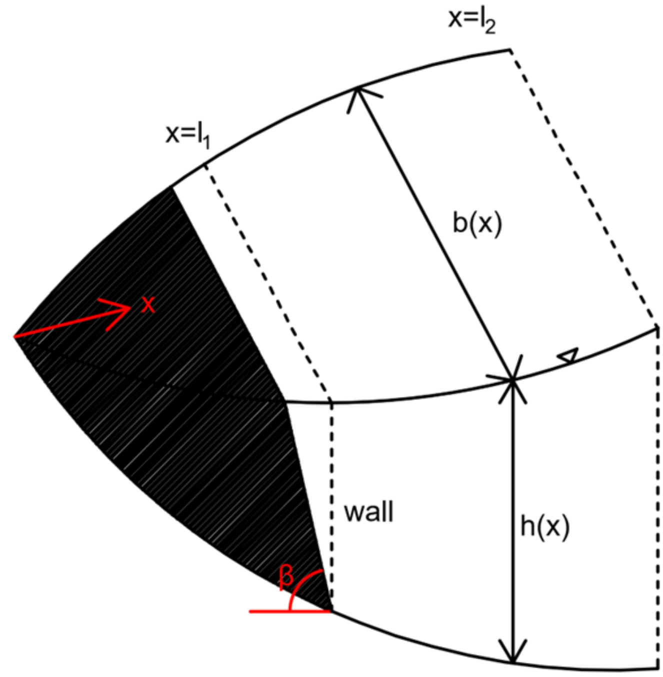

Figure 3.11 : Nonlinear breadth and depth variation with a solid inclined wall.

$$\frac{\partial \widehat{\eta}(x)}{\partial x} = -Akx^{-1/4}J_1\left(\frac{4}{3}kx^{3/4}\right) - Bkx^{-1/4}Y_1\left(\frac{4}{3}kx^{3/4}\right). \tag{3.82}$$

Imposing BC1, $\frac{\partial \eta}{\partial x} + C_w k\eta\Big|_{x=l_1} = 0$, yields

$$A = -B\frac{\left[Y_1\left(\frac{4}{3}k{l_1}^{3/4}\right) - C_w {l_1}^{1/4} Y_0\left(\frac{4}{3}k{l_1}^{3/4}\right)\right]}{\left[J_1\left(\frac{4}{3}k{l_1}^{3/4}\right) - C_w {l_1}^{1/4} J_0\left(\frac{4}{3}k{l_1}^{3/4}\right)\right]}. \tag{3.83}$$

Imposing BC2 (the open ocean) gives

$$AJ_0\left(\frac{4}{3}k{l_2}^{3/4}\right) + BY_0\left(\frac{4}{3}k{l_2}^{3/4}\right) = \frac{H}{2}. \tag{3.84}$$

By simultaneously solving Eq. (3.83) and Eq. (3.84), the water surface fluctuation solution may be obtained as

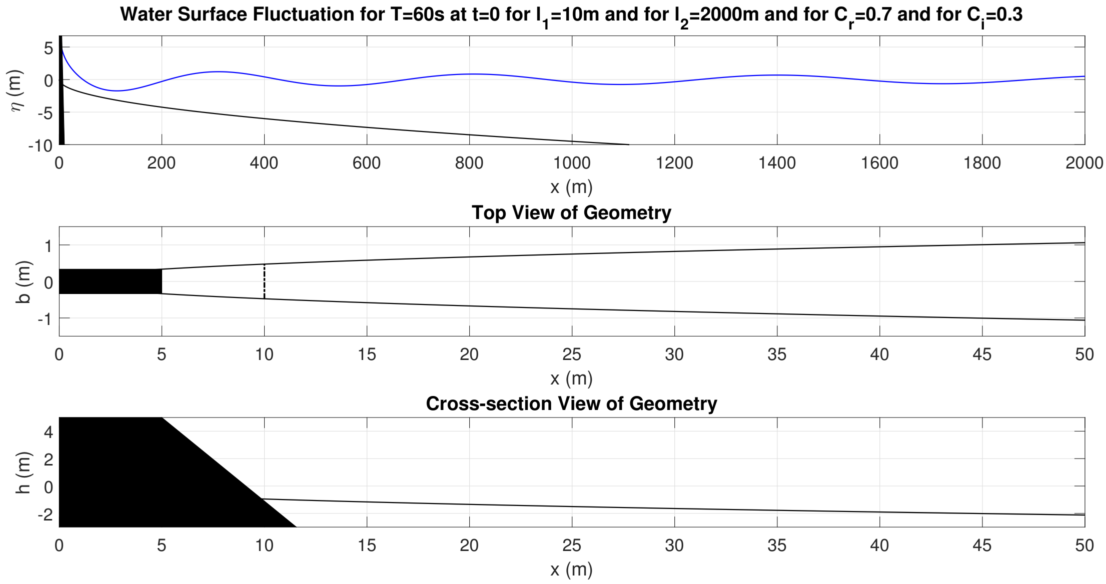

Figure 3.12 : Water surface fluctuation (η) for nonlinear breadth variation $b(x) = 0.3x^{1/2}$ and nonlinear depth variation $h(x) = 0.3x^{1/2}$ with $C_r = 0.7$, and $C_i = 0.3$ with a solid inclined wall.

$$\eta(x,t) = \frac{H}{2}\left[\frac{-\tau_2}{Y_0\left(\frac{4}{3}kl_2{}^{3/4}\right)\tau_1 - J_0\left(\frac{4}{3}kl_2{}^{3/4}\right)\tau_2} J_0\left(\frac{4}{3}kx^{3/4}\right)\right.$$
$$\left. + \frac{\tau_1}{Y_0\left(\frac{4}{3}kl_2{}^{3/4}\right)\tau_1 - J_0\left(\frac{4}{3}kl_2{}^{3/4}\right)\tau_2} Y_0\left(\frac{4}{3}kx^{3/4}\right)\right]\cos(\sigma t). \tag{3.85}$$

Here $\tau_1 = \left[J_1\left(\frac{4}{3}kl_1{}^{3/4}\right) - C_w l_1{}^{1/4} J_0\left(\frac{4}{3}kl_1{}^{3/4}\right)\right]$ and $\tau_2 = \left[Y_1\left(\frac{4}{3}kl_1{}^{3/4}\right) - C_w l_1{}^{1/4} Y_0\left(\frac{4}{3}kl_1{}^{3/4}\right)\right]$. As previously, setting $\alpha = 4/3, \nu = 0$ in Eq. (3.30), the same solution may be achieved.

Fig. 3.12 illustrates the water surface fluctuation that was produced for the nonlinear breadth and depth variation. The values for the computational parameters at time $t = 0\,s$ are $T = 60\,s$, $c_1 = 0.3\,m^{1/2}$, $c_2 = 0.3\,m^{1/2}$, $a = 1/2$, $c = 1/2$, $l_1 = 10\,m$, $l_2 = 2000\,m$, $C_r = 0.7$, and $C_i = 0.3$.

If we compare the outcomes, although we cannot make a direct interpretation of the $\eta(x,t)$ value we obtained for the inclined wall, which we expressed with Eq. (3.85), and the $\eta(x,t)$ value we obtained for the vertical wall, which we expressed with Eq. (2.60) in Chapter 2, since they are slightly different in representation, we can say that there is an extra $-C_w {l_1}^{1/4}$ parameter in the coefficients of the J_0 and Y_0 functions in Eq. (3.85) due to the inclined wall by looking at the τ_1 and τ_2 parameters in it. We can make a graphical interpretation of this difference by comparing Fig. 3.12 and Fig. 2.14. When we examine these figures, we observe that in Fig. 3.12, that is, in the case of the inclined wall, the wave height is approximately 1 m higher than in the case of the vertical wall. However, in the case with the inclined wall, the l_2 value is set to 2000 m to avoid the breaking wave option and is twice that in the case with the vertical wall. Therefore, a clear comment cannot be made about the difference in wave height between these two situations.

3.7 Solutions in Terms of Cauchy-Euler Series for Geometries with Solid Inclined Wall

As we mentioned in Chapter 2 within the frame of Publication Number 1, the solutions to the long-wave equation provided by Eq. (1.75) for a uniform beach breadth and a parabolic bathymetry are well known to be in terms of the Cauchy-Euler series [47]. When $a = 2$ is established, parabolic bathymetry function in the form $h_{par}(x) = c_1 x^2$ is achieved. This holds true for any arbitrary width profile.

Again in Chapter 2 within the frame of Publication Number 1, we mentioned lengthily the governing equation (Eq. (2.62)) is referred to as the Cauchy-Euler equation [47], and examined how to solve this equation in detail. We analyzed the characteristics of the potential solutions and made some inferences based on these solutions. In Chapter 3 within the frame of Publication Number 2, that is, in the case of the inclined wall, the general solutions in terms of the Cauchy-Euler Series are the same as the inferences and interpretations we mentioned in Chapter 2. However, although the BC2s are the same (for both vertical wall and inclined wall case BC2: $\eta(x,t) = \frac{H}{2}\cos(\sigma t)$ at $x = l_2$), the BC1s are different (for vertical wall case BC1: $\frac{\partial \eta(x,t)}{\partial x} = 0$ at $x = l_1$ for all t, for inclined wall case BC1: $\frac{\partial \eta(x,t)}{\partial x} + C_w k \eta(x,t) = 0$ at $x = l_1$ for all t where $C_w = C_r + iC_i$), so the particular solution for the inclined wall case is different from the particular solution for the vertical wall case. To achieve this particular solution, BC1 valid for inclined wall must be enforced. To see these implications and conclusions, please kindly check Chapter 2.

4. THE PREDICTABILITY OF THE 30 OCTOBER 2020 İZMIR-SAMOS TSUNAMI HYDRODYNAMICS AND ENHANCEMENT OF ITS EARLY WARNING TIME BY LSTM DEEP LEARNING NETWORK[3]

Tsunamis are defined as surface water waves that can have a long-range and reach thousands of kilometers from their source [86,87]. They are destructive since their energy is concentrated close to a front moving at the maximum group velocity $\sqrt{gh}$, where h (considered to be constant) is the water depth [88]. Tsunamis may occur with a displacement of the water column due to reasons such as earthquakes, submarine or atmospheric events, volcanic eruptions, etc. [89]. Throughout history, there has been great material damage and loss of life due to tsunamis in coastal and inland regions [86]. Tsunamis, like other natural disasters, are natural events that are almost impossible to prevent, but whose effects can be minimized with some scientific studies. There are many studies in the literature on this subject. To assess the changes in land use and land cover brought on by the great East Japan earthquake disaster in 2011, a precise land use and land cover map for the years 2013 to 2015 post-disaster with a 30-m spatial resolution is generated in [90]. An analysis of assessing and mapping the geographical and temporal consequences of the tsunami on land use and land cover, as well as the availability of associated ecosystem services in the Thai province of Phang Nga is presented in [91]. On an approximately 4.5 km shore-normal section on the shoreline region around Sendai, Japan; erosion, deposition, and related alterations to the landscape are established as a result of the Tohoku-oki tsunami in 2011 in [92]. The effects of a large tsunami on a low-lying coastal area in eastern Japan are determined using a mix of time-series satellite images, aerial videos, and observation from the ground; and an analysis is made between a shoreline with armored barriers and one without in [93]. The potential use of compressive sensing for the accurate measurement and modeling of the tsunami parameters, namely, water surface fluctuation, velocity,

[3]This chapter is based on the paper "Alan A. R., Bayındır, C., Ozaydin, F., Altintas, A. A. (2023). The Predictability of the 30 October 2020 İzmir-Samos Tsunami Hydrodynamics and Enhancement of Its Early Warning Time by LSTM Deep Learning Network, *Water,* 15(23), 4195.".

and wave pressures are examined in [94]. Despite being examined for tsunami disasters quite a lot of times with traditional observation methods such as satellite imaging, newer and technological methods have been preferred due to the inadequacy of the old methods and the demands for more detailed and useful results. For example, remote sensing is a technique that makes it possible to map and evaluate regions damaged or likely to be damaged by tsunami using satellite images [95]. Because of the large size of tsunami impact areas, recent developments in remote sensing and associated application technologies have made it feasible to use remotely sensed image data for mapping catastrophe damage distribution and determining an area's risk [96]. Another recent tsunami event took place on 30 October 2020 at 12:51 p.m. UTC (2:51 p.m. GMT+03:00) after an earthquake of 6.9 Mw, and this event is investigated by some field surveys such as [97]. Although the magnitude of the earthquake and the resulting 30 October 2020 İzmir-Samos (Aegean) tsunami flood characteristics such as the tsunami height and maximum runup are not among the most devastating ones on the earth, it was a remarkable milestone for the coastal communities along the Turkish coast of İzmir, especially at the town of Sığacık [97] due to its catastrophic consequences. The 30 October 2020 İzmir-Samos (Aegean) tsunami and its effect on various surrounding regions became and attraction of research in the recent years and many other field surveys and studies are given in the literature. For example the another field survey is conducted at the Samos island is presented in [98]. Relative sea level changes and morphotectonic implications triggered by the tsunami event is analyzed in [99]. A statistical and criticality analysis of the lower ionosphere prior to the earthquake event in performed in [100].

On the other hand, some applications of AI for tsunami data analysis are proposed in the literature. Real-time prediction of tsunami magnitudes in Osaka Bay, Japan is performed using an artificial neural network in [101]. An inverse modeling technique for the estimation of tsunami characteristics from deposits using a deep-learning neural network is studied in [102]. Early warning of tsunami inundation using convolutional neural networks and some other machine learning algorithms is analyzed in some studies such as [103]–[105]. In another paper, coastal tsunami prediction based on S-net observations using artificial neural network for the Tohoku, Japan is studied [106].

As one of the very successful DL networks, LSTM attracted some attention for tsunami disaster applications only very recently [107]–[109]. The performance of the LSTM, bi-directional LSTM and convolutional neural network–LSTM networks in predicting mean lower low water levels are analyzed in [107] where the data of two specific events recorded in Arkansas and New England/Maryland are used. The performance of recurrent neural network vs LSTM and gated recurrent units are studied in [108] where synthetic tsunami data is used. The spatiotemporal extrapolation of population data in areas prone to earthquakes and tsunamis in Lima, Peru are analyzed in [109].

This paper aims to examine the hydrodynamic characteristics and the predictability of the 30 October 2020 İzmir-Samos tsunami by using the LSTM DL network applied to data acquired using in situ and remote sensing techniques. For this purpose, we examine the prediction of the tsunami water surface fluctuation time series at different stations obtained by pressure gauges and radar and discuss their predictability using the LSTM deep learning network. We discuss the time series dynamics, root-mean-square-error (RMSE), and the spectral features of the predictions that are obtained by FFT routines. We also investigate the effect of the training data set on the performance of tsunami time series prediction both in the time as well as the spectral domain. Possible enhancement of the early warnings and early warning time scales are also discussed.

4.1 Methodology

4.1.1 Study area

On 30 October 2020 at 12:51 p.m. UTC, an earthquake with a moment magnitude of 6.9 Mw with its epicenter off the Greek island of Samos, approximately 23 km south of İzmir occurred [110]–[112]. The analysis carried after the kinematic rupture process of the earthquake indicated the cascaded rupture of two fault planes, with slightly rotated strike angles, and dominated by normal faulting and oblique faulting, respectively [112]. Not only seismic and geodetic but also tsunami data was used

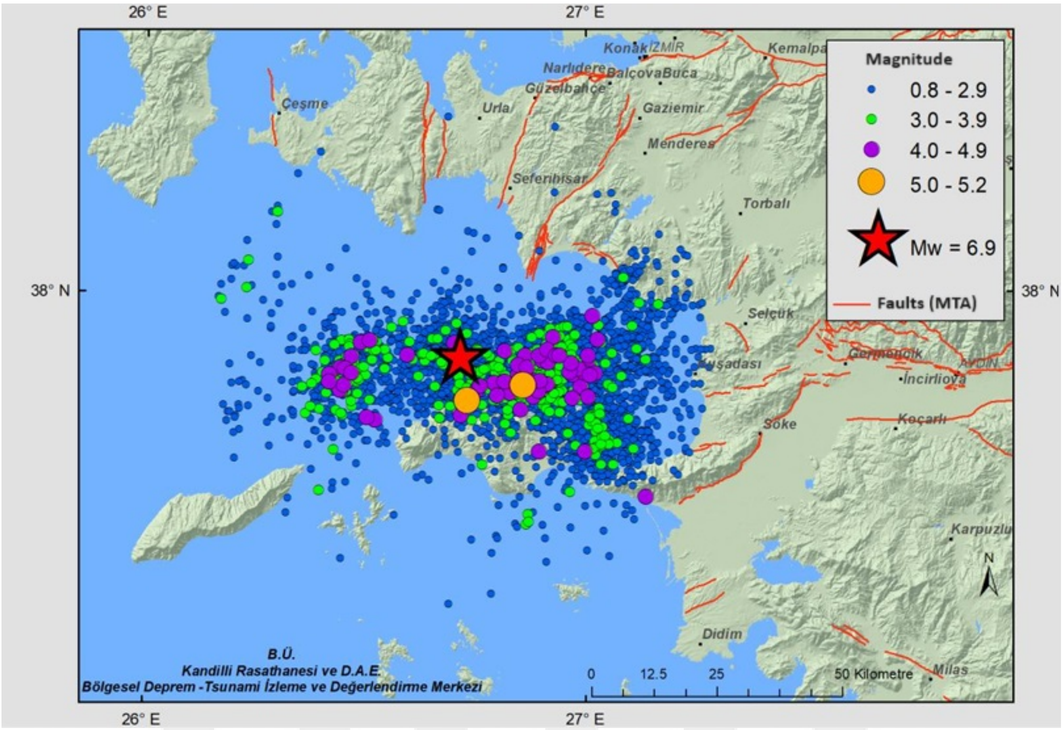

Figure 4.1 : 30 October 2020 İzmir-Samos Earthquake seismicity map [113] (Figure courtesy of KOERI and permission to reuse of this figure is obtained from Prof. Dr. Doğan Kalafat).

to analyze earthquake characteristics [112]. The seismicity map shown in Fig. 4.1 indicates the epicenter of the earthquake and the locations of 5068 aftershocks recorded on that day [113]. The earthquake's epicenter is located on the İzmir-Balikesir Transfer Zone, which extends down to Samos Island [112]. The primary seismogenic fault of the 2020 Samos earthquake is considered to be the Kaystrios Fault [112]. Kaystrios Fault along with Ikaria, Fourni, and Pythagorio Faults in the vicinity, compose a complex fault system [112]. Although the magnitude of this earthquake and the resulting 30 October 2020 İzmir-Samos (Aegean) Tsunami was not very big compared to their counterparts observed on other places on Earth, it was a major event and was of critical importance to the region. The tsunami triggered by the earthquake caused significant inundation and damage along the Turkish coastal town of Sığacık.

The study map of the 30 October 2020 İzmir-Samos tsunami, with its earthquake epicenter and surrounding UNESCO tsunami observation stations, is depicted in Fig. 4.2. As the figure depicts, the closest UNESCO stations are located at Bodrum, Syros, Kos, and Kos Marina [114]. The time series data used

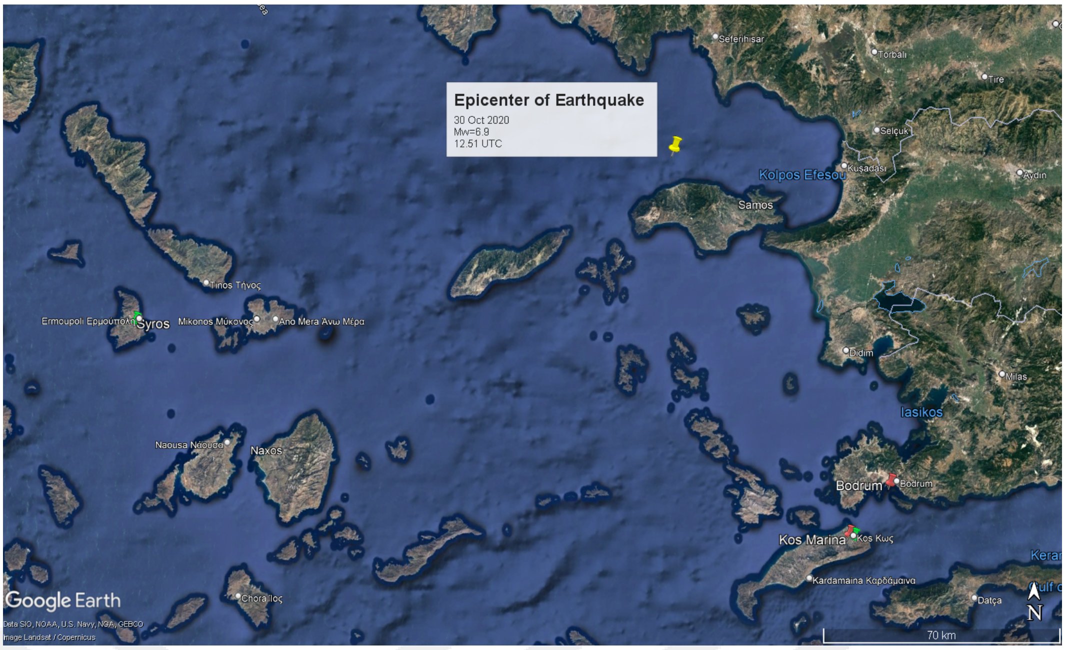

Figure 4.2 : 30 October 2020 İzmir-Samos earthquake epicenter and surrounding UNESCO tsunami observation stations: Bodrum, Syros, Kos and Kos Marina [114].

in this study are downloaded from the UNESCO website at `https://www.ioc-sealevelmonitoring.org/map.php` (accessed on 29 November 2023) and it is publicly available.

Daily data from 30 October 2020-00:00 a.m. to 31 October 2020-00:00 a.m. UTC are obtained from all of the 4 stations mentioned above. It is useful to mention that the sampling time at the Bodrum Station is 0.5 min, whereas the sampling time for all remaining 3 stations are all 1 min. The recordings at the Bodrum Station and Syros Station are acquired by an acoustic echo sounder and a pressure gauge, respectively. The recordings at the Kos and Kos Marina Stations are acquired by radar.

The predictability of the tsunami event, its dynamics, and spectral features is the subject of this paper. More specifically, one of the very successful time series prediction tools of DL is the LSTM network, and it is studied as a possible candidate for the successful prediction of 30 October 2020 İzmir-Samos tsunami hydrodynamics. In the next section, we give a brief review of the LSTM network, and in further sections, we analyze the predictability of the 30 October 2020 İzmir-Samos tsunami using the LSTM DL network.

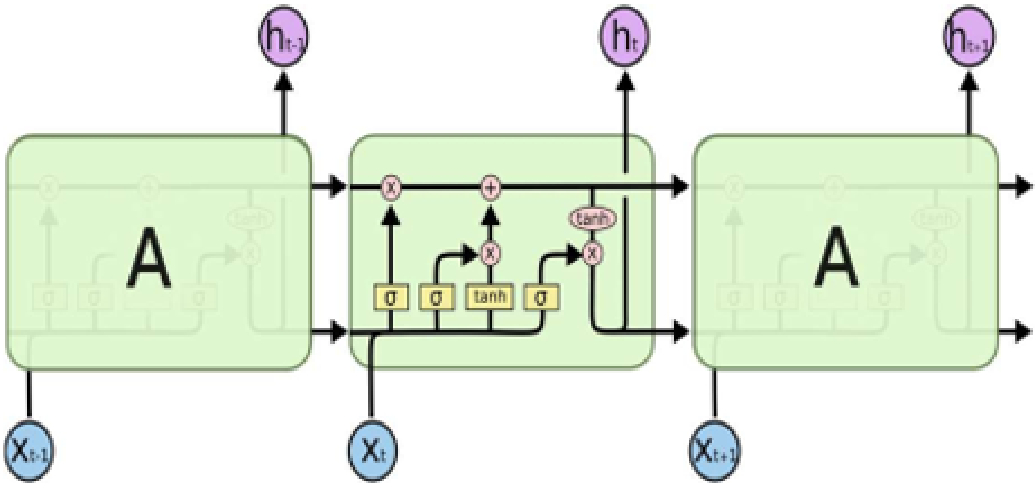

Figure 4.3 : LSTM network structure indicating input and output times series, gates and activation functions [116].

4.1.2 Review of the LSTM

Recurrent neural networks (RNN) which remain the most effective deep learning algorithms were created in the 1980s [115,116]. Forecasts can be made utilizing sequential data sets using RNN. One of those neural networks is the LSTM, and its structure is shown in Fig. 4.3 [115,116].

Up to the present, numerous studies include the utilization of RNN to analyze time series [115,116]. Nevertheless, if long data sets are being used it is known that gradient disappearance or gradient burst cases take place [115,116]. LSTM architecture was first developed in 1997 to overcome these problems [115]. Data flow is provided simply thanks to the forget gate, input gate, and output gate and additionally the memory cell outside of the input, which decides that the information will be forgotten, retained, and transferred [115,116]. The mathematical formulations of these gates reads:

(a) Forget Gate:

$$f_i^{(t)} = \sigma(b_i^f + \sum_y U_{i,j}^f x_j^{(t)} + \sum_y W_{i,j} h_j^{(t-1)}), \tag{4.1}$$

(b) State Unit:

$$s_i^{(t)} = f_i^{(t)} s_i^{(t-1)} + g_i^t \sigma(b_i^f + \sum_y U_i x_j^{(t)} + \sum_y W_i h_j^{(t-1)}), \tag{4.2}$$

(c) Input Gate:

$$g_i^{(t)} = \sigma(b_i^g + \sum_y U_i^g x_j^{(t)} + \sum_y W_i^g h_j^{(t-1)}), \tag{4.3}$$

(d) Output Gate:

$$q_i^{(t)} = \sigma(b_i^o + \sum_y U_{i,j}^o x_j^{(t)} + \sum_y W_{i,}^o h_j^{(t-1)}), \tag{4.4}$$

(e) The Output:

$$h_i^{(t)} = q_i^{(t)} tanh(s_i^{(t)}). \tag{4.5}$$

In these formulations bias values in the input, output, and forget gates are represented as b_i^f, b_i^g, b_i^o [115,116]. The input weights belonging to the gates are shown as $U_{i,j}^f$, $U_{i,j}^g$, $U_{i,j}^o$, $U_{i,j}$ [115,116]. The recurrent weights of the gate to which they belong to are denoted as $W_{i,j}^f$, $W_{i,j}^g$, $W_{i,j}^o$, $W_{i,j}$. The letter A indicates a chunk of the deep neural net. The input time series is shown as X parameter [115,116]. In all of our simulations we use 250 epochs with 1 iteration per epoch. The learning rate is selected to be 0.001 and the learning rate schedule is piecewise. A detailed discussion and analysis of the LSTM network and its applications can be seen in [115,116]. While it can be used for many different purposes including but not limited to speech and image recognition, and retrieval of transfer functions in systems theory, we use LSTM as a tsunami time series analysis tool in this study.

4.2 Results and Discussion

The data used in this study is downloaded from the UNESCO website mentioned above, and it is de-tided using a spectral approach to filter out the astronomical tidal effect. For this purpose, after zeroing out the mean, an FFT-IFFT procedure is used. The water surface fluctuation spectra are obtained via FFT, and the spectral amplitudes corresponding to central frequencies between $\pm 1\%$ frequencies around central frequency 0 giving approximately $[-3 \times 10^{-4}$ Hz, 3×10^{-4} Hz$]$ are zero-padded. Then, this filtered spectrum is inverted using an IFFT routine to construct the de-tided tsunami water surface fluctuation time series. The de-tided water surface fluctuation indicates a tsunami wave height on the order of approximately 8 cm at Bodrum station which is located at [latitude: 37.03217, longitude: 27.423453]; and is sheltered by mainland and islands. The de-tided water surface fluctuation,

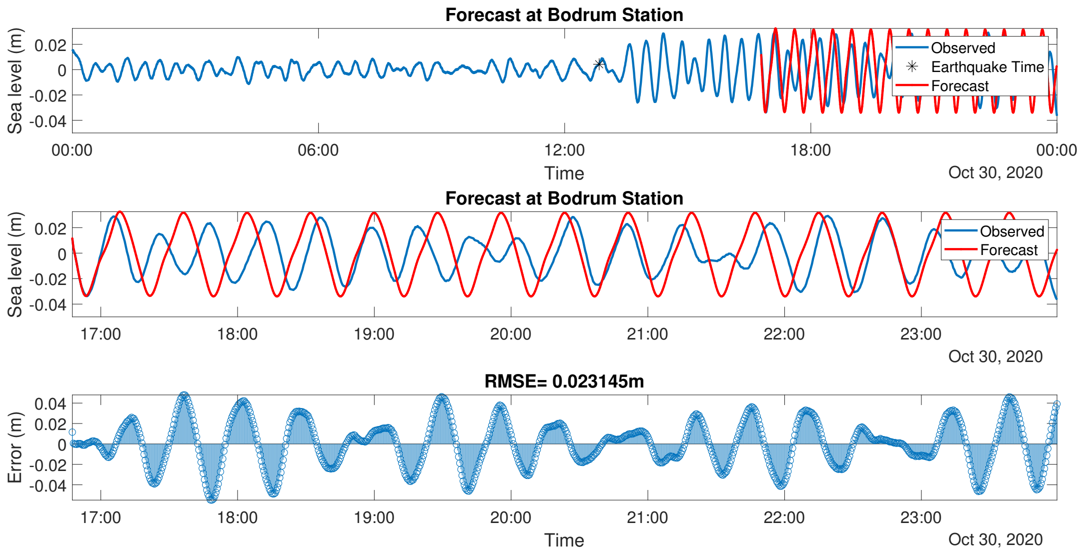

Figure 4.4 : Time series of the İzmir-Samos tsunami water surface fluctuation recorded at Bodrum station [114] on 30 October 2020 and its prediction by LSTM DL network-without updates.

its prediction by the LSTM network, and RMSE error between observations and predictions are depicted in Fig. 4.4. The 70% of the daily data set recorded at the Bodrum station is used as the training set, thus the training data set not only includes the pre-tsunami but also some of the post-tsunami recordings. The computation time for this data set is 63.93 s, whereas the computation time of the LSTM DL network is 52.00 s. These times are measured on a personal machine with an Intel Core i5 processor with 16 GB RAM and 512 GB SSD. The computation times for other data sets analyzed throughout this study are similar.

As shown in the figure, the predictions performed by LSTM can resolve the cyclic behavior. However, some shifts are present in the angular frequency of the oscillations compared to the actual recordings. The amplitude of the predictions is a better match for this data set compared to the frequencies. When an LSTM network with no updates is used, it means that only the training data set determines the success of predictions, thus actual recordings after predictions do not affect the further predictions. However, when an updated LSTM network is used, the predictions are updated according to the actual recordings of the prediction phase, thus the prediction time reduces to a one-time step. For the Bodrum Station data, this time step is 0.5 min. The results of the LSTM predictions with updates are depicted in Fig. 4.5.

As these figures confirm, the LSTM network with updates is much more successful in predicting the Bodrum station data in terms of matching the waveform of the oscillations of the water surface fluctuations, and the RMSE is significantly enhanced compared to the not-updated case. For the majority of the time series investigated in this paper, we observe a similar tendency, however, some exceptions can also be observed. To better visualize the matching of the time series of predictions with the time series of observations, again we employ a spectral approach and obtain the Fourier spectrum via FFT routines. The spectra of the predictions for not-updated and updated cases are depicted in Fig. 4.6.

Next, we repeat a similar analysis for the next station, which is Syros station located at [latitude: 37.438, longitude: 24.9411]. Compared to the Bodrum stations, Syros station is more prone to tsunami inundation since it is less sheltered by some islands as the station location map confirms. Thus, the tsunami wave height observed from the de-tided water surface fluctuation time series depicted in Fig. 4.7 is larger compared to its Bodrum counterpart, being approximately 0.17 cm.

In Fig. 4.7, we present the recorded water surface elevation time series of the 30 October 2020 Tsunami at the Syros station and its prediction with the LSTM DL network with no updates. The same predictions with the updated LSTM network are presented in Fig. 4.8. Comparing Figs. 4.7 and 4.8 it is possible to realize that again LSTM predictions become significantly better when an updated network is used. Better performance can be observed by checking the RMSE as well as the comparisons of the spectra depicted in Figs. 4.9 and 4.10.

It is interesting and useful to recognize that LSTM with updates is more successful in predicting the lower frequency components for the tsunami time series recorded at Syros station, however, for higher frequency components (shorter waves) an increase in the mismatch of the spectral amplitudes can be observed. One possible way to minimize such effects is to develop an LSTM DL network with some frequency band filters using FFT or similar routines.

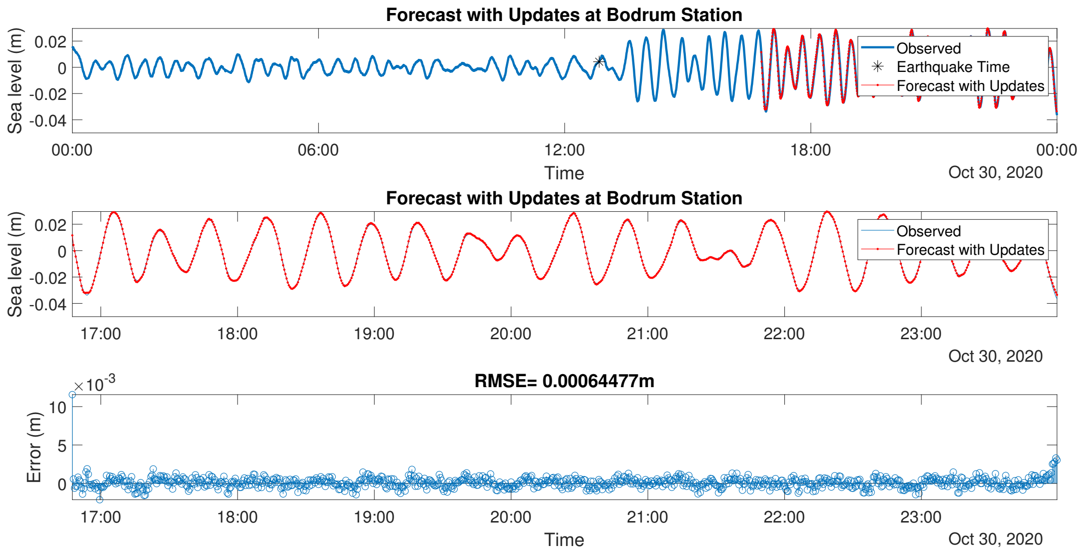

Figure 4.5 : Time series of the İzmir-Samos tsunami water surface fluctuation recorded at Bodrum station [114] on 30 October 2020 and its prediction by LSTM DL network-with updates.

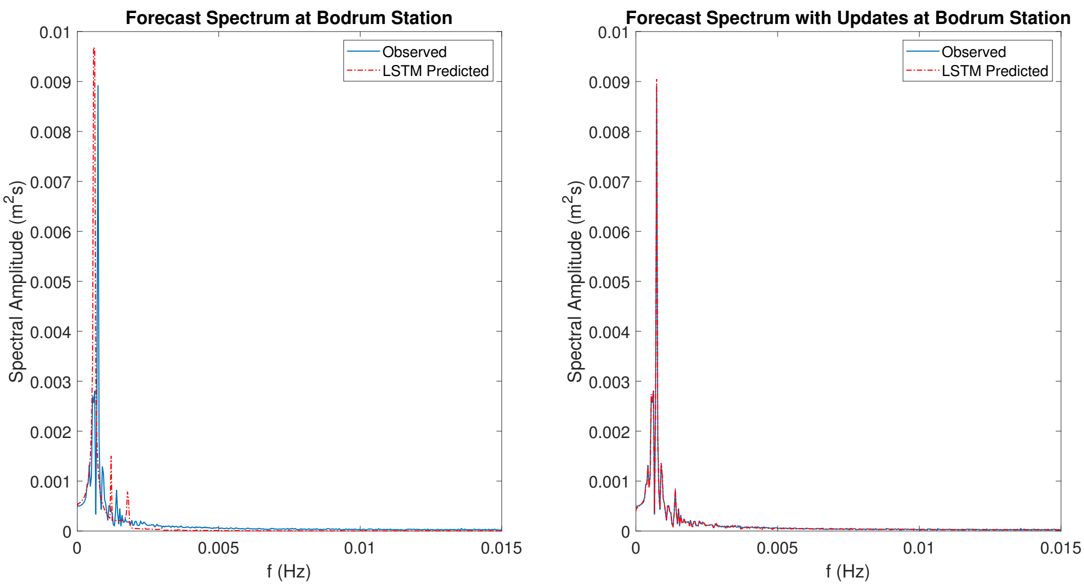

Figure 4.6 : Comparison of Fourier spectra of time series predictions performed by LSTM DL network at Bodrum Station on 30 October 2020 (**left**) without updates (**right**) with updates.

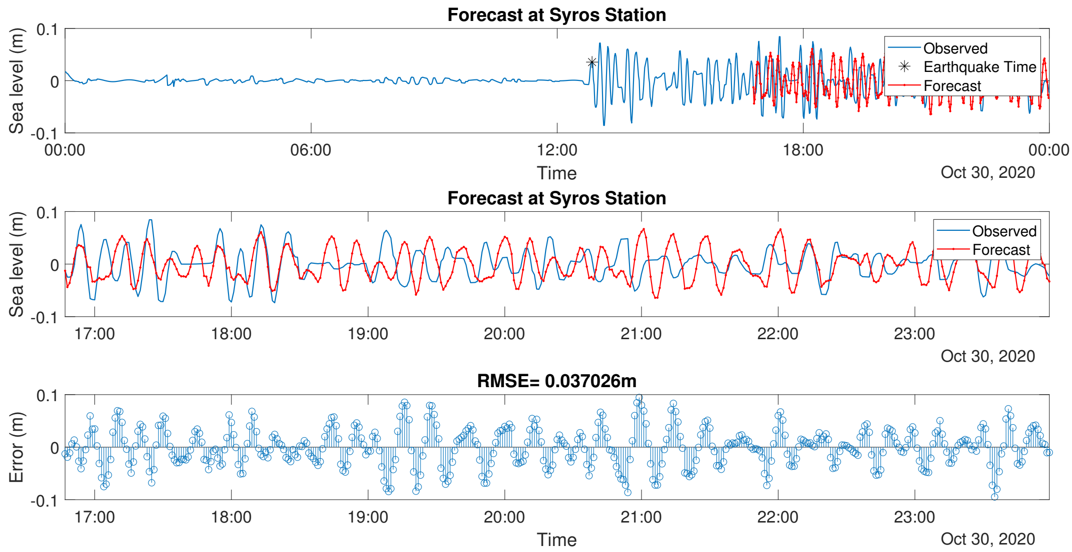

Figure 4.7 : Time series of the İzmir-Samos tsunami water surface fluctuation recorded at Syros station [114] on 30 October 2020 and its prediction by LSTM DL network-without updates.

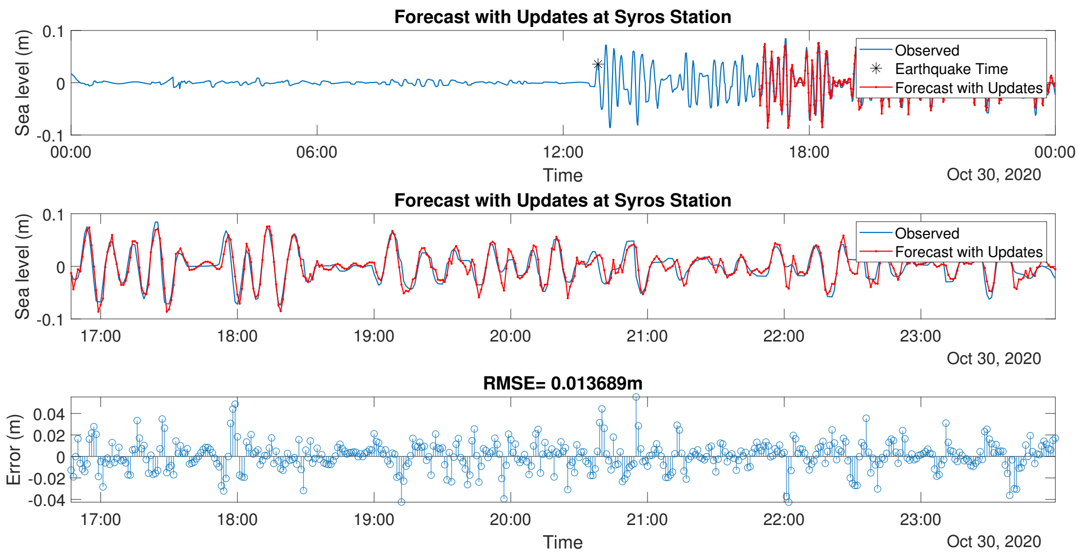

Figure 4.8 : Time series of the İzmir-Samos tsunami water surface fluctuation recorded at Syros station [114] on 30 October 2020 and its prediction by LSTM DL network-with updates.

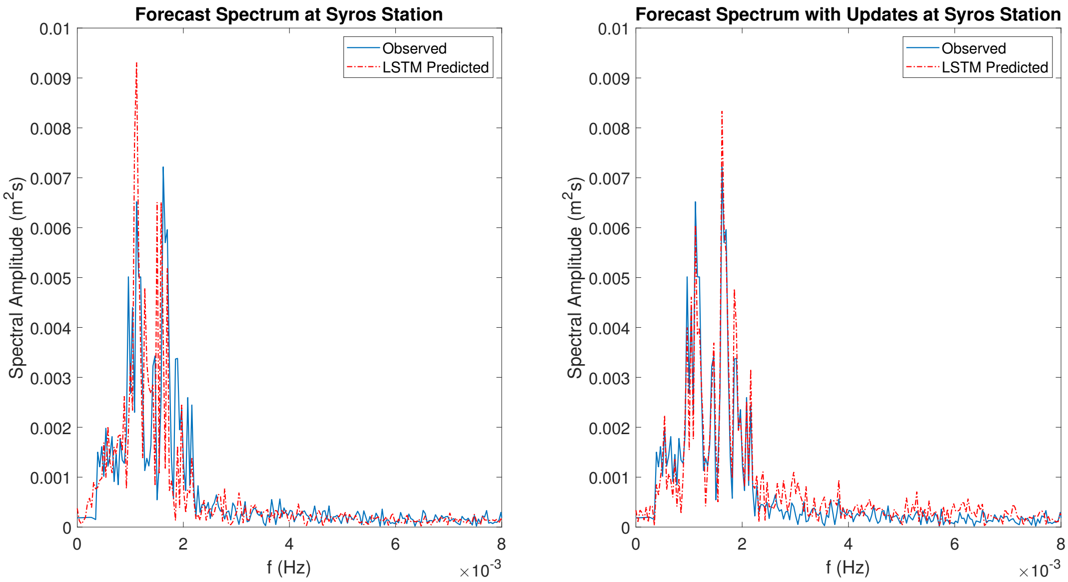

Figure 4.9 : Comparison of Fourier spectra of time series predictions performed by LSTM DL network at Syros station on 30 October 2020 (**left**) without updates (**right**) with updates.

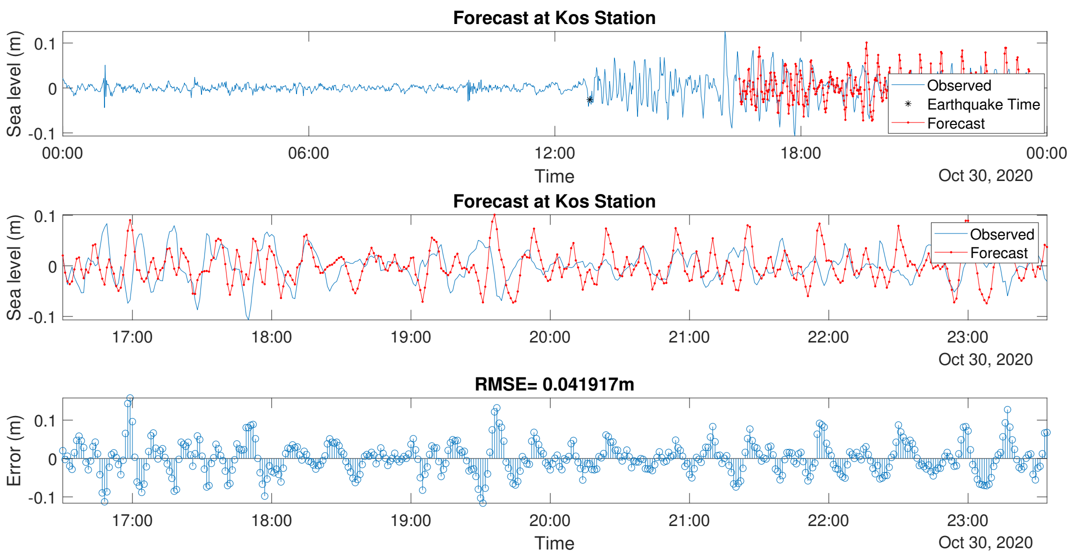

Figure 4.10 : Time series of the İzmir-Samos tsunami water surface fluctuation recorded at Kos station [114] on 30 October 2020 and its prediction by LSTM DL network-without updates.

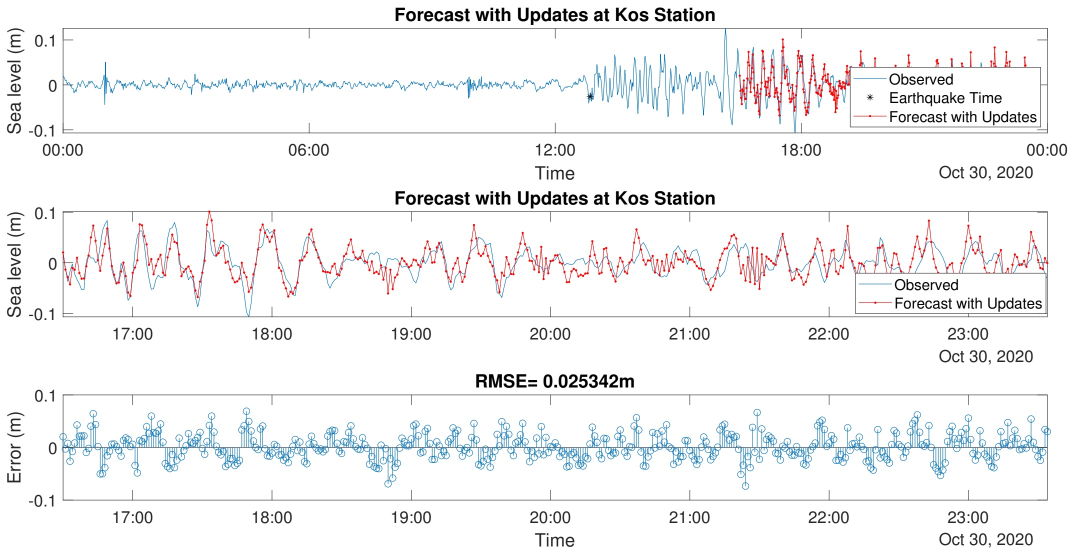

Figure 4.11 : Time series of the İzmir-Samos tsunami water surface fluctuation recorded at Kos station [114] on 30 October 2020 and its prediction by LSTM DL network-with updates.

The similar prediction analysis for the tsunami time series recorded at Kos station located at [latitude: 36.898362, longitude: 27.287792] is repeated the results obtained using the LSTM network with no updates are depicted in Fig. 4.11. The maximum tsunami wave height in this time series was recorded to be around 20 cm which remains in the training data part, for the predicted part it is around 16 cm as time series depicted in Fig. 4.11 and one-sided (half-amplitude) Fourier spectra depicted in Fig. 4.12 confirms. The highest RMSE among all data sets is depicted in Fig. 4.11, mainly due to phase mismatch between actual recordings and predictions. It can be observed that the spectral features of the Kos station time series differ from their counterparts analyzed before. Some of the reasons for this fact are the recordings are carried out by radar which is more sensitive compared to pressure gauge, as well as tsunami asymptotics can change with barriers and distance [88].

It is again useful to observe that LSTM with updates leads to spectral amplitude mismatch at higher wavenumbers; however, it predicts the lower frequency components with higher amplitudes better, as before. This can lead to the development of filtered LSTM networks for the removal and isolation of such components.

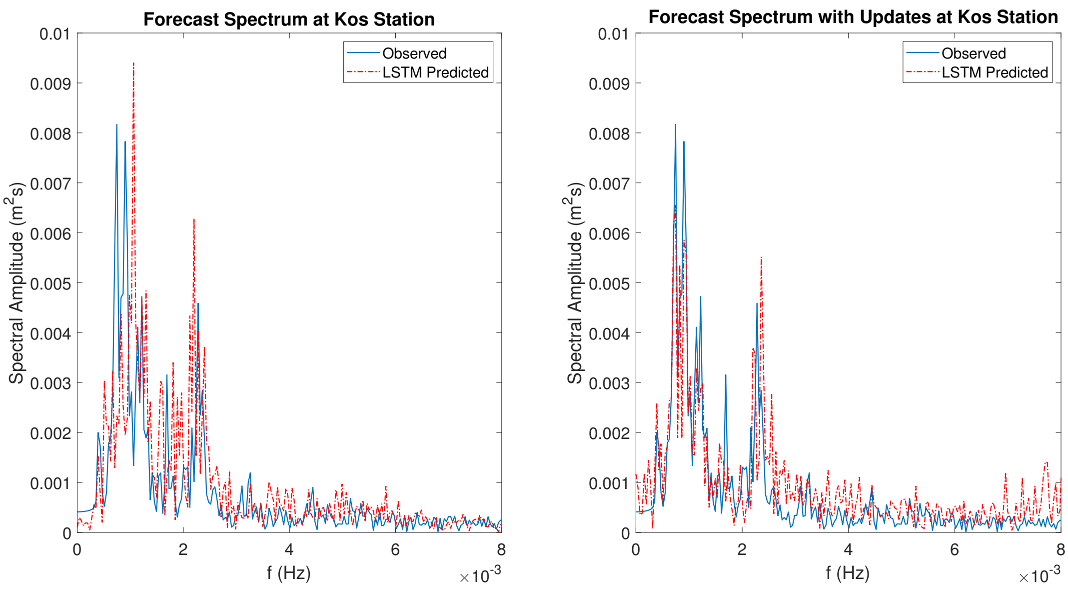

Figure 4.12 : Comparison of Fourier spectra of time series predictions performed by LSTM DL network at Kos Station on 30 October 2020 (**left**) without updates (**right**) with updates.

The last data set analyzed is recorded at the Kos Marina station located at [latitude: 36.891013, longitude: 27.303632] which is very close to the Kos station mentioned above. Similarly, the maximum tsunami wave height in this time series was recorded to be around 20 cm which remains in the training data part, for the predicted part it is around 14 cm as the time series depicted in Figure and one-sided (half-amplitude) Fourier spectra depicted in Figure confirms. The highest RMSE among all data sets is depicted in Fig. 4.11, mainly due to phase mismatch between actual recordings and predictions. The characteristics of the time series are more similar to the time series recorded at the Kos station discussed above.

Figs. 4.13–4.15 confirm that prediction by the LSTM network with no updates is better compared to the case of Kos station, however, a similar high wavenumber spectral amplitude mismatch pattern can still be observed. Again, such features may be suppressed by using spectral filters to allow for specific bandwidth of predictions.

Lastly, we turn our attention to the analysis of the effect of the length of the training data set on prediction results. For all the simulations reported above, we use 70% of the daily tsunami time series to predict the remaining 30%. The training data

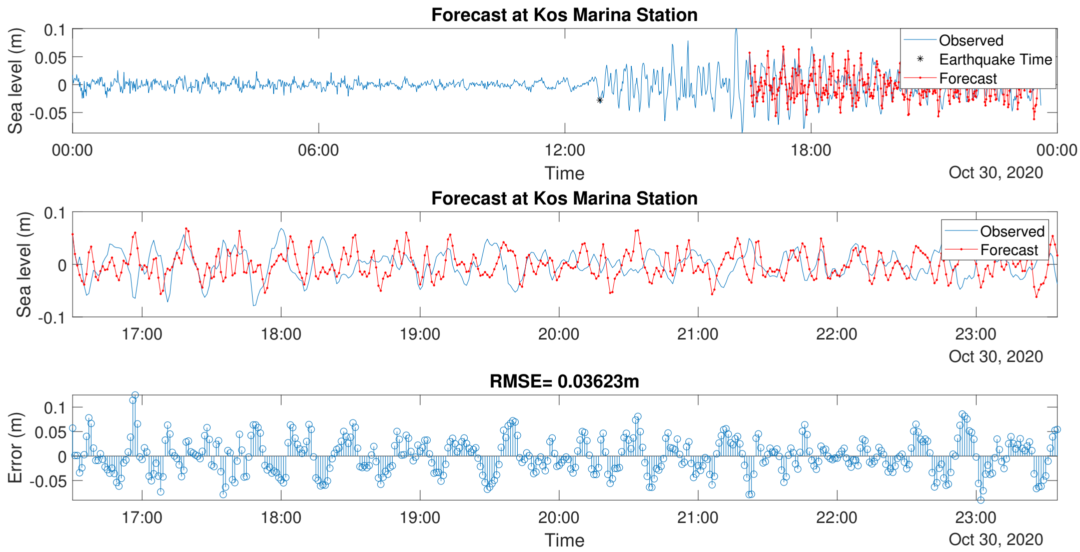

Figure 4.13 : Time series of the İzmir-Samos tsunami water surface fluctuation recorded at Kos Marina station [114] on 30 October 2020 and its prediction by LSTM DL network-without updates.

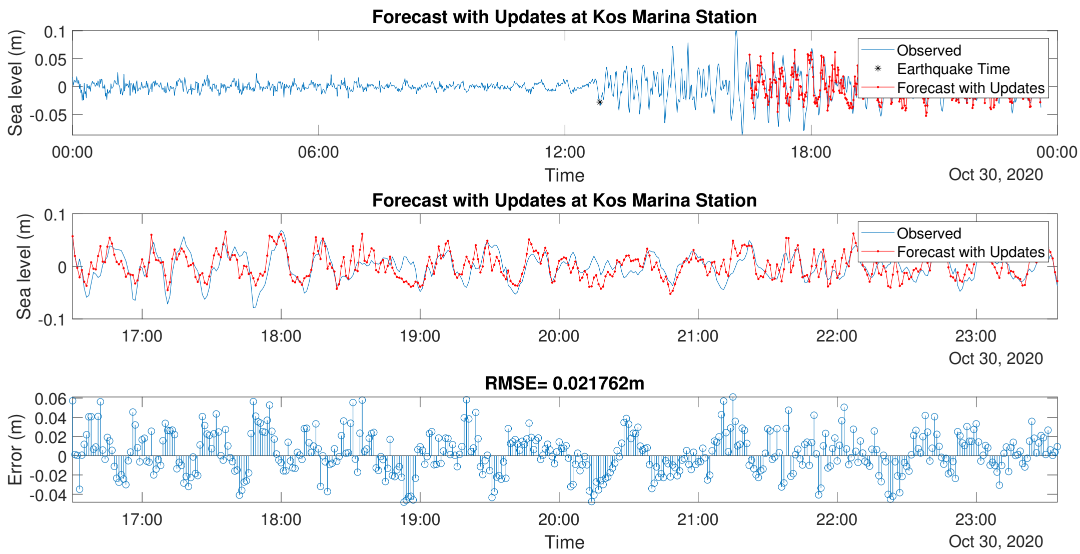

Figure 4.14 : Time series of the İzmir-Samos tsunami water surface fluctuation recorded at Kos Marina station [114] on 30 October 2020 and its prediction by LSTM DL network-with updates.

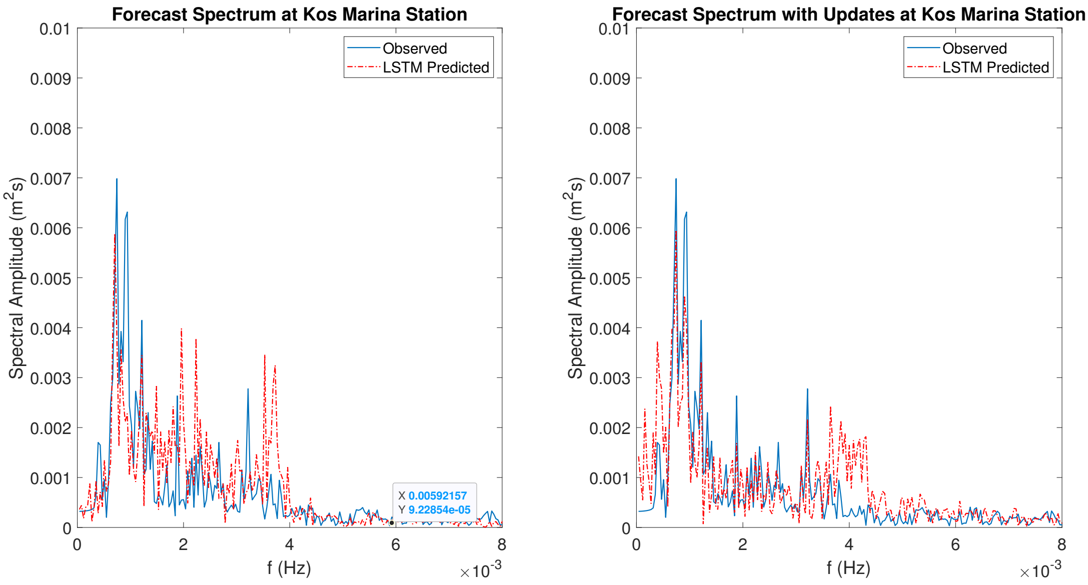

Figure 4.15 : Comparison of Fourier spectra of time series predictions performed by LSTM DL network at Kos Marina Station on 30 October 2020 (**left**) without updates (**right**) with updates.

set includes both the pre-earthquake and post-earthquake recordings. Now, as an illustrative example we set the length of the training data set to be 85% of the daily tsunami time series recorded at the Kos Marina, thus re-perform the last analysis with these values.

Checking Figs. 4.16–4.18 and comparing them with Figs. 4.13–4.15, one can realize that increasing the length of training data has a significant effect on reducing RMSE error and phase mismatch, however, in our simulations, we observe that although this is generally the case, there is not always a monotonic relation. Thus, the training data set must be selected with care. Additionally, by comparing the Fourier spectra of the last two analyses, one can realize that spectral amplitude mismatch between observations and predictions at higher wavenumbers is unlikely to be reduced by increasing the length of the training data set. Thus, a filtering approach may be developed.

The results of our paper are promising to enhance the predictions of tsunami events and hydrodynamics. Even when the LSTM network with updates is used, although the predictions are valid for a one-time step, the time steps investigated in this paper are either 0.5 min or 1 min. Such time scales can be quite beneficial to save lives and

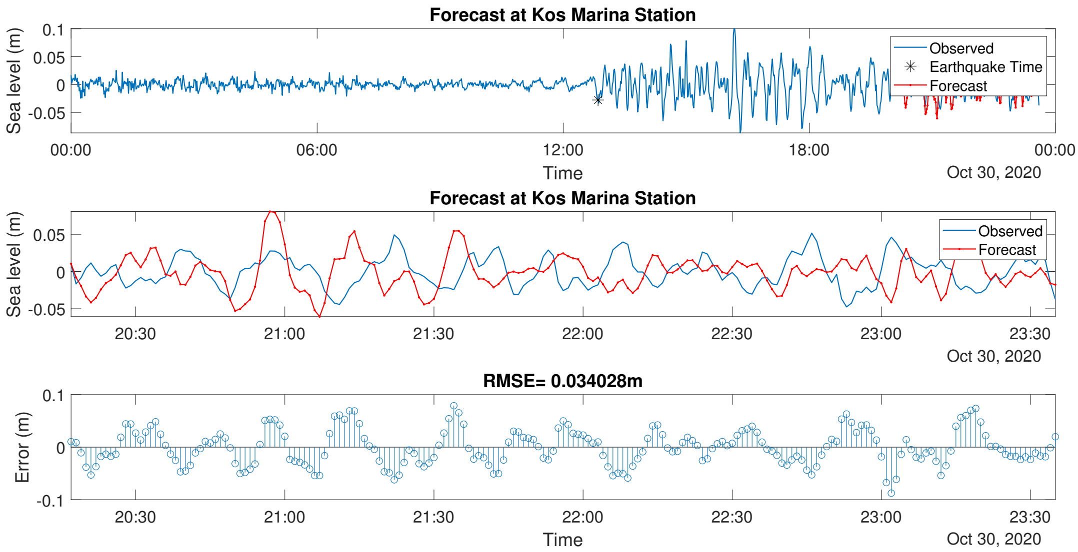

Figure 4.16 : Time series of the İzmir-Samos tsunami water surface fluctuation recorded at Kos Marina station [114] on 30 October 2020 and its prediction by LSTM DL network using 85% training data-without updates.

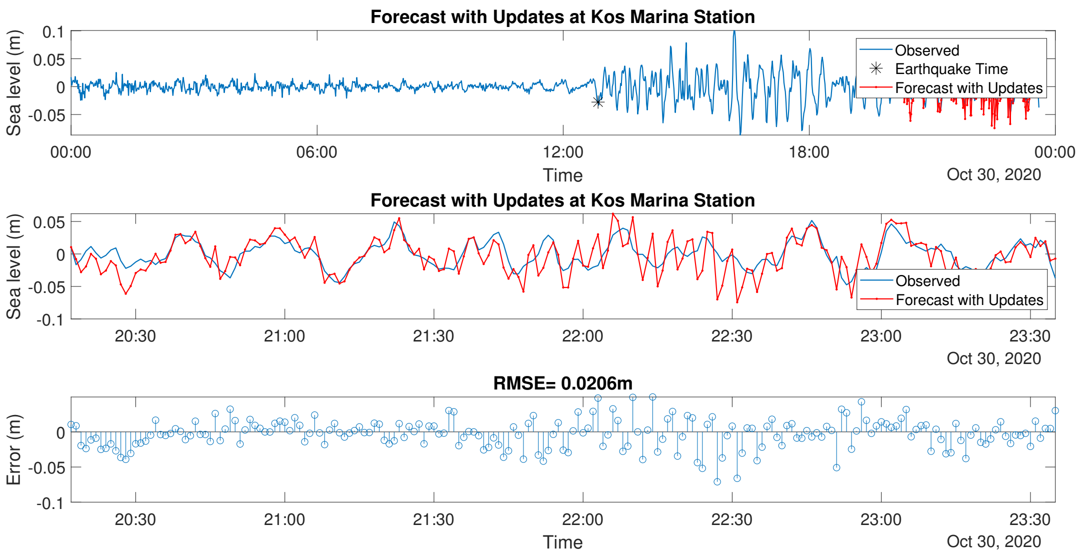

Figure 4.17 : Time series of the İzmir-Samos tsunami water surface fluctuation recorded at Kos Marina station [114] on 30 October 2020 and its prediction by LSTM DL network using 85% training data-with updates.

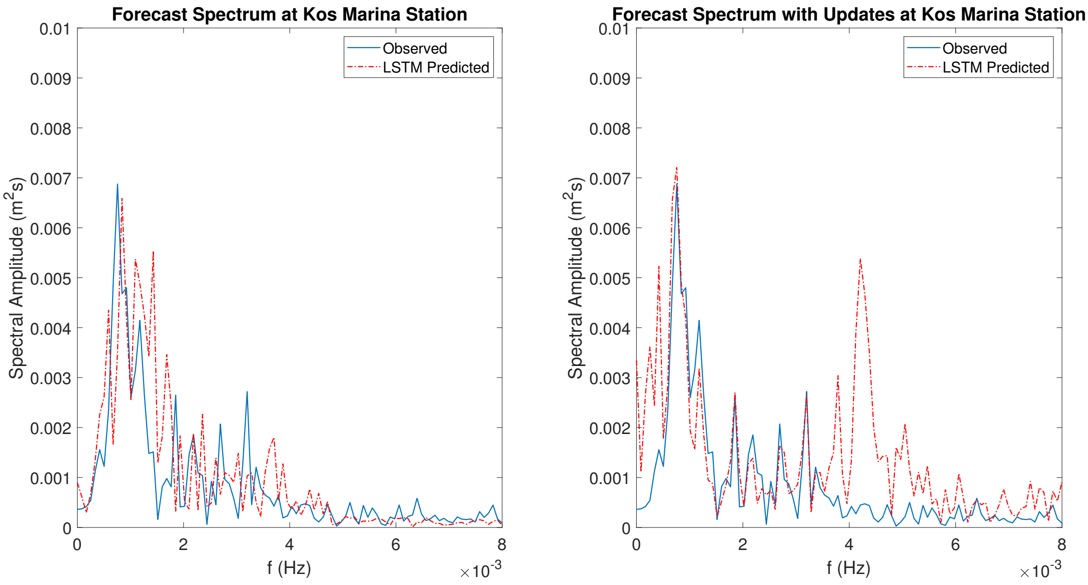

Figure 4.18 : Comparison of Fourier spectra of time series predictions performed by LSTM DL network using 85% training data at Kos Marina Station on 30 October 2020 (**left**) without updates (**right**) with updates.

avoiding damage and loss by more precise mapping of possible tsunami inundation and run-up time series, which exhibit nonlinear features that can be modeled using nonlinear equations such as those in [88,117]. Besides this, there are many different tsunami early warning systems [118]. The majority of these systems rely on techniques such as measuring and estimating the tsunamigenic potential of an earthquake using seismic data, or detection of Tsunami Waves using Sea-level Networks after a tsunami occurs in deep water. Bottom pressure recorders, coastal tide-gauge stations, current meters, buoys, or radars are used for the latter systems [118]. According to the National Oceanic and Atmospheric Administration (NOAA), the early warning time scale for tsunamis ranges from five minutes to two hours, depending on the distance between its source and the nearest Deep-ocean Assessment and Reporting of Tsunami (DART) system or coastal water-level station. Such time scales can be significantly developed (same order of magnitude) using the proposed methodology in this paper, which depends on LSTM or similar DL networks. Also, not only the early warning time scales would be enhanced using our findings, but also more accurate predictions of tsunami hydrodynamic parameters such as water surface level, run-up, or run-up volume can be made [119,120].

5. CONCLUSION

This thesis study involved the derivation of analytical solutions for non-breaking long waves on geometries exhibiting both linear and nonlinear fluctuations in breadth and depth, in the presence of a solid vertical (Chapter 2), and inclined (Chapter 3) wall. In Chapter 2 within the frame of Publication Number 1, and in Chapter 3 within the frame of Publication Number 2, we took power-law nonlinearities into consideration for the modifications of the nonlinear geometries. We demonstrated that Bessel-Z functions and Cauchy-Euler series are the forms in which the solutions for such profiles take. The singular points are shed from the boundary because of the vertical or inclined wall that is present in the geometry. Consequently, the above-mentioned first kind and second kinds of special functions were included in the analytical solutions. After giving the analytical solutions for any geometry with the considered form, we went over various examples. We reviewed the features of the generated long wave solutions and illustrated their water surface fluctuations. Certain geometries can be utilized as resonators such as Wave Buoy and Wave Dragon to increase the amount of energy captured because they can have a major impact on the fluctuation of the water's surface. Our findings have potential applications in reconstruction, sedimentation, and dredging hydrodynamics since they may be utilized to examine long wave and harbor dynamics, tsunamis, and the impact of building and removing vertical and inclined solid walls on those dynamics. They can also be used to determine the general characteristics of wave resonators and sound sources.

We intend to investigate related phenomena not only in 1D but also in 2D using the Laguerre polynomials that were covered in [13,19]. The development of similar solitary wave studies [121] and tsunami runup calculations, like the one covered by [122], may also be carried out for the geometries taken into consideration in this thesis study, involving the impact of solid vertical and inclined walls. Our method can be used to obtain the solutions of the long wave equation for additional geometries with different shapes, such as a vertical or inclined wall, in terms of Laguerre, Chebyshev, Hermite, or Legendre polynomials [123]–[125]. The effect of current can also be included in our findings when applying them to nonlinear waves like those covered by [121,126]–[129]. For some geometries, this may require numerical treatment of the fully nonlinear equations using methods like those by [130] and [131]. Additionally, if the type of wall used is changed, our work may become a new research topic. For example, by using porous walls or elastic walls, the work we have done within the scope of this thesis can be repeated and compared with previous examples.

In Chapter 4 within the frame of Publication Number 3, we have examined the LSTM deep learning network's potential use in forecasting tsunami hydrodynamics. To do this, we assessed the 30 October 2020 İzmir-Samos Tsunami's daily water surface fluctuation time series data, which was obtained at many UNESCO stations. We proved that, with or without updates, it is feasible to utilize LSTM to successfully predict such a time series. We revealed that the LSTM with updates is more successful and consistent in prediction, even if using an LSTM network without updates alone generated good results, particularly for the Bodrum station. In the case of no updates, the prediction time scale is on the order of a few hours. Nonetheless, when an updated network is utilized, the prediction time scale of the post-event accurate hydrodynamics is limited to one time step, which is either 0.5 min or 1 min for the data examined in this thesis. Additionally, we shared information about the spectral aspects of the predictions, which demonstrate that the LSTM network can reasonably forecast the tsunami time series spectrum, despite some mismatch visible at higher frequencies.

This thesis has the potential to improve tsunami early warning times by minutes to hours, based on the event's location and magnitude. When an occurrence is recognized at an offshore site, this capability would be quite useful. By predicting secondary waves and tsunami asymptotics at offshore stations after the event is recorded, the early warning system for coastal zones can be improved, and a more precise mapping of the inundation at the shoreline can be carried out. Furthermore, run-up time series and horizontal and excursion velocities—parameters associated with tsunamis—can be predicted with ease using our data. We intend to apply our results to compressive sensing of nonlinear processes and other DL networks, as well as time series prediction tools [132,133], soon. Furthermore, the DL and other AI techniques will be utilized to investigate tsunami run-up, inundation characteristics, damage prediction, and the determination of seismic behavior using tsunami data. Other observational data or analytical/numerical approaches, like the one covered in [134], can be used in conjunction with these techniques.

To improve our work in the future, we aim to represent the runup of the 30 October 2020 İzmir-Samos Tsunami on nonlinear profiles. To do this, we will develop a tsunami model code for nonlinear profiles in MATLAB. Then we will convert our tsunami data which are in the time domain to the space domain. Finally, after the application of this converted data to our code, we will obtain the 30 October 2020 İzmir-Samos Tsunami's runup characteristics for nonlinear geometries.

REFERENCES

[1] **Lamb, H.** (1945). *Hydrodynamics*, sixth ed. Dover Publications, UK, (First Edition 1879).

[2] **Chrystal, G.** (1905). *On the hydrodynamical theory of seiches with a bibliographical sketch*, Trans. Roy. Soc. Edinburg.

[3] **Wilson, B.W.**, (1972). Seiches, Advances in hydroscience, volume 8, Elsevier, pp.1–94.

[4] **Goldsbrough, G.R.** (1936). The tidal oscillation in an elliptic basin of variable depth-II, *Proceedings of the Royal Society of London. Series A-Mathematical and Physical Sciences*, *155*(884), 12–32.

[5] **Dean, R.G. and Dalrymple, R.A.** (1991). *Water wave mechanics for engineers and scientists*, volume 2, world scientific publishing company.

[6] **Mei, C.C.**, **Stiassnie, M.A. and Yue, D.K.P.** (2005). *Theory and applications of ocean surface waves: Part 1: linear aspects*, World Scientific.

[7] **Munk, W.** (1949). Surf beats, *EOS, Transactions American Geophysical Union*, *30*(6), 849–854.

[8] **Lettau, H.** (1932). Stehende Wellen als Ursache und gestaltender Vorgange in Seen, *Annalen der Hydrographie und maritimen Meteorologie*, *60*, 385–388.

[9] **Bowen, A.** (1975). On-offshore sand transport on a beach, *Transactions-American Geophysical Union*, volume 56, American Geophysical Union 2000 Florida Avenue Nw, Washington, DC 20009, pp.83–83.

[10] **Longuet-Higgins, M.S. and Stewart, R.** (1962). Radiation stress and mass transport in gravity waves, with application to ‘surf beats’, *Journal of Fluid Mechanics*, *13*(4), 481–504.

[11] **Suhayda, J.N.** (1974). Standing waves on beaches, *Journal of Geophysical Research*, *79*(21), 3065–3071.

[12] **Smith, R. and Sprinks, T.** (1975). Scattering of surface waves by a conical island, *Journal of Fluid Mechanics*, *72*(2), 373–384.

[13] **Kirby Jr, J.T.**, **Dalrymple, R.A. and Liu, P.L.F.** (1981). Modification of edge waves by barred-beach topography, *Coastal Engineering*, *5*, 35–49.

[14] **Eckart, C.** (1951). Surface waves on water of variable depth, *Wave Report Number 100, SIO Reference 51-12*.

[15] **Ball, F.** (1967). Edge waves in an ocean of finite depth, *Deep Sea Research and Oceanographic Abstracts*, volume 14, Elsevier, pp.79–88.

[16] **Noda, H.**, (1968). A study on mass transport in boundary layers in standing waves, Coastal Engineering 1968, pp.227–247.

[17] **Gallagher, B.** (1971). Generation of surf beat by non-linear wave interactions, *Journal of Fluid Mechanics*, *49*(1), 1–20.

[18] **Summerfield, W.** (1972). Circular islands as resonators of long-wave energy, *Philosophical Transactions of the Royal Society of London. Series A, Mathematical and Physical Sciences*, *272*(1225), 361–402.

[19] **Ursell, F.** (1952). Edge waves on a sloping beach, *Proceedings of the royal society of London. Series A. Mathematical and Physical Sciences*, *214*(1116), 79–97.

[20] **Bowen, A.J. and Guza, R.T.** (1978). Edge waves and surf beat, *Journal of Geophysical Research: Oceans*, *83*(C4), 1913–1920.

[21] **Stokes, G.G.** (1846). Report on recent researches in hydrodynamics, *Reports of the British Association*, *1*(1), 20.

[22] **Huntley, D.** (1976). Long-period waves on a natural beach, *Journal of Geophysical Research*, *81*(36), 6441–6449.

[23] **Holman, R. and Bowen, A.** (1979). Edge waves on complex beach profiles, *Journal of Geophysical Research: Oceans*, *84*(C10), 6339–6346.

[24] **Guza, R.T. and Inman, D.L.** (1975). Edge waves and beach cusps, *Journal of Geophysical Research*, *80*(21), 2997–3012.

[25] **Auld, B.** (1973). *Acoustic Fields and Waves in Solids*, Krieger Publishing Company.

[26] **Lakin, K.M.**, **Kline, G.R. and McCarron, K.T.** (1993). High-Q microwave acoustic resonators and filters, *IEEE transactions on microwave theory and techniques*, *41*(12), 2139–2146.

[27] **Li, X.**, **Finkbeiner, J.**, **Raman, G.**, **Steinetz, B.M.** *et al.* (2004). Optimized shapes of oscillating resonators for generating high-amplitude pressure waves, *The Journal of the Acoustical Society of America*, *116*(5), 2814–2821.

[28] **Chevalier, P.**, **Bouchon, P.**, **Haïdar, R. and Pardo, F.** (2014). Optical helmholtz resonators, *Applied Physics Letters*, *105*(7), 071110.

[29] **Liu, P.L.F.**, **Lynett, P. and Synolakis, C.E.** (2003). Analytical solutions for forced long waves on a sloping beach, *Journal of Fluid Mechanics*, *478*, 101–109.

[30] **Madsen, O.S. and White, S.M.** (1975). *Reflection and transmission characteristics of porous rubble mound breakwaters*, 76, Department of Civil Engineering, Massachusetts Institute of Technology.

[31] **Pelinovsky, E. and Mazova, R.K.** (1992). Exact analytical solutions of nonlinear problems of tsunami wave run-up on slopes with different profiles, *Natural Hazards*, *6*, 227–249.

[32] **Carrier, G.F. and Greenspan, H.P.** (1958). Water waves of finite amplitude on a sloping beach, *Journal of Fluid Mechanics*, *4*(1), 97–109.

[33] **Forsyth, A.R.** (1959). *Theory of differential equations*, CUP Archive.

[34] **Whittaker, E.** (1902a). On periodic orbits, *Monthly Notices of the Royal Astronomical Society*, *62*, 186–193.

[35] **Whittaker, E.** (1902b). *A Course of Modern Analysis*, Cambridge Univ. Press.

[36] **Thomson, W. and Tait, P.G.** (2022). *Treatise on natural philosophy*, CUP Archive.

[37] **marquis de Laplace, P.S.** (1825). *Traité de mécanique céleste*, volume 5, Chez JBM Duprat, libraire pour les mathématiques, quai des Augustins.

[38] **Jacobi, C.G.J.** (1891). *CGJ Jacobi's gesammelte Werke*, volume 6, G. Reimer.

[39] **Poisson, S.D.** (1831). *Nouvelle théorie de l'action capillaire*, Courcier.

[40] **Neumann, C.** (1862). *Ueber die Entwickelung einer Function mit imaginärem Argument nach den Kugelfunctionen erster und zweiter Art*.

[41] **Watson, G.N.** (1922). *A treatise on the theory of Bessel functions*, volume 2, The University Press.

[42] **Wilson, B.** (1966). The Encyclopedia of Oceanography, edited by RW Fairbridge, Academic Press, New York, pp.804–817.

[43] **Berkhoff, J.**, (1972). Computation of combined refraction—diffraction, Coastal Engineering 1972, pp.471–490.

[44] **marquis de Laplace, P.S.** (1823). *Traité de mécanique céleste, 1*, Typ. Crapelet.

[45] **Gauss, C.F.** (1870). *Disquisitiones arithmeticae*, volume 1, K. Gesellschaft der Wissenschaften zu Göttingen.

[46] **Bayındır, C. and Farazande, S.** (2021). The solution of the long-wave equation for various nonlinear depth and breadth profiles in the power-law form, *Dynamics of Atmospheres and Oceans*, *96*, 101254.

[47] **Greenberg, M.D.** (1998). *Advanced engineering mathematics*, Pearson Education India.

[48] **Dean, R.G.** (1991). Equilibrium beach profiles: characteristics and applications, *Journal of Coastal Research*, *7*(1), 53–84.

[49] **Okazaki, S.i. and Sunamura, T.** (1991). Re-examination of breaker-type classification on uniformly inclined laboratory beaches, *Journal of Coastal Research*, 559–564.

[50] **Iribarren, R.** (1965). Fórmula para el cálculo de los diques de escolleras naturales o artificiales, *Revista de Obras Públicas*, *113*, 829–849.

[51] **Alcérreca-Huerta, J.C.** (2014). *Process-based modelling of waves interacting with porous bonded revetments and their sand foundation*, Dissertation, Braunschweig, Technische Universität Braunschweig.

[52] **Battjes, J.A.**, (1974). Surf similarity, Coastal Engineering 1974, pp.466–480.

[53] **Bruun, P. and Johannesson, P.** (1974). A critical review of the hydraulics of rubble mound structures, *Institute report R3*.

[54] **Iversen, H.W.** (1952). Laboratory study of breakers, *Gravity Waves, Circular*, *52*, 9–32.

[55] **Galvin Jr, C.J.** (1968). Breaker type classification on three laboratory beaches, *Journal of geophysical research*, *73*(12), 3651–3659.

[56] **Sunamura, T. and Horikawa, K.** (1988). Nearshore Dynamics and Coastal Processes.

[57] **Svendsen, I.A.** (2005). *Introduction to nearshore hydrodynamics*, volume 24, World Scientific Publishing Company.

[58] **Sabatier, F.** (2007). US Army Corps of Engineers, Coastal Engineering Manual (CEM), Engineer Manual 1110-2-1100. US Army Corps of Engineers, Washington, DC (6 volumes)., *Méditerranée. Revue géographique des pays méditerranéens/Journal of Mediterranean geography*, (108), 146.

[59] **Pullen, T.**, **Allsop, N.**, **Bruce, T.**, **Kortenhaus, A.**, **Schüttrumpf, H. and Van der Meer, J.** (2007). EurOtop, European overtopping manual-wave overtopping of sea defences and related structures: assessment manual, *Also published as special volume of Die Küste*.

[60] **Camenen, B. and Larson, M.** (2007). Predictive formulas for breaker depth index and breaker type, *Journal of Coastal Research*, *23*(4), 1028–1041.

[61] **Goda, Y.**, (2010). Random wave breaking and nonlinearity evolution across the surf zone, Handbook Of Coastal And Ocean Engineering, World Scientific, pp.87–113.

[62] **McCowan, J.** (1894). XXXIX. On the highest wave of permanent type, *The London, Edinburgh, and Dublin Philosophical Magazine and Journal of Science*, *38*(233), 351–358.

[63] **Yamada, H.** (1968). Precise determination of the solitary waves of extreme height on water of a uniform depth, *Reports of Research Institute for Applied Mechanics, Kyushu University*, (52), 15–32.

[64] **Miche, M.** (1944). Mouvements ondulatoires de la mer en profondeur constante ou décroissante, *Annales de Ponts et Chaussées, 1944, pp (1) 26-78,(2) 270-292,(3) 369-406*.

[65] **Battjes, J.** (1978). Energy loss and set-up due to breaking wave, *Proceedings of the 16th International Conference on Coastal Engineering, 1978*, volume 1, pp.596–587.

[66] **Collins, J.I. and Wier, W.** (1969). *Probabilities of wave characteristics in the surf zone*, Tetra Tech, Incorporated.

[67] **Galvin Jr, C.J.** (1969). Breaker travel and choice of design wave height, *Journal of the Waterways and Harbors Division*, *95*(2), 175–200.

[68] **Kishi, T. and Saeki, H.**, (1967). The shoaling, breaking and runup of the solitary wave on impermeable rough slopes, Coastal Engineering 1966, pp.322–348.

[69] **Rattanapitikon, W. and Vivattanasirisak, T.** (2002). Comparison of breaker height formulas using large-scale wave tanks, *Journal of Science and Technology*, *24*(4), 663–674.

[70] **Ostendorf, D.W. and Madsen, O.S.** (1979). An analysis of longshore currents and associated sediment transport in the surf zone.

[71] **Larson, M.**, **Kraus, N.C. and of the army. US Army corps of engineers, D.** (1989). SBEACH: Numerical model for simulating storm-induced beach change. Report 1, Empirical foundation and model development.

[72] **Gourlay, M.R.** (1978). Wave-generated currents (Ph. D. Thesis), *Department of Civil Engineering, University of Queensland*.

[73] **Goda, Y.** (1970). A synthesis of breaker indices, *Proceedings of the Japan society of civil engineers*, volume1970, Japan Society of Civil Engineers, pp.39–49.

[74] **Rattanapitikon, W. and Shibayama, T.** (2000). Verification and modification of breaker height formulas, *Coastal engineering journal*, *42*(04), 389–406.

[75] **Kamphuis, J.** (1991). Incipient wave breaking, *Coastal Engineering*, *15*(3), 185–203.

[76] **Miche, M.** (1951). Le pouvoir réfléchissant des ouvrages maritimes exposés à l'action de la houle, *Annales de Ponts et Chaussées, 121 (285-319)*.

[77] **Seelig, W.N. and Ahrens, J.P.** (1981). Estimation of wave reflection and energy dissipation coefficients for beaches, revetments, and breakwaters.

[78] **Losada, M.A. and Giménez-Curto, L.A.** (1980). Flow characteristics on rough, permeable slopes under wave action, *Coastal Engineering*, *4*(0), 187–206.

[79] **Postma, G.** (1989). Wave reflection from rock slopes under random wave attack, *MS thesis, Delft University of Technology, Department of Civil Engingineering*.

[80] **Van der Meer, J.** (1988). Rock slopes and gravel beaches under wave attack (Ph. D. Thesis), *Delft University of Technology, Delft*.

[81] **Davidson, M.**, **Bird, P.**, **Bullock, G. and Huntley, D.** (1996). A new non-dimensional number for the analysis of wave reflection from rubble mound breakwaters, *Coastal Engineering*, *28*(1-4), 93–120.

[82] **Zanuttigh, B. and Van der Meer, J.W.**, (2007). Wave reflection from coastal structures, Coastal Engineering 2006: (In 5 Volumes), World Scientific, pp.4337–4349.

[83] **Hughes, S.A. and Fowler, J.E.** (1995). Estimating wave-induced kinematics at sloping structures, *Journal of waterway, port, coastal, and ocean engineering*, *121*(4), 209–215.

[84] **Sutherland, J. and O'Donoghue, T.** (1998). Characteristics of wave reflection spectra, *Journal of waterway, port, coastal, and ocean engineering*, *124*(6), 303–311.

[85] **Sutherland, J. and O'Donoghue, T.** (1998). Wave phase shift at coastal structures, *Journal of waterway, port, coastal, and ocean engineering*, *124*(2), 90–98.

[86] **Ward, S.N.** (2001). Tsunamis, *Encyclopedia of physical science and technology*, *17*, 175–191.

[87] **Chapman, C.** (2005). The Asian tsunami in Sri Lanka: A personal experience, *EOS, Transactions American Geophysical Union*, *86*(2), 13–14.

[88] **Berry, M.V.** (2005). Tsunami asymptotics, *New Journal of Physics*, *7*(1), 129.

[89] **Röbke, B. and Vött, A.** (2017). The tsunami phenomenon, *Progress in Oceanography*, *159*, 296–322.

[90] **Ishihara, M. and Tadono, T.** (2017). Land cover changes induced by the great east Japan earthquake in 2011, *Scientific Reports*, *7*(1), 45769.

[91] **Kaiser, G.**, **Burkhard, B.**, **Römer, H.**, **Sangkaew, S.**, **Graterol, R.**, **Haitook, T.**, **Sterr, H. and Sakuna-Schwartz, D.** (2013). Mapping tsunami impacts on land cover and related ecosystem service supply in Phang Nga, Thailand, *Natural Hazards and Earth System Sciences*, *13*(12), 3095–3111.

[92] **Richmond, B.**, **Szczuciński, W.**, **Chagué-Goff, C.**, **Goto, K.**, **Sugawara, D.**, **Witter, R.**, **Tappin, D.R.**, **Jaffe, B.**, **Fujino, S.**, **Nishimura, Y.** *et al.* (2012). Erosion, deposition and landscape change on the Sendai coastal

plain, Japan, resulting from the March 11, 2011 Tohoku-oki tsunami, *Sedimentary Geology*, *282*, 27–39.

[93] **Tappin, D.R.**, **Evans, H.M.**, **Jordan, C.J.**, **Richmond, B.**, **Sugawara, D. and Goto, K.** (2012). Coastal changes in the Sendai area from the impact of the 2011 Tōhoku-oki tsunami: Interpretations of time series satellite images, helicopter-borne video footage and field observations, *Sedimentary Geology*, *282*, 151–174.

[94] **Bayındır, C.** Analysis of tsunami and tsunami-structure interaction parameters by compressive sensing, *ICAME'21*, 25.

[95] **Sambah, A.B. and Miura, F.** (2013). Remote sensing, GIS, and AHP for assessing physical vulnerability to tsunami hazard, *International Journal of Environmental and Ecological Engineering*, *7*(10), 671–679.

[96] **Yamazaki, F. and Matsuoka, M.** (2007). Remote sensing technologies in post-disaster damage assessment, *Journal of Earthquake and Tsunami*, *1*(03), 193–210.

[97] **Dogan, G.G.**, **Yalciner, A.C.**, **Yuksel, Y.**, **Ulutas, E.**, **Polat, O.**, **Guler, I.**, **Sahin, C.**, **Tarih, A. and Kanoglu, U.** (2021). The 30 October 2020 Aegean Sea Tsunami: Post-Event Field Survey Along Turkish Coast, *Pure and Applied Geophysics*, *178*, 785–812.

[98] **Triantafyllou, I.**, **Gogou, M.**, **Mavroulis, S.**, **Lekkas, E. and Papadopoulos, G.A.and Thravalos, M.** (2021). The tsunami caused by the 30 October 2020 Samos (Aegean Sea) Mw7.0 earthquake: Hydrodynamic features, source properties and impact assessment from post-event field survey and video records, *Journal of Marine Science and Engineering*, *9*(68).

[99] **Evelpidou, N.**, **Karkani, A. and Kampolis, I.** (2020). Relative sea level changes and morphotectonic implications triggered by the Samos earthquake of 30th October 2020, *Journal of Marine Science and Engineering*, *9*(40).

[100] **Politis, D.**, **Potirakis, S.**, **Contoyiannis, Y.**, **Biswas, S.**, **Sasmal, S. and Hayakawa, M.** (2021). Statistical and criticality analysis of the lower ionosphere prior to the 30 October 2020 Samos (Greece) earthquake (M6.9), based on VLF electromagnetic propagation data as recorded by a new VLF/LF receiver installed in Athens (Greece), *Entropy*, *23*(676).

[101] **Mase, H.**, **Yasuda, T. and Mori, N.** (2011). Real-time prediction of tsunami magnitudes in Osaka Bay, Japan, using an artificial neural network, *Journal of Waterway, Port, Coastal, and Ocean engineering*, *137*(5), 263–268.

[102] **Mitra, R.**, **Naruse, H. and Abe, T.** (2020). Estimation of tsunami characteristics from deposits: Inverse modeling using a deep-learning neural network, *Journal of Geophysical Research: Earth Surface*, *125*(9).

[103] **Makinoshima, F.**, **Oishi, Y.**, **Yamazaki, T.**, **Furumura, T. and Imamura, F.** (2021). Early forecasting of tsunami inundation from tsunami and geodetic observation data with convolutional neural networks, *Nature communications*, *12*(2253).

[104] **Fauzi, A. and Mizutani, N.** (2020). Machine learning algorithms for real-time tsunami inundation forecasting: a case study in Nankai region, *Pure and Applied Geophysics*, *177*(3), 1437–1450.

[105] **Mulia, I.E.**, **Ueda, N.**, **Miyoshi, T.**, **Gusman, A.R. and Satake, K.** (2022). Machine learning-based tsunami inundation prediction derived from offshore observations, *Nature Communications*, *13*(5489).

[106] **Wang, Y.**, **Imai, K.**, **Miyashita, T.**, **Ariyoshi, K.**, **Takahashi, N. and Satake, K.** (2023). Coastal tsunami prediction in Tohoku region, Japan, based on S-net observations using artificial neural network, *Earth, Planets and Space*, *75*(1).

[107] **Xu, H. and Wu, H.** (2023). Accurate Tsunami Wave Prediction Using Long Short-term Memory Based Neural Networks, *Ocean Modelling*, *186*(102259).

[108] **Dharmawan, W.**, **Diana, M., T.B.**, **Astawa, I.M.**, **Rahardjo, S. and Nambo, H.** (2023). Tsunami tide prediction in shallow water using recurrent neural networks: model implementation in the Indonesia Tsunami Early Warning System, *Journal of Reliable Intelligent Environments*.

[109] **Geiß, C.**, **Maier, J.**, **So, E.**, **Schoepfer, E.**, **Harig, S.**, **Gomez Zapata, J.C. and Zhu, Y.** (2023). Anticipating a risky future: LSTM models for spatiotemporal extrapolation of population data in areas prone to earthquakes and tsunamis in Lima, Peru, *EGUsphere [preprint]*.

[110] **Kiratzi, A.**, **Papazachos, C.**, **Özacar, A.**, **Pinar, A.and Kkallas, C. and Sopaci, E.** (2022). Characteristics of the 2020 Samos earthquake (Aegean Sea) using seismic data, *Bulletin of Earthquake Engineering*, *20*(14), 7713–7735.

[111] **Sboras, S.**, **Lazos, I.**, **Bitharis, S.**, **Pikridas, C.**, **Galanakis, D.**, **Fotiou, A.**, **Chatzipetros, A. and Pavlides, S.** (2021). Source modelling and stress transfer scenarios of the October 30, 2020 Samos earthquake: seismotectonic implications, *Turkish Journal of Earth Sciences*, *30*(8), 699–717.

[112] **Ren, C.**, **Yue, H.**, **Cao, B.**, **Zhu, Y.**, **Wang, T.**, **An, C.**, **Ge, Z. and Li, Z.** (2022). Rupture process of the 2020 Mw = 6.9 Samos, Greece earthquake on a segmented fault system constrained from seismic, geodetic, and tsunami observations., *Tectonophysics*, *839*(229497).

[113] **KOERI** (2020). *Boğaziçi University Kandilli Observatory and Earthquake Research Institute, Regional Earthquake-Tsunami Monitoring and Evaluation Center 30 October 2020 Aegean Sea Earthquake Press Release*

, http://www.koeri.boun.edu.tr/sismo/2/wp-content/uploads/2020/10/20201030_izmir_V1.pdf, Accessed on October 10, 2023.

[114] **UNESCO/IOC** (2020). *UNESCO Intergovernmental Oceanographic Commission Sea Level Station Monitoring Facility*, https://www.ioc-sealevelmonitoring.org/station.php?code=stationcode, Accessed on October 10, 2023.

[115] **Hochreiter, S. and Schmidhuber, J.** (1997). Long short-term memory, *Neural computation*, *9*(8), 1735–1780.

[116] **Olah, C** (2015). *Understanding LSTM Networks*, https://colah.github.io/posts/2015-08-Understanding-LSTMs/, Accessed on October 10, 2023.

[117] **Bayındır, C.**, **Altintas, A.A. and Ozaydin, F.** (2021). Self-localized solitons of a q-deformed quantum system, *Communications in Nonlinear Science and Numerical Simulation*, *92*(105474), 1.

[118] **Srinivasa Kumar, T. and Manneela, S.** (2021). A review of the progress, challenges and future trends in tsunami early warning systems, *Journal of Geological Society of India*, *97*(100983), 1533–1544.

[119] **González, F.I.**, **Milburn, H.**, **Bernard, E. and Newman, J.** (2003). Deep-ocean assessment and reporting of tsunamis (DART): Brief overview and status report, **Technical Report**.

[120] **Meinig, C.**, **Eble, M.C. and Stalin, S.E.** (2001). System development and performance of the deep-ocean assessment and reporting of tsunamis (DART) system from 1997–2001, **Technical Report**.

[121] **Bayındır, C.** (2021). Self-localized solitons of the nonlinear wave blocking problem, *Dynamics of Atmospheres and Oceans*, *93*, 101189.

[122] **Synolakis, C.** (1987). The runup of solitary waves, *Journal of Fluid Mechanics*, *185*, 523–545.

[123] **Arfken, G.**, **Weber, H. and Harris, F.** (2011). *Mathematical Methods for Physicists: A Comprehensive Guide*, Academic press.

[124] **Whittaker, E. and Watson, G.** (1920). *A Course of Modern Analysis*, University Press.

[125] **Courant, R. and Hilbert, D.** (1989). *Methods of Mathematical Physics*, John Wiley and Sons.

[126] **Benney, D.J.** (1973). Some properties of long nonlinear waves, *Studies in Applied Mathematics*, *52*(1), 45–50.

[127] **Bayındır, C.**, **Altintas, A. and Ozaydin, F.** (2021). Self-localized solitons of a q-deformed quantum system, *Communications in Nonlinear Science and Numerical Simulation*, *92*, 105474.

[128] **Razzaq, W.**, **Zafar, A.**, **Ahmed, H.M. and Rabie, W.B.** (2022). Construction Solitons for Fractional Nonlinear SchröDinger Equation with -time Derivative by the New Sub-equation Method, *Journal of Ocean Engineering and Science*.

[129] **Ahmed, M.S.**, **Zaghrout, A.A.S. and Ahmed, H.M.** (2024). Travelling Wave Solutions for the Doubly Dispersive Equation Using Improved Modified Extended Tanh-function Method, *Alexandria Engineering Journal*, *61*(10).

[130] **Bayındır, C.** (2016). Compressive spectral method for the simulation of the nonlinear gravity waves, *Scientific Reports*, *6*(1), 22100.

[131] **Karjadi, E.**, **Badiey, M.**, **Kirby, J. and Bayındır, C.** (2011). The effects of surface gravity waves on high-frequency acoustic propagation in shallow water, *IEEE Journal of Oceanic Engineering*, *37*(1), 112–121.

[132] **Bayındır, C. and Namli, B.** (2021). Efficient sensing of Von Karman vortices using compressive sensing, *Computers Fluids*, *226*(104975), 1.

[133] **Bayındır, C.** (2018). Compressive spectral renormalization method, *TWMS Journal of Applied and Engineering Mathematics*, *8*(2), 425–437.

[134] **Bueler-Faudree, T.**, **Sam, D.**, **Dutykh, D.**, **Rybkin, A. and Suleimani, A.** (2021). Fast shallow water-wave solver for plane inclined beaches, *SoftwareX*, *17*(100983).

CURRICULUM VITAE

Name Surname: Ali Rıza ALAN

EDUCATION:

- **B.Sc.:** 2017, FMV Işık University, Faculty of Engineering, Department of Civil Engineering
- **M.Sc.:** 2020, FMV Işık University, Graduate School of Science and Engineering, Department of Civil Engineering

PROFESSIONAL EXPERIENCE AND REWARDS:

- September 2015-June 2016 Student Assistant at FMV Işık University, Faculty of Engineering.
- October 2018-June 2020 Research Project Assistant at FMV Işık University, Faculty of Engineering.
- December 2021-May 2024 Research Assistant at İstanbul Technical University, Faculty of Engineering.

PUBLICATIONS, PRESENTATIONS AND PATENTS ON THE THESIS:

- **Alan A. R.**, Bayındır, C., Ozaydin, F., Altintas, A. A. (2023). The Predictability of the 30 October 2020 İzmir-Samos Tsunami Hydrodynamics and Enhancement of Its Early Warning Time by LSTM Deep Learning Network, *Water,* 15(23), 4195.
- **Alan A. R.**, Bayındır, C. (2024). The Analytical Solutions of Long Waves Over Geometries with Linear and Nonlinear Variations in the Form of Power-Law Nonlinearities with Solid Vertical Wall, *Ocean Engineering,* 295, 117031.
- **Alan A. R.**, Bayındır, C. (2024). The Analytical Solutions of Long Waves Over Geometries with Linear and Nonlinear Variations in the Form of Power-Law Nonlinearities with Solid Inclined Wall, *Dynamics of Atmospheres and Oceans,* 106, 101458.

OTHER PUBLICATIONS, PRESENTATIONS AND PATENTS:

- **Alan A. R.** (2020). Impact Of Traffic Incident Duration And Road Characteristics On Traffic Flow Performance, *FMV Işık University,* M.Sc. Thesis.

- **Alan A. R.**, Bayındır C. (2021). Analysis Of Wave Runup, Overtopping And Overwash Parameters Via Compressive Sensing. *2nd International Conference on Applied Mathematics in Engineering (ICAME 2021)*, September 01-03, 2021 Balıkesir, Turkey.

- **Alan A. R.**, Bayındır C. (2021). Ocean Energy Conversion Analysis By Compressive Sensing. *2nd International Conference on Applied Mathematics in Engineering (ICAME 2021)*, September 01-03, 2021 Balıkesir, Turkey.

- Kesten A. S., **Alan A. R.** (2021). Modeling The Effects Of Traffic Incident Duration On Traffic Flow. *14th International Congress on Advances in Civil Engineering (ACE 2020-21)*, September 06-08, 2021 İstanbul, Turkey.

- **Alan A. R.**, Bayındır C. (2021). Predicting Ocean Energy Harvesting Dynamics Using LSTM Deep Learning Network. *The 34th Asian-Pasific Technical Exchange and Advisory Meeting on Marine Structures (TEAM 2020-21)*, December 06-08, 2021 İstanbul, Turkey.

- Bayındır, C., **Alan A. R.** (2022). Efficient Sensing Of Ground-borne Vibrations Induced By Pile Driving Using Compressive Sampling, *TWMS Journal of Applied and Engineering Mathematics,* 12(1), 24-33.